Polymorphic bio-filaments and their interaction with biological membranes

Julien Fierling

To cite this version:

Julien Fierling. Polymorphic bio-filaments and their interaction with biological membranes. Biophysics. Université de Strasbourg, 2016. English. NNT : 2016STRAE015 . tel-01469137

HAL Id: tel-01469137
https://theses.hal.science/tel-01469137

Submitted on 16 Feb 2017

UNIVERSITÉ DE STRASBOURG

ÉCOLE DOCTORALE DE PHYSIQUE ET CHIMIE-PHYSIQUE

Institut Charles Sadron

THÈSE présentée par :

Julien FIERLING

soutenue le : **09 septembre 2016**

pour obtenir le grade de : **Docteur de l'université de Strasbourg**

Discipline/ Spécialité : Physique

Polymorphic Bio-filaments and Their Interaction with Biological Membranes

THÈSE dirigée par :	
M. JOHNER Albert	Directeur de Recherches, Institut Charles Sadron, Strasbourg
RAPPORTEURS :	
M. MESSINA René	Professeur, Université de Lorraine
M. TURNER Matthew	Professeur, Université de Warwick
AUTRES MEMBRES DU JURY :	
M. KULIC Igor	Chargé de Recherches, Institut Charles Sadron, Strasbourg
M. SENS Pierre	Directeur de Recherches, Institut Curie, Paris
M. THALMANN Fabrice	Maître de Conférences, Université de Strasbourg

Résumé

Dans cette thèse, nous nous sommes consacrés à l'étude des bio-filaments polymorphes, et à leurs interactions avec des membranes biologiques. En particulier, nous avons développé, dans un premier temps, un modèle permettant de décrire des bio-filaments ne se comportant pas comme des filaments semi-flexibles. Dans un deuxième temps, nous avons étudié les interactions entre des filaments et des membranes tubulaires ou planes. Enfin, nous nous sommes intéressés à la façon de se mouvoir de la bactérie nommée Spiroplasma.

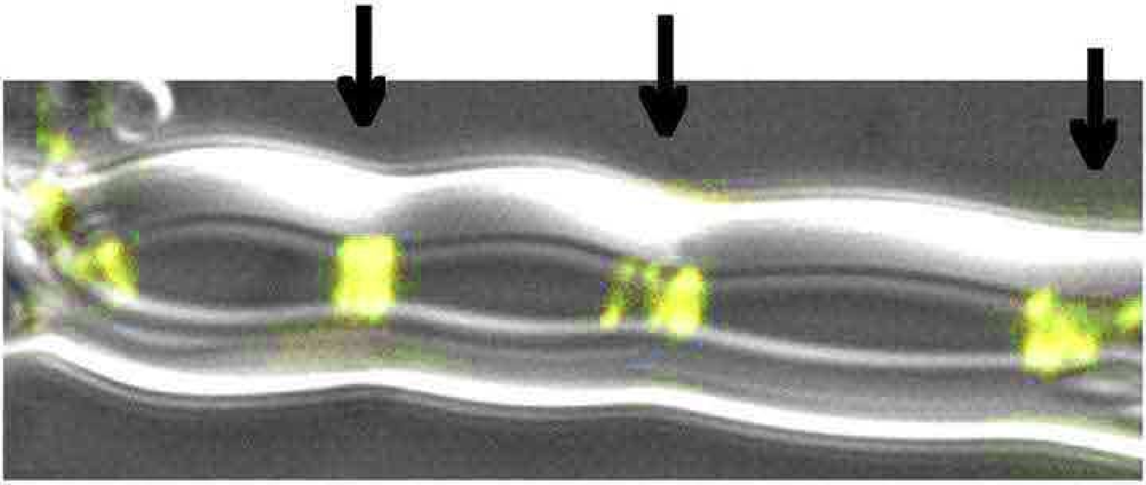

Figure 1: Un liposome comprenant trois anneaux circulaires de FtsZ représentés en jaune à l'aide d'une méthode de fluorescence. Les flèches indiquent ces anneaux [67].

Dans notre corps, mais également dans toutes les cellules, qu'elles soient eucaryotes ou prokaryotes, des protéines polymérisent formant des filaments. Ces filaments sont généralement décrits par des chaines semi-flexible (comme par exemple l'ADN), et ont pour énergie élastique (sans torsion) $E_{el} = \frac{B_f}{2} \int_0^L (\kappa - \kappa_0)^2 ds$, où B_f est le coefficient de rigidité du filament, κ la courbure à la position s le long de la courbe décrivant le filament, et κ_0

la courbure intrinsèque. Cependant, certains filaments importants au bon fonctionnement de la cellule, tels que l'actine, les microtubules, etc, ont des comportements différents. En effet, les protéines composant ces filaments peuvent changer de conformation sous l'action de réactions chimiques, de telle facon que les filaments eux-mêmes changent également de forme. Par exemple, la protéine FtsZ présente dans les bactéries est responsable de la division cellulaire après polymérisation en un filament circulaire (voir Fig. 1). Une réaction chimique entraîne un changement de conformation et une constriction de la bactérie. De même, la protéine de dynamine, qui forme une hélice autour de la membrane des cellules lors de l'endocytose (et qui peut être approximée par une série d'anneaux autour de la membrane) est également un filament dit *switchable*. De même que précédemment, une réation chimique permet un changement de conformation et une constriction de la membrane.

Dans le chapitre 2, nous avons étudié le comportement de ces filaments, dits *switchable*, que nous avons contraint à former une courbe fermée dans le plan. Dans un premier temps, nous avons étudié ce phénomène pour des filaments isolés, puis nous l'avons appliqué à un scénario possible de déformation de membranes tubulaires. Nous avons développé un modèle simple, pour lequel les consitutants de ces filaments (les protéines) ont une énergie différente de celle précédemment décrite. Notre modèle élastique non-linéaire en courbure permettant une ou plusieurs formes préférées. Pour ce faire, nous nous sommes arrêté à l'ordre 4 en courbure. De plus, nous n'avons pas considéré le cas où les filaments peuvent être intrinsèquement tordus. L'énergie par protéine est alors donnée par :

$$f(\kappa) = A\kappa - \frac{B}{2}\kappa^2 + \frac{C}{2}\kappa^4,$$

où A, $B > 0$ et $C > 0$ sont des constantes élastiques définies de telle manière qu'il existe au moins un état stable. Il est également à noter que le terme en κ représente une asymétrie dans le problème différenciant les deux faces des protéines (voir Fig. 2 (a)). Il est possible de créer un seul état stable si la constante A est suffisamment grande. Par la suite, nous avons forcé plusieurs de ces protéines à se lier et à former un cercle. Il est apparu que dans ce cas, grâce à la contrainte sur l'angle tangent à la courbe, les protéines n'ayant qu'un seul minimum d'énergie pris séparément en ont deux lorsqu'elles sont forcées à former un cercle (en intégrant sur toute la courbe, le terme en $A\kappa$

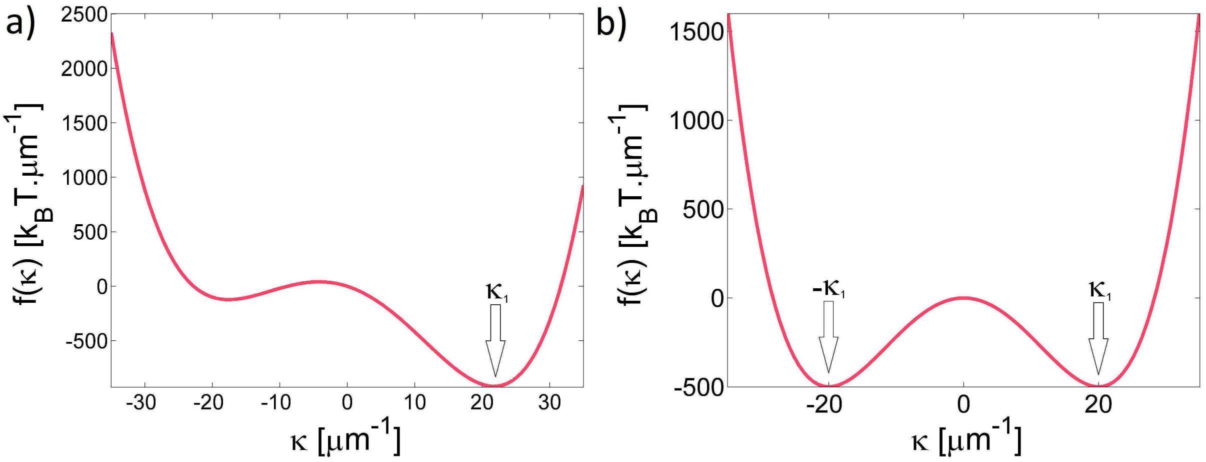

Figure 2: Energie des monomères en fonction de leur courbure κ. Pour a), les paramètres sont $A = -20 k_B T$, $B = 5 k_B T.\mu\mathrm{m}$ et $C = 1/160 k_B T.\mu\mathrm{m}^3$ et $\kappa_1 \approx 21.76 \mu\mathrm{m}^{-1}$. Pour b), les paramètres sont $A = 0 k_B T$, $B = 5 k_B T.\mu\mathrm{m}$ et $C = 1/160 k_B T.\mu\mathrm{m}^3$ et $\kappa_1 = 20 \mu\mathrm{m}^{-1}$. Pour un monomère de longueur $a = 10$ nm, la barrière d'énergie entre les deux minima est de $5 k_B T$.

donne une constante). Dans ces conditions, l'énergie de chaque protéine est donnée par une énergie effective symétrique par rapport à la courbure nulle. Les deux minima d'énergie sont donnés pour les valeurs suivantes de la courbure $\kappa = \pm\kappa_1 = \pm\sqrt{\frac{B}{2C}}$ (voir Fig. 2 (b)). Nous avons ensuite étudié les fluctuations élastiques de filaments composés de tels monomères et déterminé naïvement une longueur de persistance. Cette longueur est une longueur de persistence purement élastique, qui est différente de la longueur de persistence effective du filament. En effet, une seconde contribution est à prendre en compte, une contribution totalement entropique due au nombre d'états fondamentaux d'énergie qu'il est possible d'obtenir avec un tel système.

Puis, nous avons effectué une étude de la dégénérescence du nombre d'états fondamentaux pour un tel système. Il s'est avéré qu'à cause de la contrainte de fermeture, il était assez difficile de calculer l'entropie exacte du système, c'est pourquoi, dans un premier temps nous nous avons uniquement considéré un cas symétrique, le cas le plus simple étant pour nous lorsque l'on peut séparer la courbe en 4 parties identiques, et copier-coller la forme obtenue pour un quart de la courbe. L'entropie joue un rôle important dans ce système. En effet, due à l'entropie, l'énergie libre du système est différente de l'énergie élastique simple des monomères. Une étude de champs moyen a permis de déterminer que la courbure adoptée par les protéines n'est pas la courbure $\pm\kappa_1$, mais une courbure légèrement différente (pouvant être plus grande ou plus petite que la courbure $\pm\kappa_1$). Sans entropie, la dégénérescence de l'état fondamental n'apparaît que lorsque la courbure κ_1 est supérieure à celle d'un anneau non déformé, tandis que lorsque l'on tient compte de l'entropie, la transition de forme peut se réaliser même lorsque la valeur de la courbure κ_1 est inférieure à celle de l'anneau non déformé. Plus le nombre de monomères est grand, et plus le nombre d'états fondamentaux est élevé.

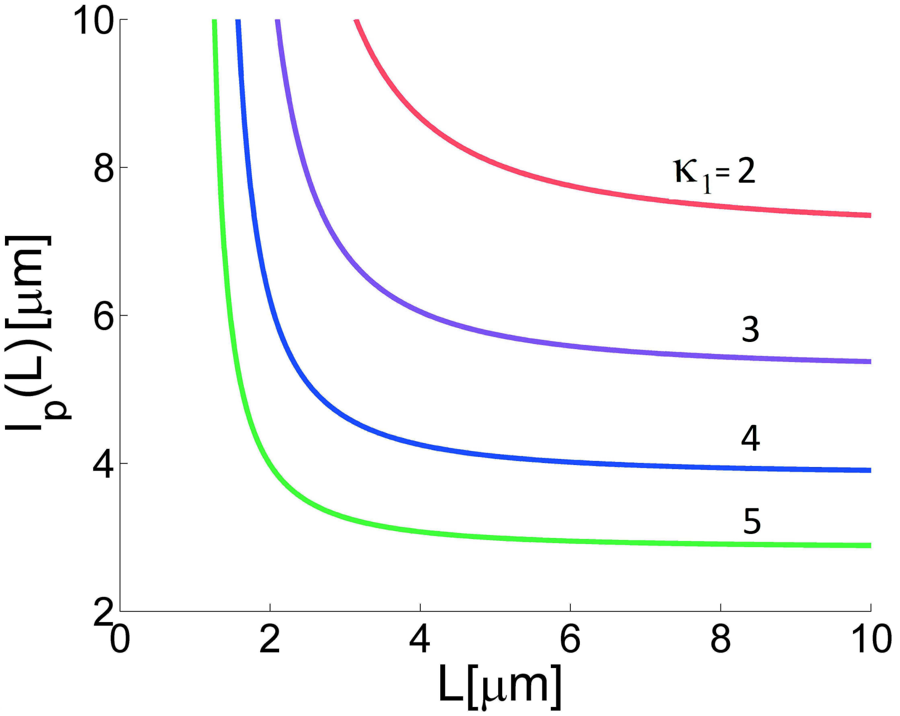

Figure 3: La longueur de persistance l_p d'un filament fermé dépend de sa longueur L. Les courbes représentent différentes valeurs de κ_1.

Par la suite, nous nous sommes placés dans un régime tel que les fluctuations élastiques peuvent être négligées, c'est à dire dans le cas de filaments rigides. Puis, nous avons développé un modèle "coarse-grained" de l'anneau, pour un nombre important de protéines composant l'anneau, ainsi qu'une courbure préférée κ_1 supérieure à la courbure nécessaire pour former un cercle parfait. Dans le cas de ce modèle, nous n'avons plus besoin d'utiliser la symétrie pour fermer la courbe. Le modèle "coarse-grained" s'applique à la courbure qui se comporte comme dans le cas d'une chaine semi-flexible classique. Nous avons donc décrit le filament comme une Worm-Like Chain avec une énergie effective donnée par cette théorie (énergie quadratique en courbure donnée dans le deuxième paragraphe). Il est important de noter que dans le cas étudié, comme les constituants de l'anneau adoptent une courbure $\kappa = \pm\kappa_1$, l'énergie du système est constante. Ce modèle est donc purement entropique. Pour forcer le filament à se fermer, il a été nécessaire d'effectuer une approximation sur les variations de l'angle tangent à la courbe. Le résultat de ces calculs, nous a permis d'obtenir la longueur de persistance totale du filament, dépendent de la longueur de persistance élastique et de celle entropique, déterminée par ce modèle "coarse-grained". Etonnamment, la longueur de persistance diminue lorsque l'on augmente la valeur de la courbure préférée des monomères, le filament devient plus mou (voir Fig. 3). Par ailleurs, à température nulle, pour une chaine semi-flexible classique, la longueur de persistance diverge. Dans notre modèle, elle reste finie à cause de la contribution entropique de cette dégénérescence.

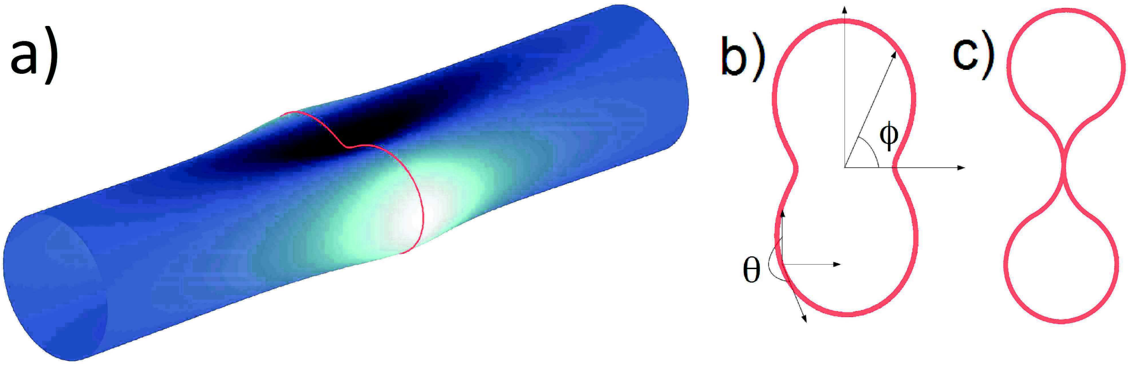

Figure 4: a) Un filament fermé sur une membrane fluide, b) peu déformé, c) critique pour $\kappa_1/\kappa_0 = 7/3$.

Finalement, nous avons étudié, pour illustrer le modèle, les effets de tels anneaux sur des membranes tubulaires. Nous avons remarqué qu'il est impossible de casser une membrane avec un tel anneau. Pour réussir à casser cette membrane, il faut introduire une nouvelle condition, il faut que les protéines soient couplés. Il est plus favorable énergétiquement pour les protéines d'être dans le même état que leur proche voisin. Il est donc défavorable de faire beaucoup de régions avec peu de protéines ayant la même courbure (aussi appelées domaines). Dans notre cas, les protéines auront soit une courbure positive κ_1 soit une courbure négative $-\kappa_1$. Il est

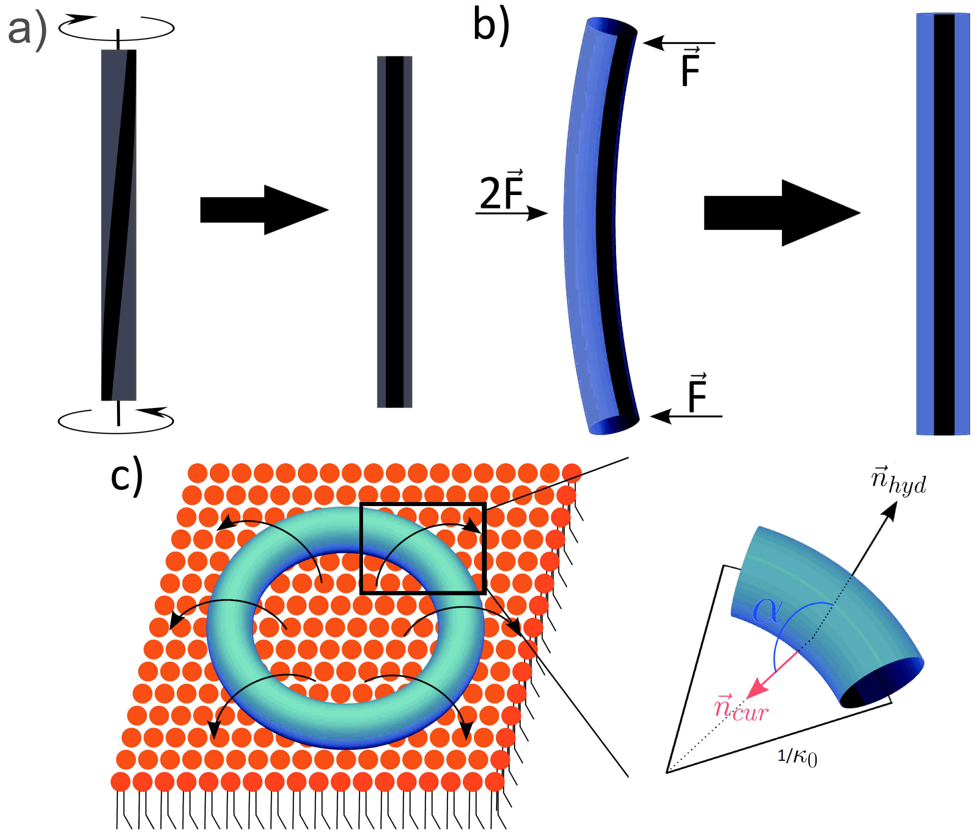

Figure 5: Représentation schématique d'un filament (a) droit et (b) courbé avec leur partie hydrophobe en noir, pre-contraint afin qu'ils adhèrent à des membranes planes. (c) Un filament circulaire, fermé appliquant des couples localement sur une membrane plane (*left*), formé par des monomères de courbure κ_0 avec leurs parties hydrophobes en noir (*right*).

plus favorable d'avoir deux régions de courbure positive et deux régions de courbure négative pour une forte coopérativité, permettant de casser des membranes (voir Fig. 4).

Dans le chapitre 3, nous avons étudié les déformations induites par des filaments sur des membranes planes ou tubulaires. Les filaments peuvent appliquer des forces mais également des couples. Au cours de ce projet, nous nous sommes particulièrement intéressés au cas moins traîté dans la littérature de filaments appliquant des couples voir Fig. 5). Cette étude a été faite pour des filaments rigides, dans le cadre des petites déformations. Afin de satisfaire cette dernière contrainte, le couple appliqué doit être faible et rester constant au cours de la déformation. Pour les membranes tubulaires, il est possible d'écrire le déplacement radial du tube comme : $u(\phi, z) = \sum_{n,m} C_{n,m} \exp\left(i(k_m z + n\phi)\right)$. Dans le cas d'une membrane plane, la même méthode a été utilisée. Finalement, il est possible d'écrire l'énergie de la membrane sous la forme :

$$E_{mem} = \sum_{n,m} M_{n,m} |C_{n,m}|^2,$$

où $M_{n,m}$ dépend des indices des modes de Fourier, et les $C_{n,m}$ sont les amplitudes des modes de Fourier.

Concernant les filaments que nous considérons donc comme rigides, nous nous sommes intéressés aux cas où ceux-ci appliquent des forces sur les membranes, ainsi qu'au cas où ils peuvent appliquer des couples. Afin d'intégrer les filaments dans nos calculs, nous avons décidé de ne pas considérer la structure interne des filaments, mais de les considérer comme des contraintes externes appliquées sur les membranes. Dans ce cas, la taille des filament n'est pas fixée, les filaments pouvant donc polymériser ou dépolymériser. Les résultats que nous allons donner par la suite seront pour le cas où les filaments ont été traité comme des systèmes de couples.

Dans un premier temps, nous avons traité le cas d'une seule protéine appliquant des couples sur des membranes planes et tubulaires (voir Fig. 6 (a)). Dans ce cas, une des différence apparaissant est une brisure de symétrie dans le cas de membranes tubulaires, tandis que pour des membranes planes, le système est anti-symétrique par rapport au moment appliqué. Ensuite, nous avons étudié les interactions médiées par la membrane entre deux protéines appliquant le même couple sur une membrane tubulaire. Il s'avère que le profil d'énergie est oscillatoire. En effet, dans un premier temps, pour de faibles distances entre les deux protéines, les deux protéines s'attirent, puis elles se repoussent, et ainsi de suite. Cependant, nous avons remarqué que les barrières d'énergie entre les différents minima (qui diminuent lorque l'on augmente la distance entre les deux protéines) sont très faibles comparées à l'énergie thermique, et sont donc quasi inéxistantes.

Ensuite, nous avons étudié les cas d'un filament fermé sur des membranes planes et tubulaires. Dans le cas d'un filament circulaire fermé sur une membrane plane, on remarque la formation d'une invagination. Concernant les membranes tubulaires, nous nous sommes intéressés aux plus petits modes n possibles, c'est-à-dire à une distribution de couples circulaire ($n = 0$, voir Fig. 6 (b), (d)) mais aussi ellipsoidale ($n = 2$). Pour un filament circulaire

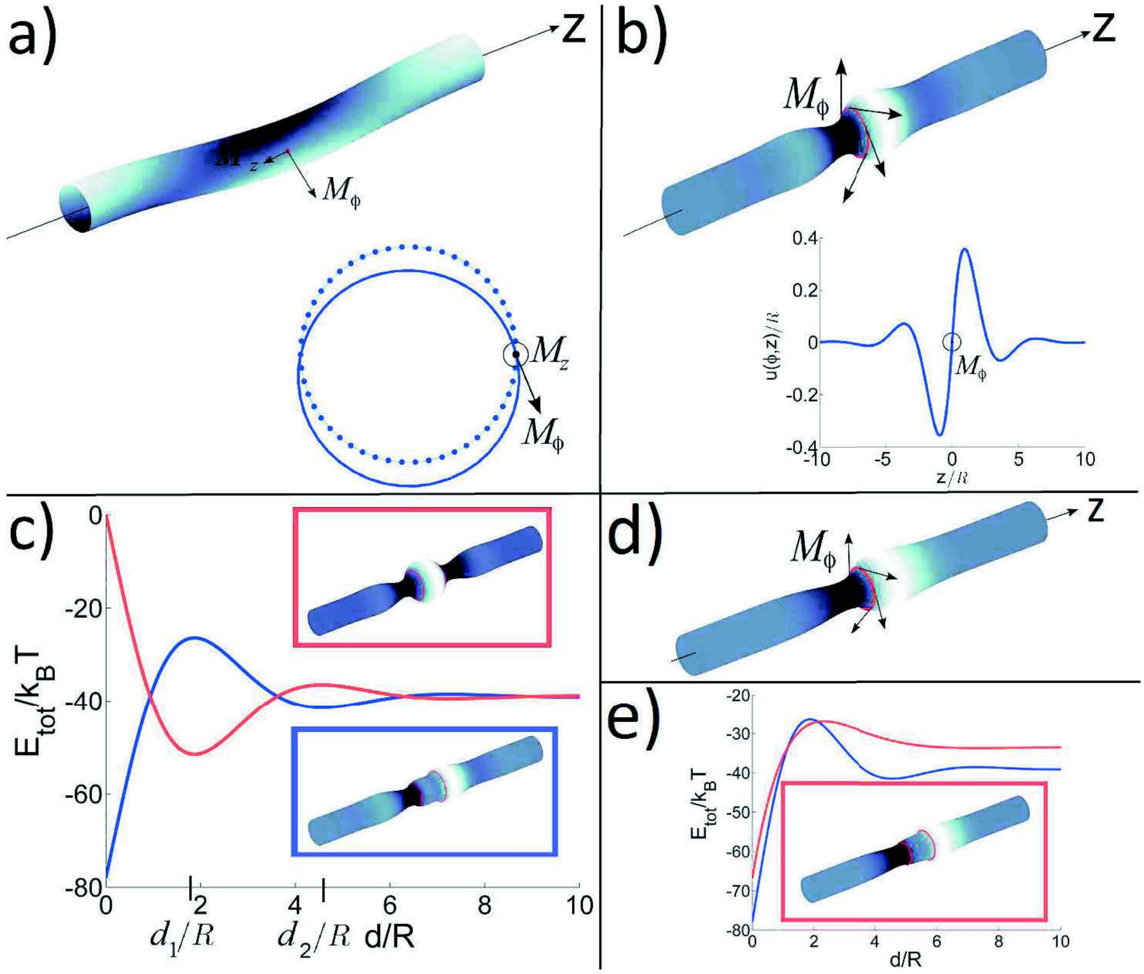

Figure 6: Déformations de membranes tubulaires induites par (a) un couple seul, et (b) un filament circulaire. (c) Energies totales et formes d'équilibre de deux distributions circulaires de couples. La courbe bleue dans le diagramme d'énergie correspond au cas où les deux couples sont identiques, tandis que la courbe rouge correspond au cas où les distributions de couples sont opposées. Il est important de remarquer que ces figures correspondent au cas où aucune force longitudinale n'est appliquée au tube ($\gamma = 0$). (d) Déformation d'une membrane tubulaire induites par un filament circulaire pour $\gamma = 2.2$. Dans ce régime, la tension de surface et la différence de pression entre l'interieur et l'exterieur de la membrane sont positves. (e) Energies totales de deux distributions circulaires de couples pour $\gamma = 0$ en bleu et $\gamma = 2.2$ en rouge. Dans l'encadré rouge, la forme d'équilibre du tube est représentée pour $\gamma = 2.2$.

($n = 0$), le profil du tube est oscillatoire amorti. Pour une distribution ellipsoidale ($n = 2$ uniquement), ce n'est pas le cas, et la membrane relaxe directement pour reprendre sa forme cylindrique. Par la suite, les interactions entre deux filaments fermés ont été étudiées, et comme pour deux protéines, un profil oscillatoire a été démontré. Cependant, contrairement au cas de deux protéines, il est possible de passer la barrière d'énergie pour aller dans le minimum principal (pour des membranes et filaments typiques, la barrière est d'environ $15k_BT$), mais il est impossible de sortir du minimum principal, la barrière étant trop grande ($\approx 50k_BT$) (voir Fig. 6 (c), (e)).

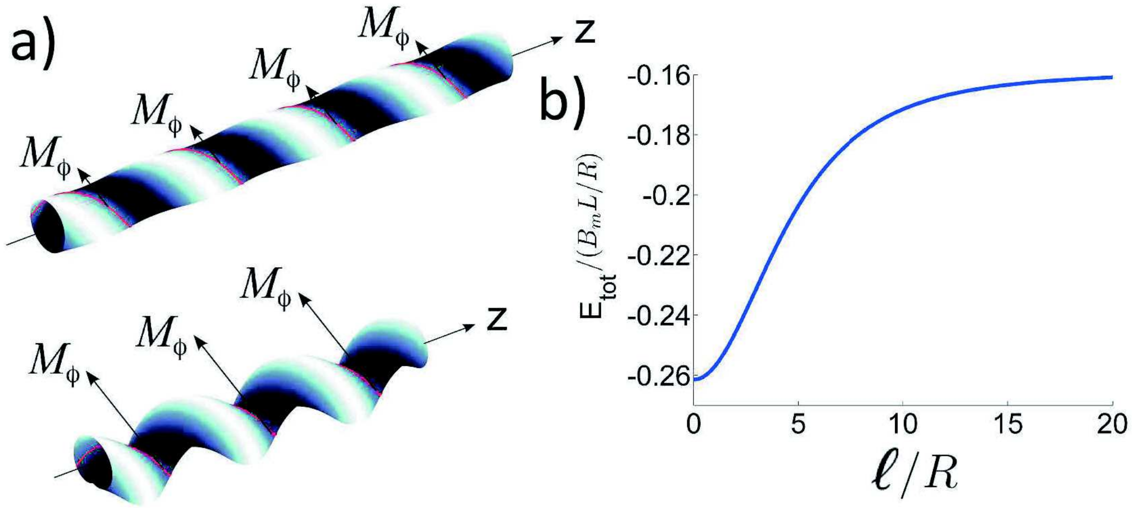

Figure 7: (a) Déformations d'une membrane tubulaire dûes à une distribution hélicoïdale de couples pour des valeurs faibles (*haut*) et élevées (*bas*) de M_ϕ. (b) Profil de l'énergie du système en fonction du pas ℓ de l'hélice.

Finalement, nous nous sommes intéressés à un filament hélicoidal sur une membrane tubulaire, toujours dans le régime linéaire (voir Fig. 7). Il est apparu que lorsque l'on augmente le couple, la membrane devient hélicoidale elle-même, et s'enroule dans l'espace, faisant diminuer sa longueur. Par ailleurs, plus le couple augmente, plus la déformation est grande, tel qu'au delà d'un certain moment, la membrane va commencer à s'auto-pénétrer et casser. Ce phénomène peut donc donner lieu à la fission de la membrane tubulaire. Il est à noter que pour des couples trop grands, nous sortons du régime linéaire. Enfin, nous avons étudié le profil de l'énergie par rapport au pas de l'hélice ℓ, et avons obtenu un seul minimum pour $\ell = 0$.

Enfin, dans le chapitre 4, nous avons commencé à traiter un problème en rapport avec une bactérie, connue sous le nom de spiroplasma, ayant une façon spéciale de se déplacer. En effet, cette bactérie possédant un cytoskelette (comme une grande partie des bactéries) est hélicoidale et se déplace en changeant d'hélicité (voir Fig. 8). Le changement d'hélicité d'une partie de la bactérie entraine a formation d'un "kink" entre les régions d'hélicités différentes. C'est en propageant ce "kink" le long de son corps

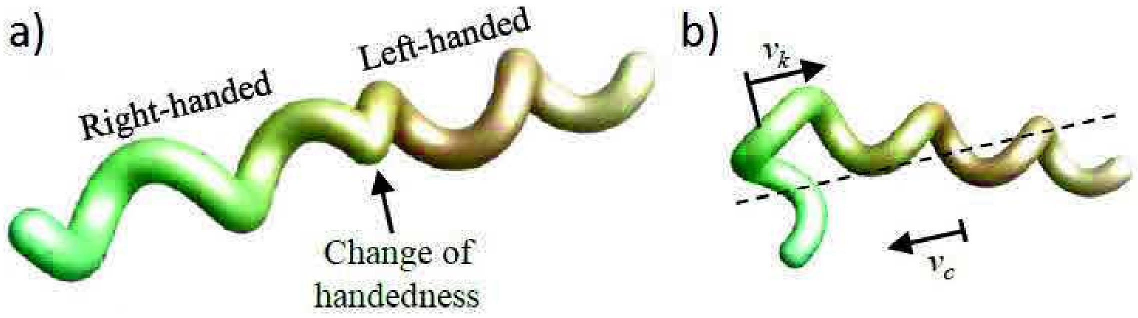

Figure 8: a) Schéma représentant le changement d'hélicité et b) la propagation du "kink" le long de la bactérie [140].

que la bactérie peut se déplacer dans le sens contraire du kink. A l'aide d'une théorie développée pour des surfaces pré-contraintes, nous avons étudié le changement de conformation du cytoskelette en fonction de cette pré-contrainte. Il est apparu que pour une pré-contrainte de la forme:

$$\epsilon = \epsilon_0 \left(\frac{y}{w}\right)^2 + C,$$

où w est la largeur du cytoskelette, C une constante et ϵ_0 l'amplitude de la déformation, une brisure de symmétrie est possible. Dans un second temps, nous souhaitons continuer ce projet afin de comprendre plus précisemment la propagation de ces "kinks", et donc la façon de se déplacer de la bactérie Spiroplasma.

Contents

Chapter 1

The biological cell

It is not the strongest of the species that survives, nor the most intelligent, but the one most responsive to change - Darwin (1809-1882)

Between 3.8 and 4 billions years ago, *abiogenesis*, the creation of life arising from non-living matter, is thought to have occurred on Earth. It is well accepted in the scientific world [1, 2] that life firstly belonged to the RNA world, and evolved to the DNA, RNA and protein world we live in. Few years later (between 3.5 and 3.8 billions years ago), the small living uni-cellular organisms, known as the *last universal ancestor* (LUA), evolved in first two, then three main families of living organisms. These families, the so-called *kingdoms of life* shown in Fig 1.1 (a) on the simplified *phylogenetic tree* are the *eubacteria*, the *archaea* and the *eukaryota* (Fig 1.1 (b)-(d)).

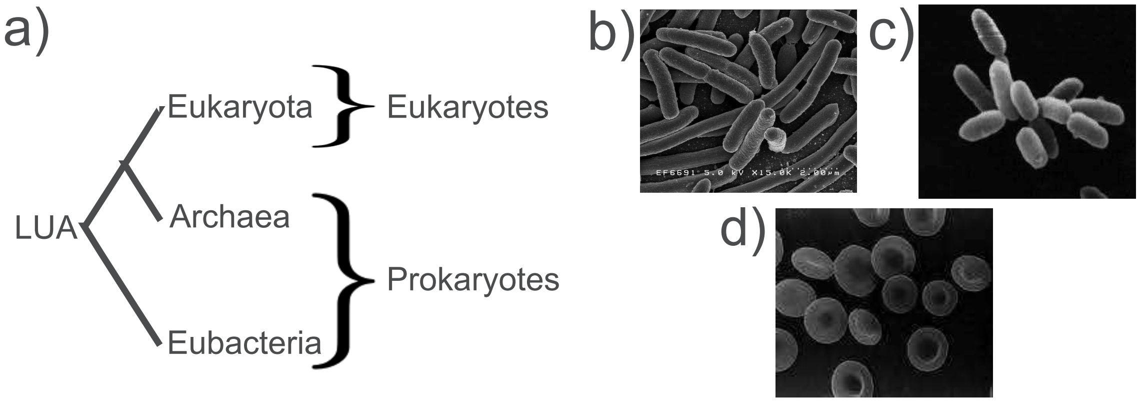

Figure 1.1: (a) Simplified representation of the phylogenetic tree, representing the three kingdoms of life. Examples of cells from these kingdoms : (b) eubacteria *Escherichia coli* cells [3] of length around 2-3 μm, (c) archaea *Halobacteria* [4] of length around 5 μm, and (d) eukaryota *red blood cells* [5] of about 6 μm in diameter.

Even if the archaea and the eubacteria differ, they are quite similar in shape and both are *prokaryotic cells*, whereas eukaryota are *eukaryotic cells*. The main difference between prokaryotic and eukaryotic cells lies in their internal structure. Prokaryotic cells lack internal well-defined structures: the nucleus and the organelles [6]. For instance, the

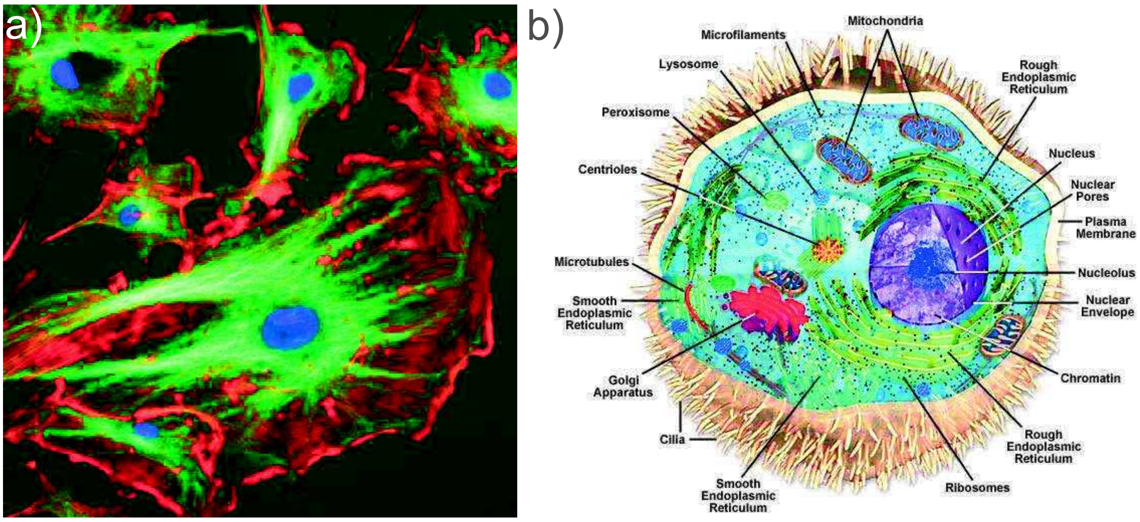

Figure 1.2: (a) Bovine pulmonary artery endothelial cells seen in fluorescence experiment. Nuclei, actin filaments and microtubules respectively appear in blue, red and green [7]. (b) Schematic representation of an animal cell [8].

mitochondria, where the energy needed by the cell is produced are organelles and are only present in eukaryotic cells (Fig. 1.2). The first living organism was unicellular, and through time and evolutionary processes, multicellular organisms emerged. On the one hand, the prokaryotes and some eukaryotes, such as yeast, are unicellular. On the other hand, all multicellular organisms, such as animals or plants are eukaryotes.

Cells are the functioning and structural unit of all living organisms. They possess at least a membrane protecting their internal constituents (such as proteins) and their genetic code (and the organelles for eukaryotic cells) from the external environment by controlling the exchanges between the inside and the outside of the cell. We will focus on the *biological membranes* in a first step. We will then give a brief overview on the internal ”inhabitants” of biological cells we are interested in, *i.e.*, bio-filaments.

1.1 Biological membranes

Biological membranes do not only delimit cells. In eukaryotic cells, two kinds of membranes are present: the cell membrane, and the organelles membranes. Interestingly, some organelles, such as the nucleus or the mitochondrion are double membrane-bound organelles [6]. Biological membranes are mainly composed of phospholipids [1], which are amphiphilic macromolecules (see Fig. 1.3 (a)). As the inside (cytosol [9]) and the outside (extracellular fluid) of the cell both are mainly made of water, lipids form a bilayer, where all the hydrophobic tails of the lipids are in the bilayer, avoiding contact with water molecules thanks to the hydrophilic heads protecting them (see Fig. 1.3 (b)).

Membranes alone do not entirely control the exchanges between the inner and outer

---

[1] The term phospholipid will be replaced simply by lipid in the following.

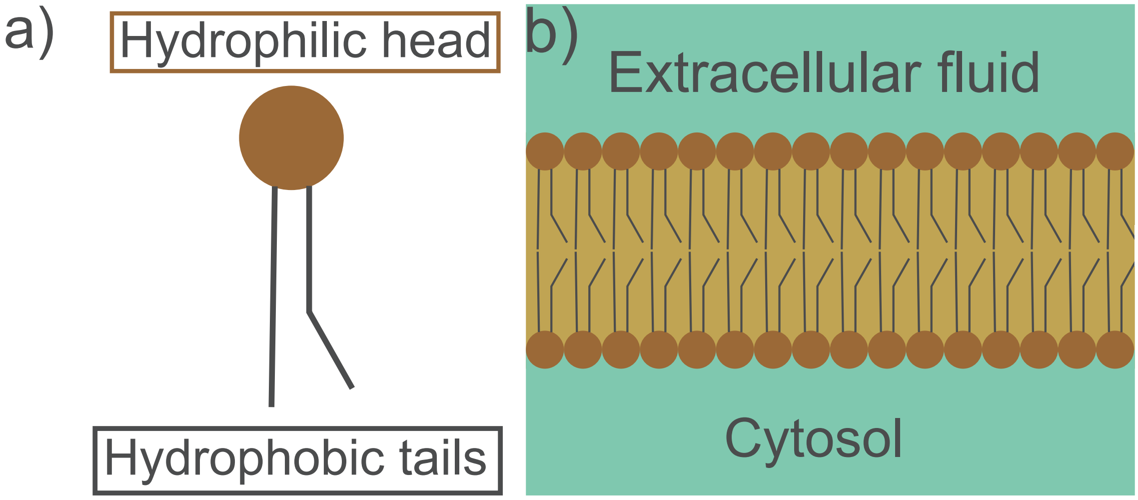

Figure 1.3: Simplified representation of (a) a single lipid and (b) a membrane bilayer.

parts of organelles or cells. Indeed, some macromolecules are involved in the functioning of the membrane. In particular, transport through membranes is of high importance and is governed by functional proteins [12]. For example, ion channels are involved in this mechanism by selecting ions penetrating the cell to regulate the electrostatic potential. Nonetheless, other larger molecules (such as proteins) are also needed in cells, and cannot go through membranes, but rather need to be ”swallowed” by them. This phenomenon is called endocytosis [13]. Cells do not only swallow but can also eject molecules from the inner part of the cell, this is called exocytosis [14].

Moreover, lipids can tune the properties of membranes. Cholesterol is one of them and plays a role in the fluidity of the membrane [10, 11]. Due to these intra-membranous macromolecules, but also to a wide diversity in the lipids composing membranes, the biological membranes present in all living cells are not as simple as shown in Fig. 1.3 (b).

1.1.1 Membranes as two-dimensional elastic sheets: Helfrich model

No theoretical model exists with the level of details just described, however, a simplified solvable and useful model to describe membranes has been developed by Canham and Helfrich [15, 16, 17]. In this model, the first assumption is to consider the membranes as thin sheets. Indeed, typical membranes found in Nature have a thickness of about 5 nm. For red blood cells (see Fig. 1.1 (d) and caption), the circumference of the membrane is about 20 μm. Comparing the in and out-of-plane sizes, one clearly sees that membranes can be seen as two-dimensional objects. In addition to this simplification, a coarse-grained approach is performed, such that the lipids are not considered themselves. The smallest size considered is larger than the lipids size. The composition of the bilayers can thus display several types of lipids. Nonetheless, the cholesterol and other intra-membranous proteins are not present in this description. Finally, under physiological conditions, bilayers are in the so-called fluid phase (see next subsection for more detailed discussion), and are elastic. Membranes are assumed to be bendable but not stretchable elastic sheets. Resulting membranes correspond to the one shown in Fig. 1.3 (b).

In the continuous limit, the energy associated with this simplified bilayer membrane, is then not purely geometric, as it is in general when we consider surfaces embedded in the three-dimensional world. Due to the elastic properties of the bilayer, a more general form of the energy is given by[18]:

$$E_{Hel} = \int \Big(2B_m \left(H - H_0\right)^2 + \bar{\kappa} K_G + \sigma\Big)\, dA, \tag{1.1}$$

where B_m and $\bar{\kappa}$ respectively are the bending and saddle-splay moduli and σ is the surface tension. H, H_0 and K_G respectively correspond to the mean, spontaneous and Gaussian curvatures. The mean and Gaussian curvatures are expressed in term of the principal curvatures κ_1 and κ_2 of the surface [2] such that $H = \dfrac{\kappa_1 + \kappa_2}{2}$ and $K_G = \kappa_1 \kappa_2$. The value of H_0 corresponds to the preferred curved state of the membrane. Finally, dA is the infinitesimal area element, and the integral is performed over the whole surface of the membrane. The first two terms of the energy correspond to its bending energy, and in particular the term depending on the Gaussian curvature can be rewritten such that it only depends on the topology of the surface. The Gauss-Bonnet theorem [19] permits the calculation of the integral for closed surfaces. It shows that the integral can be rewritten for a single closed surface as:

$$\int K_G dS = 4\pi(1 - g), \tag{1.2}$$

where g corresponds to the number of handles of the surface [3]. For instance, $g = 0$ for a sphere, and $g = 1$ for a torus. Note that this term does not change the energy if the topology of the system remains the same as it will be the case in the remainder of this manuscript. We will use the energy given by Eq. 1.1 in the following chapters (chapters 2 and 3) for different specific geometries.

1.1.2 Physical properties of membranes

Experimentally, properties of such membranes have been measured. One of the most interesting being the bending modulus also known as the bending stiffness. For this precise example, Small Angle X-Ray Scattering (SAXS) [20, 21, 22] and micropipette experiments [23, 24] are the most reliable techniques. For instance, in X-Ray scattering experiments, one illuminates the sample made of multilamellar phases, which corresponds to bilayers on top of each other separated by the distance $\bar{d}$ (see Fig. 1.4 (a) (right)). The main problem with this experiment is that there exist many regions of lamellar phases of different orientations, such that bilayers are not all parallel to each other (see Fig. 1.4 (a) (left)). The result obtained with such experiment should give Bragg peaks giving as a result the

---

[2] The principal curvatures correspond to the maximal and minimal values of the curvature normal to the surface. They measure the maximal and minimal bending of the surface at each point of the surface.

[3] For N closed surfaces, the integral is equal to $4\pi(N - N_h)$, where N_h is the total number of handles.

smectic periodicity $d = \bar{d} + \delta$ (where δ is the thickness of the bilayer) thanks to Bragg's law :

$$n\lambda = 2d\sin(2\theta), \tag{1.3}$$

where n is the order of reflection that takes an integer value, λ is the X-Ray wavelength (between 1 and 100 nm) and θ is the scattered angle (see Fig. 1.4 (b)). However, as the experiments are done at finite temperature, membranes fluctuate. Such fluctuations widen the Bragg peaks, which are linked to the bending modulus, and make them asymmetric (see Appendix A.1). The SAXS experiment can be coupled to other measurements such as Nuclear Magnetic Resonance (NMR) analysis [29] or Surface Force Apparatus SFA measurements [30], for higher precision. In particular, the compressibility modulus can be determined thanks to SFA, such that the bending modulus can be deduced from Eq. A.15 given in appendix A.1:

$$B_m = \frac{9\pi^2}{64}\frac{B(k_BT)^2}{d^4}, \tag{1.4}$$

where B is the compressibility modulus.

In the case of a micropipette experiment (see Fig. 1.4 (c)), the pressure inside the micropipette P_p is tunable, allowing the creation of a difference of pressure with the medium $\Delta P = P_{out} - P_p$. The aim of the experiment is to attract and suck up a vesicle present in the medium in the micropipette. This is only possible for $\Delta P > 0$. It is important to note that for too small ΔP (of the order of 1 Pa = 10^{-2} pN.μm^{-2}), fluctuations of the membrane forming the vesicle are large, and the shape of the quasi-vesicle outside the micropipette is not circular. Increasing ΔP to a value of the order of 10 Pa, the membrane of the vesicle still fluctuates but is assumed to be circular. Knowing all these parameters but also the sucked length L, and the surface tension of the vesicle thanks to Laplace law [4] giving

$$\sigma = \frac{R_p\Delta P}{2\left(1 - \dfrac{R_p}{R_v}\right)} \tag{1.5}$$

allows to determine the bending modulus of the studied vesicle (see Appendix A.2). Typically, the bending modulus of bilayer membranes is of the order of $10 - 30$ k_BT under physiological conditions, where k_B is Boltzmann's constant and T is the temperature. Also note that one can attach a magnetic bead to the vesicle, trap it thanks to magnetic tweezers [26] and move it away from the vesicle, thus applying a longitudinal force and creating a tubular membrane [27, 28].

Numerically, coarse-grained experiments have been performed, where the lipids are described by few beads. A single bead describing a lipid would not give precise results, not allowing for instance to consider the possible polarity of the lipids. For example, the

---

[4] Note that a generalized Laplace law is necessary for radii smaller than 10 nm for typical membranes [25].

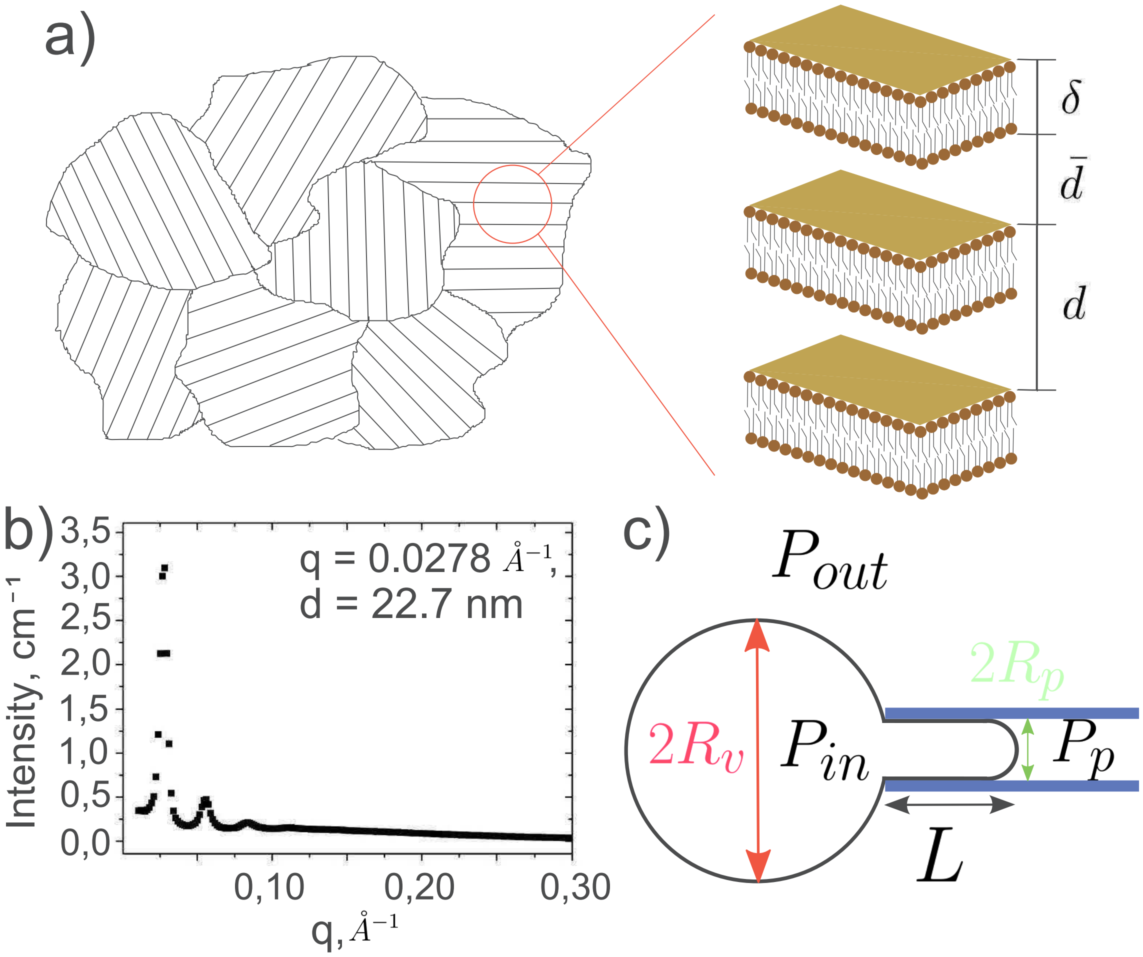

Figure 1.4: Schematic representations of X-Ray (panels (a) and (b)) and micropipette (panel (c)) experiments. (a) Typical X-Ray sample, showing multi-domains lamellar phases (left) and a zoomed view of a lamellar phase (right). (b) Example of plot of intensity scattered by the lamellar phases sample as a function of the wavevector q. Three Bragg peaks are visible, allowing to infer the periodicity of the sample: $d = 22,7 \pm 0,4$ nm [29].

Martini force field has been developed for molecular dynamic simulations of lipids [31]. Numerical simulations also have been performed to determine phase stability of ternary mixtures. Assuming that the competition between the liquid and gel order of the lipids is the main driving force behind lipid segregation, they calculated a free energy of mixing. The simulations enabled a fast determination of the phase diagram [32]. Full atomistic simulations also have been performed, but mostly to study membrane-proteins interactions [33]. Simulations could also give insight on the collective properties of the bilayers. However, the number of particles needed to highlight such properties is so high that calculations need too much time and memory.

The properties of the simplified bilayer membranes we consider have microscopic origins. For instance, in a fluid, lipids are large molecules, and thus can freely move (if not linked to anything) due to collisions with smaller particles of the fluid in their vicinity.

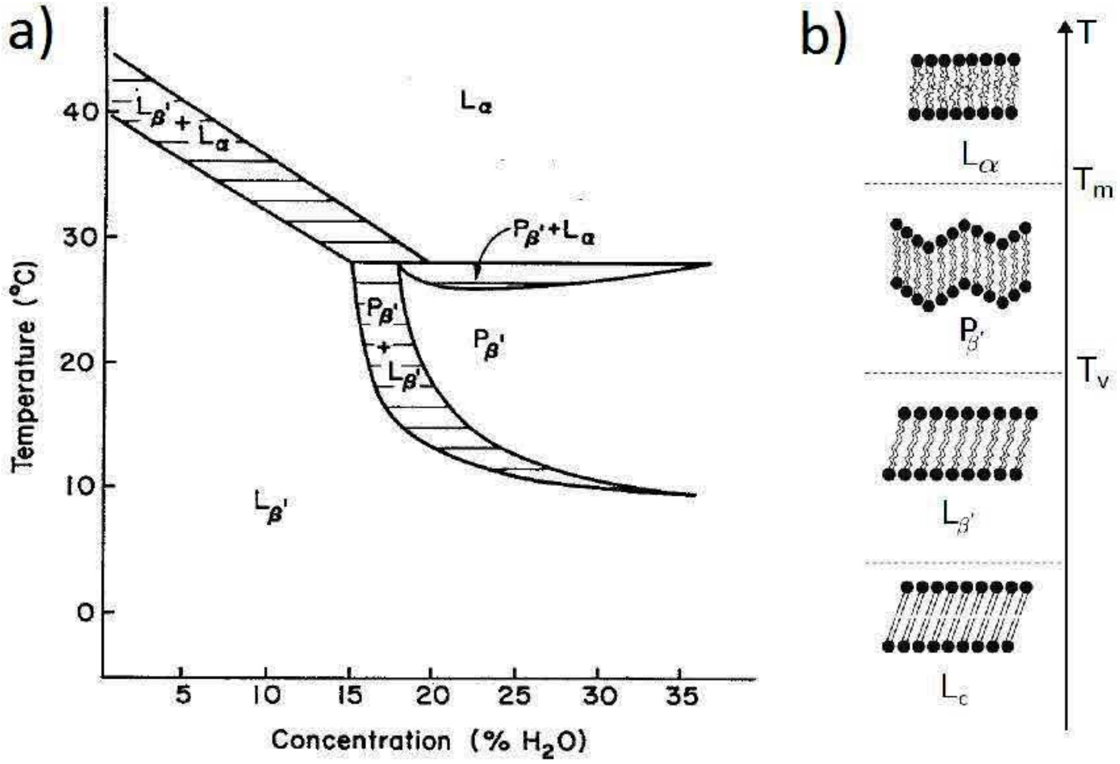

Figure 1.5: (a) Experimental phase diagram for DMPC (a sort of two-tailed lipid) plotted as a function of temperature and hydration[34]. (b) Schematic representation of the different phases, where L_c, $L_{\beta'}$, $P_{\beta'}$ and L_α respectively are the crystalline, gel, ripple and fluid phases. T_v corresponds to the gel-ripple transition temperature, while T_m is the fluid transition temperature [44].

The motions of the lipids depend on external parameters. In particular, temperature plays an important role on their mobility. Moreover, for lipids in water, the water fraction (also known as hydration) also modifies the properties of bilayers for fixed temperature as shown on the phase diagram on Fig. 1.5 (a). Another interesting behaviour is linked to the relative values of the elastic constants B_m and $\bar{\kappa}$ defining the membranes. This second diagram will represent not a real phase diagram, but more a shape diagram.

Let us firstly focus on the water concentration-temperature phase diagram shown on Fig. 1.5 (a). It presents three of the four phases encountered for different temperatures and water concentrations. The fourth phase, which is known as the crystalline phase L_c does not appear on this diagram as it only exists at low temperature. In this phase, the lipids arrange in a well defined structure and have a mobility assumed to be null [5]. Heating the system increases the thermal fluctuations which affect the lipids. This additional thermal energy allows the lipids to diffuse faster. The structure is still well defined, but the lateral organization of the lipids is lost. In this state, the so-called gel phase $L_{\beta'}$, the diffusion coefficient is small, but non zero ($D < 10^{-2}\mu\text{m}^2.s^{-1}$) [35, 36]. Depending on water concentration, the lipids might behave slightly differently in the so-called *ripple* phase $P_{\beta'}$. In

---

[5] This is the analogue to the solid state in hard matter.

particular, the lipids do not form a quasi-flat membrane but display a corrugated state [37, 38]. The period of oscillations depends on the lipids, but are in a range of 100 to 300 $\mathring{A}$. Finally, at high temperature, the bilayer membranes are in the fluid phase L_α. In fluid membranes, the diffusion coefficient increases drastically to reach a value of the order $1 - 10\mu\text{m}^2.s^{-1}$ [39, 40]. Note that this diffusion coefficient, as the one given for the gel phase, is only valid for diffusions along a monolayer. Moreover, the bilayer is softer in this state, and fluctuates more in the out-of-plane direction.

Interestingly, transition temperatures mainly depend on the nature of the tails. In particular, for short lipid chains, the transition temperatures are lower than for long lipid chains. Similarly, the more unsaturated lipids are, the faster they change state. Furthermore, long-chained lipids do not display ripple phase [38].
At room temperature, membranes are in their fluid state, but what is their topology ?

Let us consider only the elastic energy of an intrinsically flat membrane ($H_0 = 0$), and study its stability. For a flat membrane, as the mean and Gaussian curvatures are zero, the elastic energy also is $E_{el} = 0$. Consider now the case of the same membrane, but closed. Its elastic energy then reads:

$$E_{el} = \int 2B_m H^2 dA + 4\pi\bar{\kappa}(1-g). \tag{1.6}$$

The bending modulus B_m being always positive, let us investigate the stable shapes of membranes due to the effect of the saddle-splay modulus $\bar{\kappa}$. On the first hand, for $\bar{\kappa} < 0$, the second term of the elastic energy (Eq. 1.6) is minimum for $g = 0$, meaning that the membrane does not present handles. Two possible phases without handles correspond to the flat membrane, and the spherical membrane, *i.e.*, the vesicle. Note that the area is the smallest possible one in these two particular cases, meaning that the energy term corresponding to the surface tension also is minimal. The question now is to find out whether a vesicle is more stable than a flat membrane. For a vesicle, both radii of curvature correspond to its radius R. The first term in the elastic energy (Eq. 1.6) thus gives

$$\int 2B_m H^2 dA = 8\pi B_m. \tag{1.7}$$

The vesicular state is favorable when its elastic energy is negative, whereas the flat state is favorable when $E_{el} > 0$ in Eq. 1.6. This implies that the membrane is in its spherical state for $\bar{\kappa} < -2B_m$, and in the flat state for $-2B_m < \bar{\kappa} < 0$. On the other hand, for $\bar{\kappa} > 0$, the second term of the elastic energy (Eq. 1.6) is minimal for g going to infinity, which would mean for an infinite number of handles. This is however not the case. Indeed, the energy proportional to the mean curvature can be minimised for $H = 0$, *i.e.*, for $\kappa_1 = -\kappa_2$. However, the surface tension term in the free energy is not minimised for $g \to \infty$. A competition between these two terms gives the final number of handles. This is the so-called cubic phase.

In the previous analysis of the shape diagram, we only considered one membrane, but this result holds in general for N membranes. It is also important to note that this study is done at a temperature of 0 K. At finite temperature, membranes fluctuate and the cubic

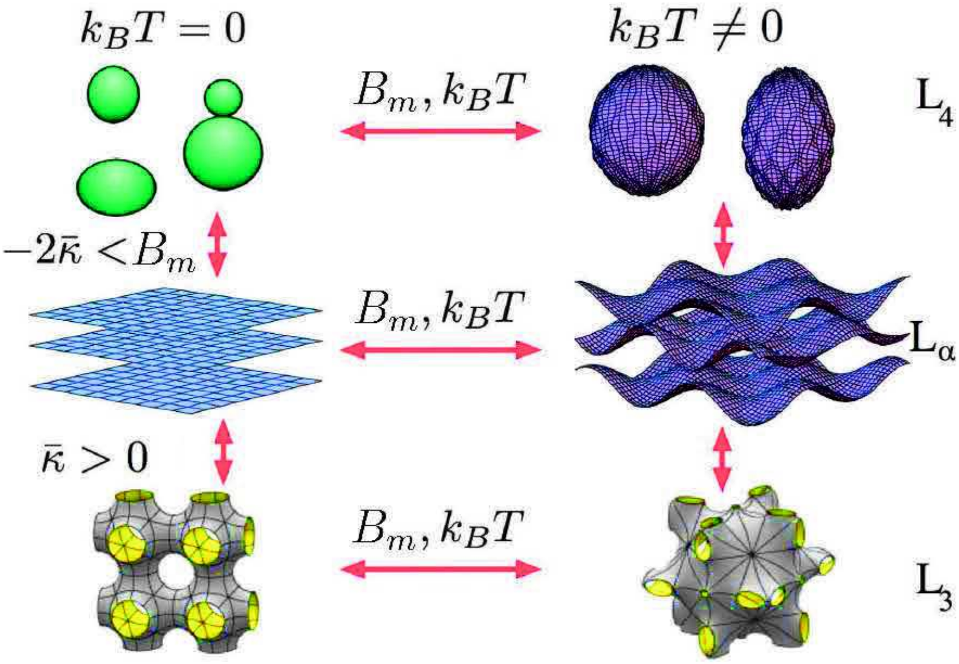

Figure 1.6: Schematic representation of the stability of a lamellar phase at 0 K (left), and at temperature T (right). L_4, L_α and L_3 respectively correspond to the vesicular, lamellar and sponge phases [41].

phase is called the sponge phase (see Fig. 1.6).

These phase and shape diagrams exist because, depending on the external temperature, lipids can diffuse along the membrane. Nonetheless, this is not the only motion lipids can display. We present these motions from the most to the less frequent (see Fig. 1.7)

- The tails of the lipids can move very rapidly, with a change of conformation approximately every 10^{-12} s.
- Lipids can freely turn round in a characteristic time of approximatively 10^{-9} s.
- Lipids can leave the layer plane from a distance of the order of the Angström. This is the so-called protrusion which happens also in a characteristic time of the order of 10^{-9} s [42].
- As already mentioned, lipids diffuse along the membrane, with the diffusion coefficient depending on the phase. For the crystalline phase, it is assumed to be null, whereas for the gel phase, it is smaller than 10^{-2} μm^2.s^{-1}. Under physiological conditions, *i.e.*, in the fluid phase, it is of the order of 1 to 10 μm^2.s^{-1}. For instance, for a red blood cell of diameter equal to 6 μm, a lipid can turn around the cell in 6 to 20 s.
- Finally, lipids can switch from one layer to the other one of the bilayer. This is the so-called flip-flop. This is the less energetically favorable movement of the lipids, such that its characteristic time is close to the hour [43]. There is a difference of 15 orders of magnitudes between the most and the less frequent movements of lipids.

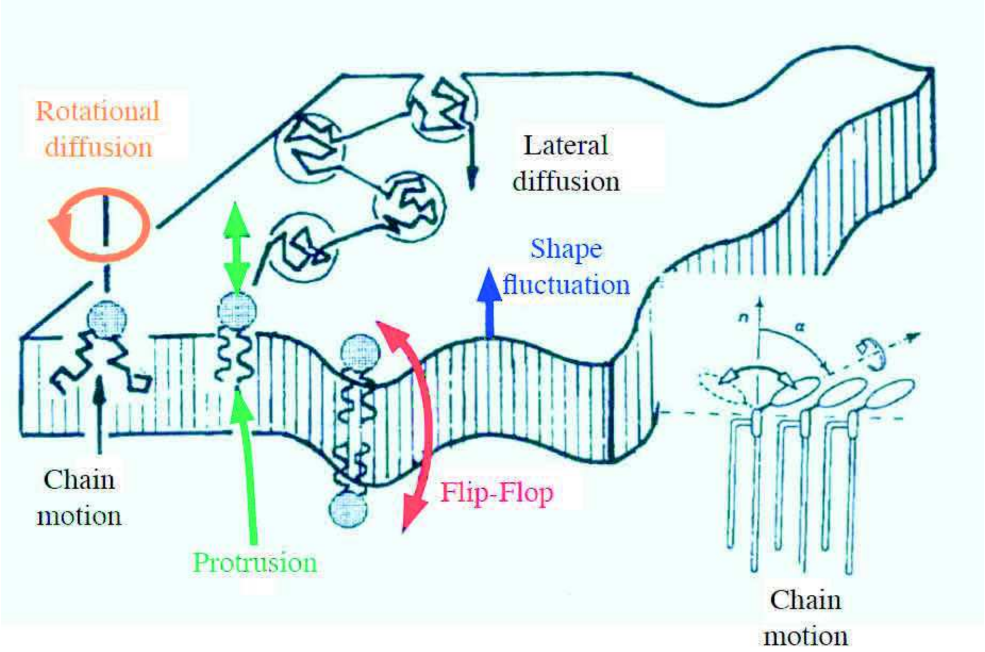

Figure 1.7: Schematic representation of a bilayer membrane and various lipids motions [44].

The lipids motions lead to collective motions, and changes in the properties of membranes. In particular, lateral diffusion of lipids are particularly linked to the phase of the membrane. For instance, in the fluid state, lipids diffuse rapidly, such that the membrane does not sustain shear in the plane. In other words, no torque can be applied to fluid membranes in the out-of-plane direction.

1.2 Bio-filaments

For now, we discussed bilayer membranes utility in the functioning of cells, *i.e.*, mainly protection of the inside of the cell and cell transport. We also examined the physical properties of simplified membrane bilayers. In particular, their elastic properties are of high importance to understand the shape of cells. Nonetheless, membranes themselves under physiological conditions would not exist. Indeed, it is known that membranes tear for surface tensions of the order of 10^{-3} N.m^{-1} [45]. Under physiological conditions, the osmotic pressure is of the order of 10^5 Pa [46]. Using a simple Laplace law for a spherical membrane of radius $r \approx 2\mu$m, one finds a surface tension of the order of 10^{-1}, which is larger than the surface tension of rupture. This means that inside cells, one finds other constituents, which help membranes maintaining their stability [47]. These are the so-called *proteins*.

For instance, as already mentioned, some are devoted to maintain the shape of the cell (spectrin for red blood cells for example). Other proteins are involved in cell transport, cell division... Proteins might also assemble (polymerise) to form long chains of proteins. Furthermore, one finds another type of macromolecules in cells, the so-called nucleic acids. These macromolecules, which are also of high importance for life (see below), are made

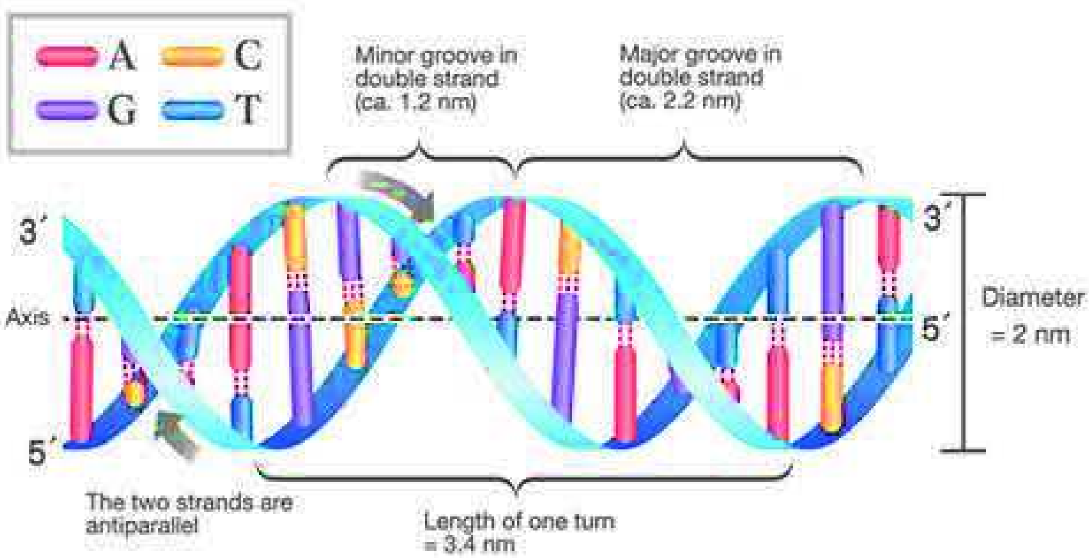

Figure 1.8: Schematic representation of a double-stranded DNA [50].

of nucleotides. These long chains can be termed as bio-polymers or bio-filaments. Both assembly (polymerisation) and disassembly (depolymerisation) occur as needed by cells. In the following overview, we will first discuss various examples of bio-filaments. In a second step, we will discuss one of the theoretical model used to describe bio-polymers, and its limits.

1.2.1 Examples of bio-filaments

The most prominent bio-filament is *DNA* [48], which contains the genetic information of the living organism. It is localized in the nucleus of eukaryotes and directly in the cytosol (the liquid inside cells) in prokaryotes. Interestingly, DNA is one of the two bio-filaments that are composed of nucleotides. The second one is *RNA* [49] which main role is to synthesize proteins. The chemical structures of these two macromolecules are similar. Indeed, DNA is made of four types of nucleotides: guanine (G), cytosine (C), adenine (A), and thymine (T), whereas for RNA, Uracil (U) replaces thymine. Moreover, they both are double-stranded helices, where the two strands are anti-parallel, as shown in Fig. 1.8.

Amino acids polymerization leads to proteins. Proteins assembly forms long filaments, which are useful for the life of the cell. The list of filaments is long, with the foremost being actin [51, 52, 53, 54], microtubules [55, 56, 57, 58], intermediate filaments [59, 60, 61], dynamin [62, 63, 64, 65] in eukaryotic cells, and FtsZ [66, 67, 68, 69, 70] and MreB [71, 72, 73] in prokaryotic cells. In Table 1.1, we present the main roles of these bio-filaments.

In particular, two of these filaments motivated our work. The first one, dynamin is a member of the GTPase family[6], which participates to membrane fission [65]. In mammal cells, it has three forms. Dynamin1 is only present in neurons and is involved in the

---

[6] In cells, the energy can be provided by two nucleotides: Adenosine triphosphate (ATP) or Guanosine triphosphate (GTP). Dynamin uses the energy released by GTP, when transformed into GDP to perform work.

Name	Actin	Microtubule	Intermediate filament
Main roles	Cell migration Cell division Muscle contraction	Cell division Intra-cellular transport Cell shape	Cell solidity Cell shape
Name	MreB	FtsZ	Dynamin
Main roles	Rod-like cell shape	Cell division	Endocytosis

Table 1.1: Presentation of some bio-filaments and their main roles in the life of the cell.

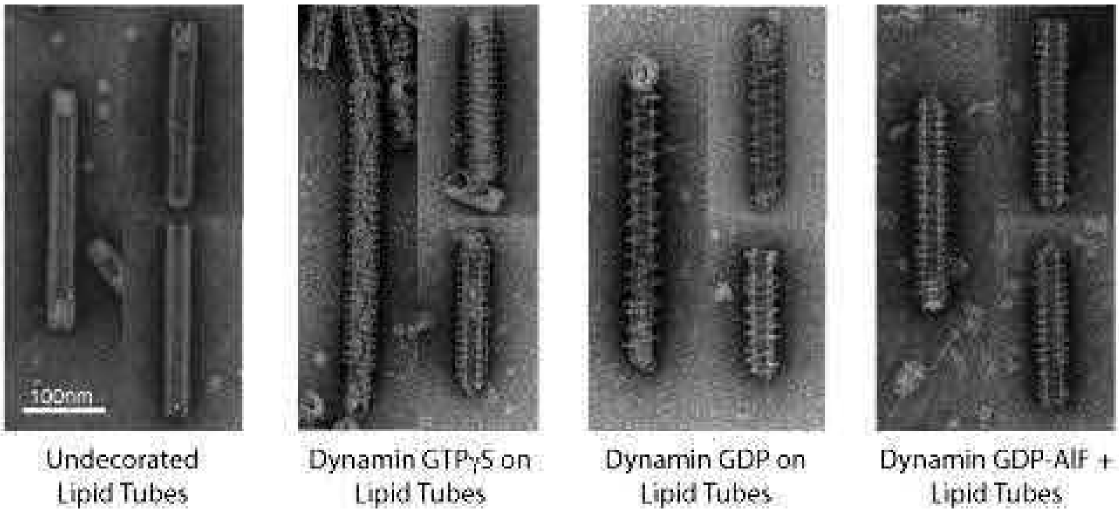

Undecorated Lipid Tubes

Dynamin GTPγS on Lipid Tubes

Dynamin GDP on Lipid Tubes

Dynamin GDP-AlF + Lipid Tubes

Figure 1.9: Dynamin coiling around lipid nanorods in presence of different nucleotides seen under negative stain electron microscopy [78].

formation of synaptic vesicles [74]. Dynamin2 is responsible for clathrin-mediated endocytosis, in all types of cells [75]. Finally, Dynamin3 is the least characterised of these three isoforms of dynamin, and is thought to have a presynaptic function, similar to Dynamin1 [76]. Dynamin proteins[7] polymerise to form helically-shaped bio-filaments around tubular membranes. *In vivo* and *in vitro*, when the function of dynamin has been blocked, *i.e.*, without GTP, the filaments were found to be identical. When wrapped around tubular membranes of diameter of about 20 nm, dynamin helices were found to display external diameters of approximatively 50 nm, and few tens of nanometers long [77]. It is thus assumed that dynamin proteins have a size of approximatively 15 nm.

Nonetheless, the pitch of the dynamin filaments differ. Indeed, *in vitro*, the pitch was found to lie between 10 and 13 nm [79, 80], whereas *in vivo*, it is close to 20 nm [81]. This difference comes from the association of dynamin with BAR proteins, which are not present *in vitro*. When wrapping around tubular membranes, the dynamin filament is a right-handed helix with ≈ 14.3 proteins per helical turn. In presence of GTP, dynamin and GTP first bind, then dynamin hydrolyses the GTP. This process releases some energy that can be utilised by dynamin to change its shape. The use of this energy to change

---

[7] In principle, we should term the subunit of the dynamin filament as a dimer. Indeed, the dynamin monomer is an almost straight protein, and the subunit, which looks like an ”X” is made of two of these monomers. In the text, when mentioning ”dynamin protein”, we consider in reality the ”X” dimer.

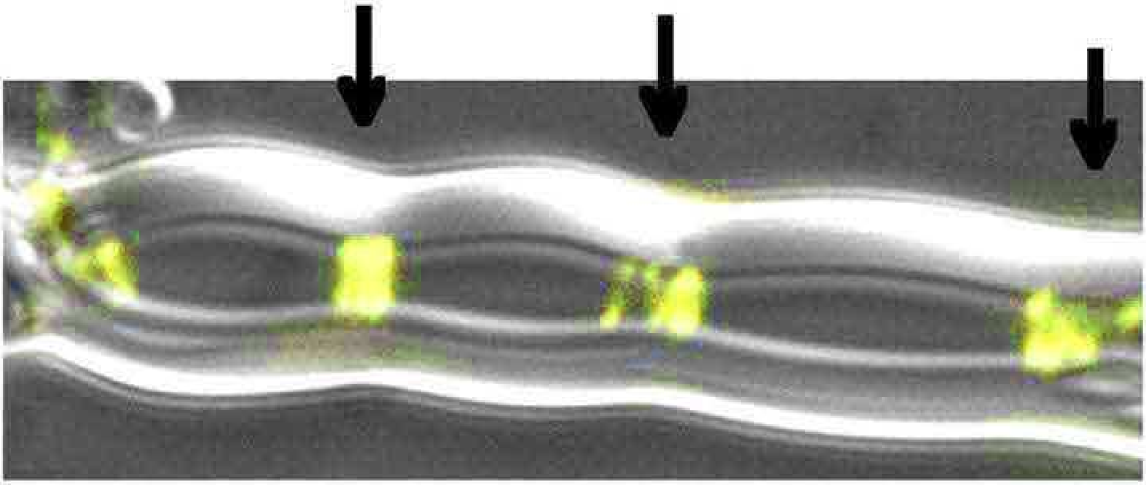

Figure 1.10: A liposome with three bright Z rings, each centered on a constriction. The fluorescent FtsZ is shown in yellow, superimposed on the differential interference contrast image of liposome. Arrows indicate Z rings [67].

conformation has been studied in particular by Stowell *et al* [78] on tubular nanorods (see Fig. 1.9) and Sweitzer and Hinshaw [82].

The main difference between these two papers lies in the effect of the GTP hydrolysis on the shape of the whole system. In the first case, the pitch of the helix increases upon hydrolysis, whereas in the second paper, the pitch reduces. This difference comes from the tube, which in the case of Stowell *et al* is stiff (the tube is rod-like), whereas in Schweitzer and Hinshaw, dynamin wraps around a tubular membrane. A theoretical model developed by Lenz *et al*, which assumes that the dynamin filament constricts the tube, confirms the effect of the stiffness of the tube on the pitch of the helically-shaped dynamin filament [63]. According to Sweitzer and Hinshaw, the outer radius of the dynamin helix decreases from 25 to 20 nm, while the pitch decreases from 13 to 9 nm. Assuming that the height of the dynamin proteins remain the same upon constriction, one sees that the radius of the tubular membrane decreases from 10 to 5 nm. The constriction itself is thus not sufficient for membrane fission. Indeed, membranes are assumed to fission during the so-called hemi-fission phenomenon, where two opposite sides of the membrane inter-penetrate. This happens for radius smaller than the lipid bilayer which is of the order of 5 nm. As constriction is not sufficient for membrane fission, there is another phenomenon which breaks the tube. At the neck of the tubular membrane, at the border between where dynamin constricts, and where there is no dynamin, there is a change of curvature of the tube. In this particular region, the surface tension is the highest. For high enough surface tension, the tubular membrane might fission.

The second one, FtsZ [66, 67, 68, 69, 70], is a protein also member of the GTPase family. It is found in bacteria where it plays a crucial role in cell division. It is a tubulin homologue which has the same function as the actin protein found in eukaryotic cells. *In vitro*, FtsZ proteins assemble into one-stranded proto-filaments made in average of 30

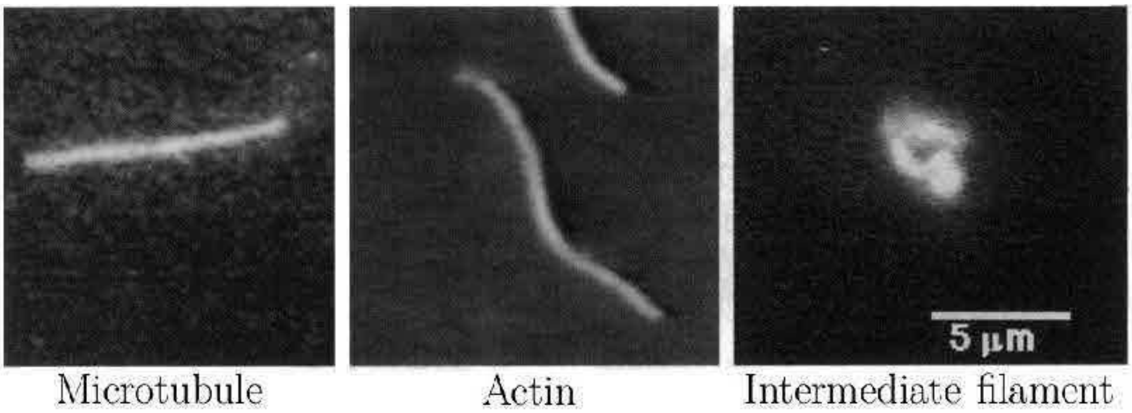

Figure 1.11: Fluorescence images of three bio-filaments discussed in Table 1.1. (a) Microtubule, (b) Actin and (c) Intermediate filament [87].

subunits for a length of 125 nm [83]. *In vivo*, these proto-filaments assemble into long filamentous structures attached to the inner bacterial membrane. They do not directly bind to the membrane but bind to FtsA proteins, which are embedded in the membrane. Interestingly FtsA forms, by polymerising, helical filaments on the membrane [84]. First, it was thought that when these proto-filaments are connected, they form rings in the center of the cell. These rings are the so-called FtsZ Rings (see Fig 1.10). Nonetheless, it is nowadays thought that the polymerisation of the FtsZ proteins leads to the formation of close-pitched helices [85, 86].

In vivo, FtsZ proteins, in addition to a dozen other proteins, are involved in cell division. In particular, FtsZ Rings are the first filaments recruited to divide the cell. As a first step, it constricts the cell. Indeed, FtsZ proteins display two states. Due to this characteristic, proto-filaments also display multiple states. The two extreme cases occur when all proteins are in the same state. The proto-filaments can be straight, highly curved or display intermediate configuration between these two extreme cases. The mechanism of force generation comes from the switch from the straight to the curved conformation. Similarly to the case of dynamin, it is the hydrolysis of GTP that gives the energy necessary for the change of conformation.

1.2.2 The Worm-Like Chain model

Similarly to the bending modulus of membranes, the bending stiffness is one of the most important physical property of bio-filaments, and has been widely studied experimentally [88, 89, 90, 91]. Fig. 1.11 shows the effect of the bending stiffness on the shape of three of the main bio-filaments found in eukaryotic cells. One clearly sees differences between them. Indeed, the microtubule seems to be stiff, and rod-like, while actin is a bit wavy and the intermediate filament seems completely soft and looks like a ball of wool. The following subsection will be dedicated to the discussion about one of the most used model to describe the elasticity of bio-filaments.

Theoretical models describing these filaments often consider that the interactions between the subunits are averaged or smoothed away. This approximation allows to treat the bio-filaments as thin elastic rods. One of the simplest model generally used is the Worm-Like Chain (WLC) [92]. The general form of the WLC Hamiltonian is written as a function of the curvatures $\Omega_{1/2}$ and twist Ω_3 as:

$$E_{WLC} = \frac{1}{2}\int_0^L \left(B_1(\Omega_1 - \omega_1)^2 + B_2(\Omega_2 - \omega_2)^2 + C(\Omega_3 - \omega_3)^2\right) ds, \tag{1.8}$$

where B_1, B_2 are the two bending stiffness and C is the torsional stiffness. $\omega_{1/2}$ and ω_3 respectively are the intrinsic curvatures and twist. Finally ds is the infinitesimal length unit of the filament of total length L. In polymer science, the quantities of interest are not the bending and torsional stiffnesses, but quantities directly linked to them and known as the persistence lengths. These are lengths over which the tangential correlations of the filament are lost (see Appendix A.3). For distances smaller than the persistence length, the filament is considered as a rod, while for larger distances, the filament seems floppy. It is possible to rewrite the stiffness as a function of these lengths as (see Appendix A.3):

$$\begin{aligned} B_{1,2} &= l_{p,1/2}\ k_B T \\ C &= l_t\ k_B T, \end{aligned} \tag{1.9}$$

where $l_{p,1/2}$ are the two persistence lengths for bending and l_t is the persistence length for twisting.

The filaments discussed previously, such as DNA, actin, microtubules and intermediate filaments were described even more simply. Indeed, one first considers that these filaments do not spontaneously twist, and are isotropic, such that whatever the direction they curve in, the energy cost is the same. The two persistence lengths for bending are thus equal and the twist term is null. In addition, as a last simplification one can study this kind of filaments confined in a two dimensional plane such that it can bend only in one of the two discussed directions (with positive or negative curvature). We call this persistence length for bending l_p. The expression of the energy given in Eq. 1.8, thus can be simplified, for a straight filament (no spontaneous curvature) as:

$$E_{fil} = \frac{l_p\ k_B T}{2}\int_0^L \kappa(s)^2 ds. \tag{1.10}$$

One sees in Fig. 1.11 that the distance between both ends is strongly affected by the stiffness of the filaments. In the limit of the WLC model, the mean square end-to-end distance $\langle R^2 \rangle$ reads (see Appendix A.3):

$$\langle R^2 \rangle = 2l_p^2 \left(\frac{L}{l_p} + e^{-L/l_p} - 1\right), \tag{1.11}$$

where $\langle ... \rangle$ denotes a thermal average. In the limit of $L/l_p \ll 1$, $\langle R^2 \rangle \approx L^2$, such that the filament is rod-like, similarly to microtubules. In the opposite limit of $L/l_p \gg 1$, $\langle R^2 \rangle \approx 2l_pL = Nb^2$, with effective bond length $b = 2l_p$, corresponding to the Kuhn length [93]. The filament adopts a random-walk conformation, similarly to intermediate filaments. Under physiological conditions, the persistence length of the latter filaments have been experimentally measured. For instance, for microtubules, 0.1 mm $< l_p <$ 5 mm [88, 90], for intermediate filaments, $l_p \approx 1\mu$m [89], for actin, $l_p \approx 17\mu$m [88, 91] and for double-stranded DNA, $l_p \approx 150$ bps (base pairs) ≈ 50 nm [94].

However, biological filaments can display a behavior more complex than that of straight standard semi-flexible chains described by the WLC model. In many cases, *in vivo* and *in vitro*, bio-filaments manifest heterogeneities of different origin. For instance, in the last two decades, there has been strong evidence that some bio-polymers have individual subunits which can fluctuate between different conformations leading to very unusual mechanical behavior. This kind of switchable multistable filament is abundant in the biological realm. In particular, FtsZ [66, 67], MreB [71], actin [51, 52, 53, 54] and microtubule which shows a very exceptional mechanical and dynamical behavior [56, 57, 95], the confotronic dynamics recently introduced [58], are switchable. Other remarkable examples of such polymorphic filaments are the bacterial flagella [96, 97] and the spiroplasma [98, 99, 100, 101].

Among many interesting and important questions, one tries to understand how bio-filaments and biological membranes interact. For instance, one tries to understand how membranes fission. In eukaryotic cells, actin interacts with the cell membrane, while in prokaryotic cells, FtsZ plays the same role as actin. Another example is during endocytosis, in order to let molecules cross the membrane, dynamin deforms the membrane and cuts it. Such phenomena have been widely studied theoretically and experimentally [62, 63, 68, 102, 103, 104]. However, the previous works did not take into account that filaments can display a more complex behavior than simple semi-flexible chains.

In Chapter 2, we discuss the collective mechanical behavior of coupled non-linear monomer units entrapped in a circular filament. The phenomenon, that we term polymorphic crunching, is discussed and applied to a possible scenario for membrane tube deformation by switchable dynamin or FtsZ filaments.

In Chapter 3, we study the deformations of a fluid membrane imposed by adhering stiff bio-filaments due to the torques they apply. In the limit of small deformations, we derive a general expression for the energy and the deformation field of the membrane. This expression is specialized to different important cases including closed and helical bio-filaments. In particular, we analyse interface-mediated interactions and membrane wrapping when the filaments apply a local torque distribution on a tubular membrane.

Finally, in Chapter 4, we discuss the motility of eukaryotic and prokaryotic cells. In particular, we focus on the Spiroplasma bacterium, which is helically-shaped and displays a bacterial cytoskeleton and lacks a cell wall. We discuss the ingredients of the theory we want to develop in the future to understand the motility of this bacterium.

Chapter 2

Polymorphic biofilament rings

In this chapter, we pose the following conceptual question: What happens when protein monomers with an intrinsic curvature form a stiff polymer which is forced to close in a ring of different curvature radius ? We first give the conditions for the emergence of multi-stability. Then we describe the model, giving rise to the degeneracy of the ground state and to a softening of the ring through prestrain. Finally, we apply this model to a possible mechanism of membrane fission.

2.1 Emergence of multi-stability

The WLC model discussed in the introduction can describe a multitude of filaments, which are not necessarily simple. For instance, it can describe intrinsically twisted and curved filaments. Nonetheless, this continuous linear model does not take into account the possible multi-stability of the constituent subunits. In this model, the subunits only have one preferred state of curvature. What would happen if the subunit constituents of the filament were multi-stable and could switch between several states?

Let us consider two simple situations, where multi-stability and switchability of coupled subunits arise. Consider N identical elastic subunits described by their curvature κ_i. Each subunit has a corresponding elastic energy $f\left(\kappa_i\right)$, where the function f has a global minimum at the curvature $\kappa_i = \kappa_m$, corresponding to the intrinsic curvature of the subunit. Note that in this general setting, subunits can be mono-stable or multi-stable.

As a first example, consider these N monomers mechanically coupled in the plane perpendicular to their bending axis (see Fig. 2.1 (a)). On the one hand, for intrinsically straight monomers $\kappa_m = 0$ (in Fig. 2.1 (a), this corresponds to straight rectangular subunits), such a coupling results in the formation of a slice of tube of circular cross-section. In this particular configuration, all monomers are in their ground state. On the other hand, for intrinsically curved monomers ($\kappa_m \neq 0$), the cylindrical tube bends in the direction orthogonal to the cross section and displays an apparent curvature κ_{tube}. Similarly to the case of straight monomers, due to the closure constraint, not all monomers display their preferred curvature. Indeed, if all subunits bend such that their energy is minimal, *i.e.*, with curvature κ_m, the closure condition is not respected all along the bending axis. The

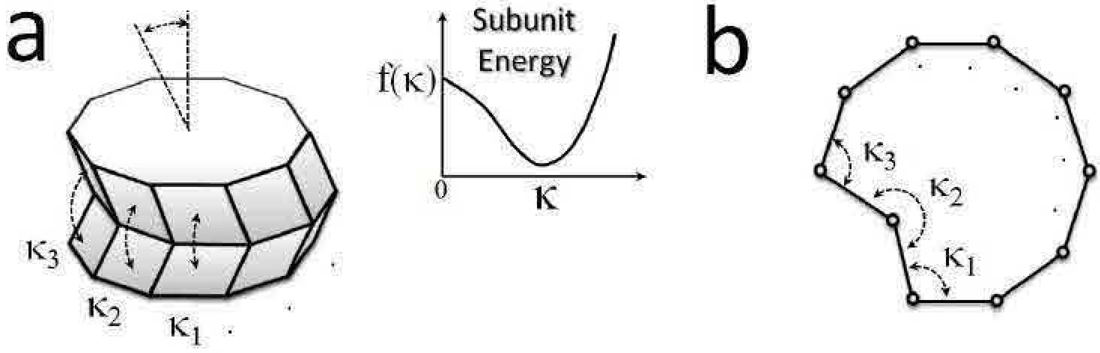

Figure 2.1: Two simple types of collective coupling between non-linear units, with curvature κ_i and bending energy f(κ_i), via a global constraint. a) Polymorphic buckling as found in bacterial flagella and microtubules. Bendable units are coupled in the plane perpendicular to their bending axis [56, 57, 58]. Note that for a cylindrical tube, *i.e.*, for $\kappa_{tube} = 0$, all subunits are frustrated with $\kappa_i = 0$. b) Polymorphic crunching, described in more details in this chapter. Non-linear bendable units are coupled in-plane of bending by a ring closure constraint.

subunits curvature can be approximated at first order by:

$$\kappa_i \approx \kappa_{tube} \cos\left(\frac{2\pi i}{N}\right), \tag{2.1}$$

as a result of the projection of the tube's curvature on each subunit. The elastic energy of the slice of tube is the sum of the energy of all the subunits such that:

$$E_{tube}(\kappa_{tube}) = \sum_{i=1}^{N} f\left(\kappa_{tube} \cos\left(\frac{2\pi i}{N}\right)\right). \tag{2.2}$$

Let us consider for instance the case of two subunits ($N = 2$). The energy of such a system then is:

$$E_{tube} = f(\kappa_{tube}) + f(-\kappa_{tube}). \tag{2.3}$$

As the sides of the constituents must be in contact, the two subunits lie on each other and are "welded". Assuming that the subunits are symmetric, such that bending with a curvature ±κ costs the same energy, we can rewrite the energy as follows: $E_{tube}(\kappa_{tube}) = 2f(\kappa_{tube})$. More generally, the energy, due to the symmetry of the system only depends on even terms of the function f, if the number of subunits is even itself ($N = 2k$, where $k \in \mathbb{N}$) . In such a case, the system is expected to present at least three equilibrium states. The two symmetric curved states $\langle\langle$ and $\rangle\rangle$, but also the straight state $\|$. According to the energy profile given in Fig. 2.1, the two bent states are supposed to be stable states, while the straight one is unstable. This is only possible if $\left.\frac{\partial^2 f}{\partial \kappa^2}\right|_{\kappa=0} < 0$. Note that for a more general energy profile, subunits might display N stable bent states and $N-1$ unstable states. This symmetry breaking permits the emergence of a multi-stability (in this precise example a bi-stability), which is the basic motif in switchable tubular systems. In particular, this is of interest for microtubules [56, 57, 58] and bacterial flagella [105, 106, 107, 108].

As a second example, which is even simpler than the previous one, consider subunits coupling to each other in their plane of curvature (see Fig. 2.1 (b)). The following question arises: what happens when a chain made of such subunits is closed in a planar ring?

Like in the previous studied case, let us start from a general setting which will be specialised to the particular model we developed. let us consider N_0 monomers of size a, having energies that are function of their intrinsic curvatures κ. Again, the elastic energy of a single monomer is given by a function of the curvature $f(\kappa)$. The elastic energy of the filament also corresponds to the sum of all the energies of each monomer. Nonetheless, another term might play an important role on the shape of the filament. This is the cooperative energy. Indeed, many filaments, including dynamin and FtsZ among others are known to switch cooperatively. In the following, although cooperativity often plays an important role, we first neglect this coupling between neighbour monomers, and we will introduce cooperativity later. Thus, we assume that the formation of domains of same curvature along the filament ring is not favoured.

In the limit of N_0 large, or small size a of the monomers, the summation can be replaced by an integral over the length, such that the energy reads:

$$E_{ring} = \int_0^{L_0} f\left[\kappa(s)\right] ds, \tag{2.4}$$

where $L_0 = N_0 a$ and ds is the arc-length element along the filament. Note that for a linear filament described by the WLC model, $f\left[\kappa(s)\right] \propto (\kappa - \kappa_1)^2$, where κ_1 is the intrinsic curvature of the subunit. The ground state of such a closed filament ring is a circular ring of curvature $\kappa = \kappa_1 = \frac{2\pi}{L_0}$. Also note that in this case, the curvature of the circle corresponds to the intrinsic one.

If we now take another number of monomers N and enforce them to close in a ring with mean curvature $<\kappa>= \kappa_0 = \dfrac{2\pi}{L}$, where L is the length of the filament, the ground state will not be a circle of curvature κ_1 but a deformed circle. Assuming the shape of the ring close to the circular state, such that the curvature of the ring reads $\kappa(s) = \kappa_1 + \delta\kappa(s)$, where $|\delta\kappa| \ll |\kappa_1|$, the elastic energy can be expanded in the following way:

$$E_{ring} = E_0 + \sum_{n=1}^{N_{max}} \frac{1}{n!} \left.\frac{\partial^n f}{\partial \kappa^n}\right|_{\kappa=\kappa_0} \int_0^L \delta\kappa^n ds, \tag{2.5}$$

where E_0 corresponds to the energy of the circular ring, and N_{max} corresponds to the highest order term in $\delta\kappa$ retained.

2.2 The model

For the sake of concreteness, let us study monomers described by a non-linear elastic energy density, which is given by:

$$f(\kappa) = A\kappa - \frac{B}{2}\kappa^2 + \frac{C}{2}\kappa^4, \tag{2.6}$$

where A, $B > 0$ and $C > 0$ are elastic constants, whose signs are taken in such a way that at least one stable preferred curvature state exists. Moreover, the constant A represents an asymmetry of the monomer, which has an inner part and an outer one. The term proportional to κ^2 is always negative (meaning that $B > 0$) to fulfil the condition that the straight state is unstable. For A large enough, the bi-stable monomer becomes mono-stable with preferred curvature $\kappa_1 \approx -\left(\frac{A}{2C}\right)^{1/3}$ (Fig. 2.2 (a)). Note that the term in κ^3 has not been taken into account for simplicity.

For a polymer chain, in the continuous limit, for a large number of monomers ($N \gg 1$), the elastic energy becomes

$$E_{elastic} = \int_0^L f(\kappa)ds, \tag{2.7}$$

where $s \in [0, L]$ is the arclength variable. Note that this equation holds even for non-closed polymer.

If we now choose to force the polymer to close, this imposes two constraints. The first one is a constraint on the continuity of the tangent angle $\theta(s)$, where the curvature and the tangent angle are linked by the following relation $\kappa(s) = \frac{d\theta}{ds}$. To close the ring without kink, the tangent angle (which is continuous along the filament) must be equal to 2π such that $\theta(L) - \theta(0) = 2\pi$. The second one, is imposed by the closure condition of the ring. The x and y-components have to be the same at the beginning and at the end of the polymer:

$$\int_0^L \cos\theta(s)ds = \int_0^L \sin\theta(s)ds = 0. \tag{2.8}$$

Outstandingly, if we implement the constraint on the tangent angle θ in the elastic energy (Eq. 2.7), the asymmetric term, *i.e.*, the linear term in κ just gives a constant when integrated over the whole curve :

$$\begin{aligned} \int_0^L A\kappa ds &= A\int_0^L \frac{d\theta}{ds}ds \\ &= A\left(\theta(L) - \theta(0)\right) \\ &= 2\pi A. \end{aligned} \tag{2.9}$$

Interestingly, if we take $A = 0$, there is no change in the variation of the energy, and in the ring's shape as compared to the state where $A \neq 0$. This means that without any change of physics for the whole ring we could have chosen $A = 0$ from the beginning. Nonetheless there is a subtle but important difference in interpretation of the physics of the monomer itself. Indeed, if we take $A = 0$, we don't have any more mono-stable monomers, but bi-stable ones (with two equivalent energy minima) (Fig. 2.2(b)). With

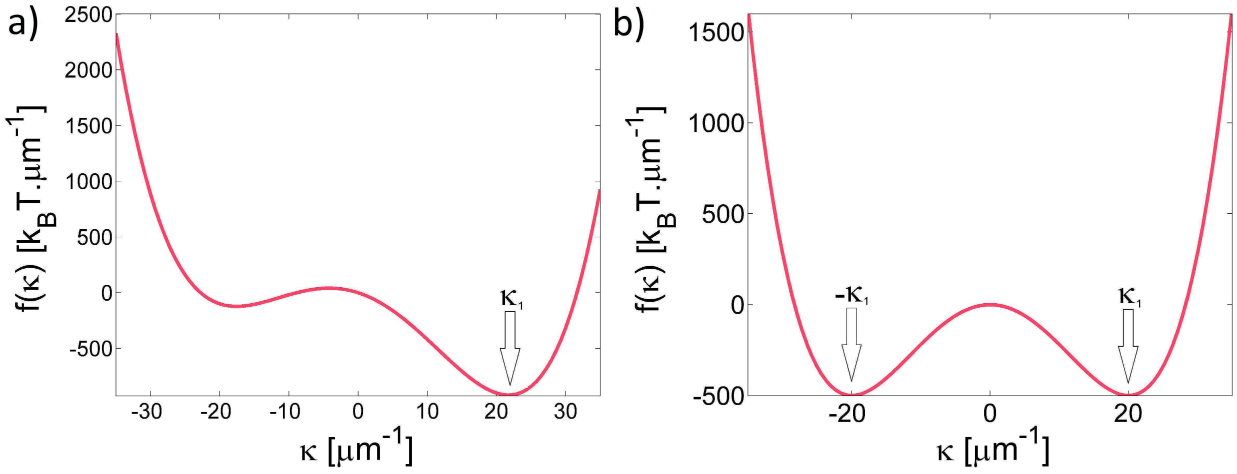

Figure 2.2: Profile of the monomer's energy with respect to the curvature κ. For a), the parameters are $A = -20k_BT$, $B = 5k_BT.\mu\text{m}$ and $C = 1/160k_BT.\mu\text{m}^3$ and $\kappa_1 \approx 21.76\mu\text{m}^{-1}$. For b), the parameters are $A = 0k_BT$, $B = 5k_BT.\mu\text{m}$ and $C = 1/160k_BT.\mu\text{m}^3$ and $\kappa_1 = 20\mu\text{m}^{-1}$. For a monomer of size $a = 10$ nm, the barrier is equal to $5k_BT$.

$A \neq 0$, the monomers might have only one preferred curvature while with $A = 0$, the function describing the bending energy being an even function, the monomers have two symmetric preferred curvatures, one positive and another one negative ($\pm\kappa_1$). The closure condition implies that the initially mono-stable monomers act as if they were bi-stable ones. The linear term can thus be discarded, and we end up with an effective total energy of the ring :

$$E_{elastic} = \int_0^L E_{eff}(\kappa)ds, \quad \text{where} \tag{2.10}$$

$$E_{eff} = -\frac{B}{2}\kappa^2 + \frac{C}{2}\kappa^4, \tag{2.11}$$

where the new B and C are different from the one given in the equation of E_{mono} (Eq. 2.6) in order to have the same value of the preferred curvature κ_1. Note that with the corresponding effective energy, there are always two minima $\kappa = \pm\kappa_1$, where $\kappa_1 = \sqrt{\dfrac{B}{2C}}$ and $E_{eff}(\kappa_1) = -\dfrac{1}{8}\dfrac{B^2}{C}$. Notedly, it is the chain closure, that generates a bi-stability of the monomers.

Suppose now that the monomers, due to temperature, display thermal elastic fluctuations $\delta\kappa_{el}(s)$, where $|\delta\kappa_{el}(s)| \ll |\kappa(s)|$. The curvature of the monomers is now given by $\kappa(s) = \pm\kappa_1 + \delta\kappa_{el}(s)$, and the energy, expanded up to quadratic order is :

$$E_{elastic} = -\frac{L}{8}\frac{B^2}{C} + B\int_0^L \delta\kappa_{el}^2 ds, \tag{2.12}$$

which corresponds to the same formula as the one of the ring given in the previous section (Eq. 2.5). From this equation, it is possible to define a purely elastic persistence length for the system $l_B = \frac{2B}{k_B T}$, where k_B is the Boltzmann constant, and T is the temperature. However, we will see in the following parts that a purely entropic contribution due to the degeneracy of the ground state will also have to be taken into account.

2.3 (Infinite) degeneracy of the ground state and crunching transition

As shown in the previous part, the elastic energy can be written as a function of the effective energy of the monomers $E_{effective}$ (Eq. 2.11). This energy profile being symmetric, it has two stable states $\kappa(s) = \pm\kappa_1$, giving rise to a multiple number of ground states, increasing with the number of monomers. The monomers can have one of these two curvatures, without any difference in energy.

In this part, we work in discrete notation, where each element corresponds to a monomer. In this case, the curvature of the n-th monomer can be written as $\kappa_n = \sigma_n \kappa_1$, where the "spins" $\sigma_n = \pm 1$, and $n = 1, ..., N$. For an open filament described by the elastic energy given for symmetric monomer energy (Eq. 2.10), the system is formally equivalent to a one-dimensional Ising chain without interactions between the spins. In analogy to the latter model, at a finite temperature, we introduce the "average magnetization"

$$M = \frac{1}{N} \sum_{n=1}^{N} \sigma_n, \tag{2.13}$$

describing the mean value of the distribution of positively and negatively curved monomers such that $< \kappa_n >= \kappa_1 M$. Note that $-1 \leq M \leq 1$. Indeed, if all the monomers are negatively curved, $M = -1$, while if they all are positively curved, $M = 1$. Between these two values, there are n_+ monomers positively curved, and n_- negatively curved, such that $N = n_+ + n_-$. For a given value of M, the free energy $F(M) = E_{elastic} - TS(M)$ decomposes into the elastic energy (Eq. 2.12) and the entropic contribution $S(M) = k_B \ln W(M)$, where $W(M) = \frac{N!}{n_+! n_-!}$ is the number of ground states for a given M. Note that the elastic thermal fluctuation contributions $\delta\kappa_{el}$ around the ground states average to $< \delta\kappa_{el} >= 0$ and only adds a constant term to the free energy, and can thus be disregarded. The physical value of M is given by the minimum of the free energy $F(M)$, when $\frac{dF(M)}{dM} = 0$, which is when the entropy is maximum, if all monomers are in their preferred state. In other words, this is the case when the number of ground states $W(M)$ is maximum, which is obviously when $M = 0$ for an open filament. This implies that, although degenerate and locally tortuously bent, the ground states, for an open filament, are statistically straight on average. The closure constraint induces a competition between the entropic and the elastic terms.

Similarly to the open filament, the closed ring also has a high number of ground states (Fig. 2.3). Its degeneracy is less important due to the constraints it has to adapt to. Indeed, the non-linear closure constraints (Eq. 2.8) introduce a weak non-local effective coupling between the individual monomers. Besides, as the ring has to close, its mean curvature $< \kappa_n >$ has to satisfy the following condition $< \kappa_n >= \kappa_0$. Solving this problem with the

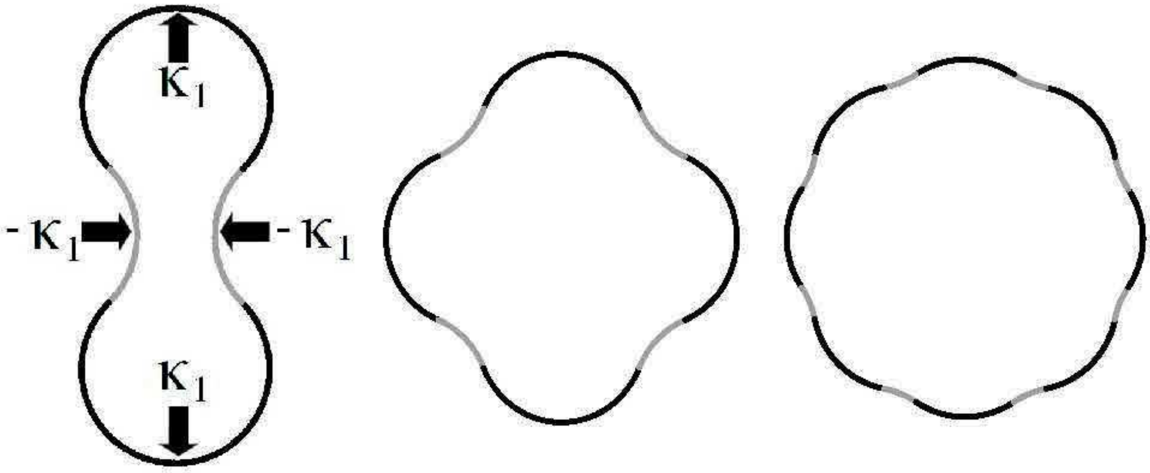

Figure 2.3: Crunching of a circularly closed non-linearly elastic filament for $\kappa_0/\kappa_1 = 0.5$. A ground state consists of a sequence of positive and negative curvature regions. All depicted states are ground states and have the same elastic energy

non-linear closure constraints is a rather difficult task, but it is possible to simplify the problem to illustrate the degeneracy of the ground state. If we consider that the curvature $\kappa(s)$ displays a four-fold symmetry with the x and y axes, then the closure is ensured by symmetry. It is now possible to cut in quarters the ring and treat only one of these quarters with $\frac{N}{4}$ monomers each.

Like in the open filament case, the free energy is given by $F(M) = E_{elastic} - TS(M)$, but in this case, even if we still can neglect the elastic fluctuations, the monomers do not need to exactly have a curvature $\kappa(s) = \pm\kappa_1$, but can move away from the minimum of the effective potential. Indeed, in this case, even if it costs energy to go away from the minimum, the entropy contribution can counterbalance this cost. The addition of a deviation in the curvature Δ_κ to the preferred curvature κ_1 leads to a total curvature for each monomer such that $\kappa_n = \sigma_n\kappa_1 + \Delta_\kappa$. This addition in the elastic energy helps the system to reach more configurations than for $\Delta_\kappa = 0$, thus increasing the entropy. With this expression for the curvature, it is possible to rewrite the “mean magnetization” of the ring, *i.e.*, the angular closure constraint, as follows

$$M = \frac{n_+ - n_-}{N} = \frac{4}{N}\sum_{n=1}^{N/4}\sigma_n = \frac{\kappa_0 - \Delta_\kappa}{\kappa_1}. \tag{2.14}$$

Note that due to the closure constraint, the “mean magnetization” can not be negative any more, *i.e.*, $0 \leq M \leq 1$. Moreover, if $\kappa_1 < \kappa_0$, Δ_κ is necessarily non-zero in order to have $M < 1$.

Let us go back to the free energy of the system $F = E - TS$. As previously, E is the elastic energy and $S(M) = k_B \ln W(M)$ is the entropy of the system, where $W(M)$ is the number of states which has now to fulfil the previous condition (Eq. 2.14). Note that when the energy dominates over the entropy (small T or small N), the parameter $\Delta_\kappa \approx 0$, while when the entropy becomes comparable to the energy, there is a compromise between these two quantities such that Δ_κ can become large. The minimisation of the free energy leads to the following self-consistent equation (for more details on the calculation, see appendix B.1):

$$\Delta_\kappa = \frac{\kappa_0 - \kappa_1 + (\kappa_0 + \kappa_1)\exp(-\epsilon)}{1 + \exp(-\epsilon)}, \tag{2.15}$$

where

$$\epsilon = \frac{2aB\Delta_\kappa}{k_B T \kappa_1}(2\kappa_1^2 + 3\kappa_0\Delta_\kappa - 3\Delta_\kappa^2). \tag{2.16}$$

For a very stiff filament, *i.e.*, when $B = \frac{l_B k_B T}{2} \gg \frac{k_B T}{a\kappa_1^2}$, the energy cost to change curvature is huge compared to the gain from entropy such that the value of Δ_κ jumps sharply from $\Delta_\kappa = \kappa_0 - \kappa_1$ for $\frac{\kappa_0}{\kappa_1} > 1$ to $\Delta_\kappa = 0$ for $\frac{\kappa_0}{\kappa_1} < 1$ (see Fig. 2.4 (a), blue curve). Interestingly, for very stiff filaments, $\Delta_\kappa = 0$ always corresponds to a minimum of free energy (for instance, for $\alpha = \kappa_0/\kappa_1 = 0$ and $\epsilon_1 = 1000$, see Fig. 2.4 (b)). Nonetheless, due to the closure constraint, the magnetization (see Eq. 2.14) must be comprised between 0 and 1, such that $0 < \alpha - \beta < 1$, where $\beta = \Delta_\kappa/\kappa_1$. This implies that for an α given, the study of the free energy must be restricted to the interval $\alpha - 1 < \beta < \alpha$. For $\alpha < 1$, the minimum of the free energy for $\Delta_\kappa = 0$ can be reached, but this is not possible for $\alpha > 1$. The free energy increasing monotonously (before reaching a maximum of free energy, which is never in the interval for closed filaments), the minimum of free energy is for $\beta = \alpha - 1$, *i.e.*, for $\Delta_\kappa = \kappa_0 - \kappa_1$.

Let us implement these values in the expression of the "mean magnetization" to see what it exactly means. For $\frac{\kappa_1}{\kappa_0} < 1$, the "mean magnetization" $M = 1$, which means that all the constituent units of the filament are positively curved, *i.e.*, the filament stays a ring with $\kappa = \kappa_0$. For a non-closed filament, all monomers would have a curvature $\kappa = \pm\kappa_1$, nonetheless this is not the case any more in the closed state as the closure constraint would not be fulfilled. In order to still have the system in its minima of energy, monomers are frustrated and take a value of $\kappa = \kappa_0$. For $\frac{\kappa_1}{\kappa_0} > 1$, the "mean magnetization" $M = \frac{\kappa_0}{\kappa_1}$, which means that some of the constituent units of the filament are positively curved while the others are negatively curved with $|\kappa| = \kappa_1$. The filament stays a ring below the transition ($\frac{\kappa_1}{\kappa_0} < 1$), and is crunched above it.

For very soft filaments, *i.e.*, $B \ll \frac{k_B T}{a\kappa_1^2}$, monomers can change their curvature without paying much energy, allowing at the same time a higher gain due to entropy. Filaments thus are always crunched even for $\frac{\kappa_1}{\kappa_0} < 1$ (see Fig. 2.4 (a), red curve). Finally, for more moderate stiffnesses $B \lesssim \frac{k_B T}{a\kappa_0^2}$, the system more gradually interpolates between un-crunched and crunched state, and the transition smoothens increasingly with decreasing bending stiffness B (see Fig. 2.4 (a), purple curve).

From this mean field analysis, we understand that the local curvature can deviate from its preferred value ($\pm\kappa_1$) by a certain amount Δ_κ, in such a way that the free energy of the

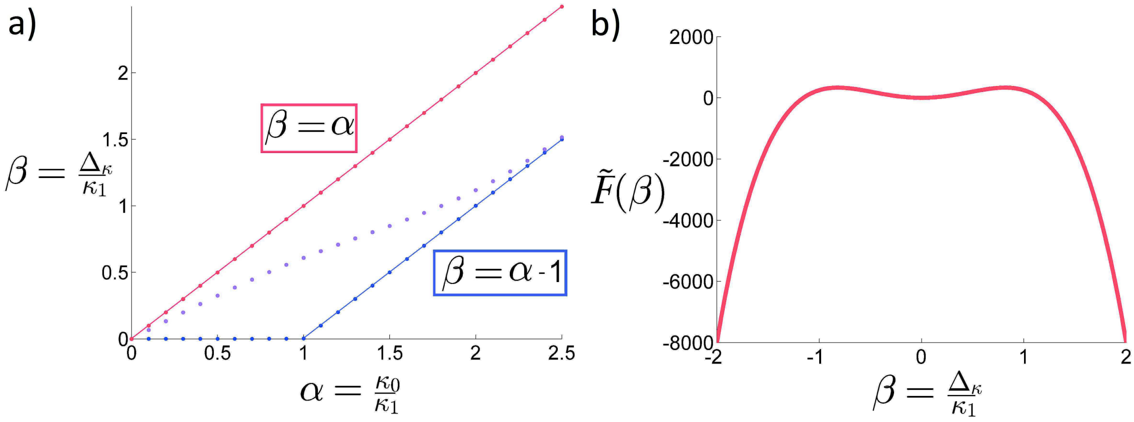

Figure 2.4: (a) Plot of the curvature fluctuations Δ_κ rescaled by monomer's curvature κ_1 as a function of the rescaled ring curvature $\alpha = \kappa_0/\kappa_1$ for different values of $\epsilon_1 = (Ba\kappa_1^2)/(k_BT)$. The blue curve corresponds to stiff filaments ($\epsilon_1 = 1000$), whereas red curve corresponds to soft filaments ($\epsilon_1 = 10^{-3}$). Finally, a filament with intermediate stiffness ($\epsilon_1 = 0.5$) is represented by the purple curve. (b) Example of a plot of the free energy of very stiff filaments as a function of β for $\alpha = 0$ and $\epsilon_1 = 1000$.

system is minimal. Due to this change of curvature, the filament which classically crunches (at $T = 0$) when $\kappa_1 > \kappa_0$, can "pre-crunch" even for $\kappa_1 < \kappa_0$.

2.4 Persistence length : softening through prestrain

In Sec. 2.2, we defined a purely elastic persistence length $l_B = \frac{2B}{k_BT}$, nonetheless as said in Sec. 2.3, we are interested in the free energy which depends on the entropy of the system, corresponding to the presence of exponentially many equivalent ground states. In this section, we will discuss the impact of the entropic contribution on the persistence length of closed filaments.

As already mentioned, calculating the number of ground states for a given value of the preferred curvature of monomers κ_1 is a rather difficult task, due to the closure condition (Eq. 2.8) which results in a weak non-local coupling between the individual monomers. Nonetheless, we circumvented the closure coupling by studying the four-fold symmetry case. In this section, this coupling will be treated more elegantly later on by eliminating certain Fourier modes in a coarse-grained filament description. Moreover, we consider the ring formed by a large number of bi-stable monomers, $N \gg 1$ and a stiff filament, such that the "phase transition" between crunched and un-crunched states is sharp. The study is done for rings of smaller curvature than the monomer's one ($\kappa_1 > \kappa_0$), such that the additional curvature Δ_κ defined in the previous section is null.

To enforce the closure condition (Eq. 2.8), we consider the Fourier decomposition of the tangent angle θ around the circular state, *i.e.*, $\theta(s) = \theta_0 + \delta\theta(s) = \kappa_0 s + \delta\theta(s)$, where

$$\delta\theta(s) = \sum_{n=1}^{N_{max}=N/2} (a_n^\theta \sin(\kappa_0 n s) + b_n^\theta \sin(\kappa_0 n s)). \tag{2.17}$$

Note that $N_{max} \neq N$. Indeed, N_{max} can't be larger than $N/2$ because on the small scale, it is impossible to have more variations in curvature than the number of monomers itself. It means that in an oscillation of the latter sine or cosine functions, there is a minimum of 2 monomers. Furthermore, we impose the ring conformation on average, *i.e.*, $< \kappa_n >= \kappa_0$, such that the "spins" σ_n can be considered as randomly distributed around an average value $< \sigma_n >= M$ (Eq. 2.14).

For a large number of monomers N, the piecewise function $\kappa_n = \pm\kappa_1$ satisfies the central limit theorem, such that the probability to find a curvature $< \kappa_n >_l$ on a length l is a Gaussian variable, where $a \ll l \ll Na = L$. This coarse-grained length must be larger than the monomer size, but must remain smaller than the total length, *i.e.*, smaller than the ring. Using this coarse-grained approach, which is valid on the scale defined above, we treat the curvature as a continuous Gaussian-distributed function $\kappa(s)$. It is more convenient to introduce a new random Gaussian variable $\tilde{\kappa}(s) = \kappa(s) - < \kappa(s) >= \kappa(s) - \kappa_0$ with zero mean value and a standard deviation $< \tilde{\kappa}^2(s) >= \kappa_1^2 - \kappa_0^2 \overset{(2.14)}{=} \kappa_1^2(1 - M)$. Moreover, since the curvature is uncorrelated on larger scales, the correlation function is $< \tilde{\kappa}(s)\tilde{\kappa}(s') > \approx \delta(s - s') < \tilde{\kappa}^2(s) >$ for $|s - s'| \gg l$. Rewritten in this form, the filament can be seen as a standard semi-flexible chain as the coarse-grained curvature $\tilde{\kappa}(s)$ behaves on larger scales as the curvature of a semi-flexible chain. The latter can be described by the Worm-Like Chain (WLC) model with an effective configurational free energy

$$F_{WLC} = \frac{l_e k_B T}{2} \int_0^L \tilde{\kappa}^2(s) ds, \tag{2.18}$$

where the effective persistence length is given by a study of the standard deviation. First of all, we need to expand the X-Y constraints (Eq. 2.8) to lowest order in modes a_n^θ and b_n^θ

$$\int_0^L \sin(\theta_0)\delta\theta ds = 0 \quad \text{for the X component} \tag{2.19}$$

$$\int_0^L \cos(\theta_0)\delta\theta ds = 0 \quad \text{for the Y component,} \tag{2.20}$$

leading to the vanishing of a_1^θ and b_1^θ. The higher modes are unaffected and according to the equipartition theorem ($< F_{WLC} >= d\frac{k_B T}{2}$ where d is the number of degrees of freedom of the system), they satisfy the following equation

$$< (a_n^\theta)^2 >=< (b_n^\theta)^2 >= \frac{L}{2\pi^2 l_e} \frac{1}{n^2}, \tag{2.21}$$

which are temperature-independent due to purely entropic effects. Finally, we can implement these values in Eq. 2.17 and compare it to the expression of the standard deviation given above $< \tilde{\kappa}^2(s) >= \kappa_1^2 - \kappa_0^2$. We end up with this expression for the effective persistence length

$$l_e = \frac{1}{a(\kappa_1^2 - \kappa_0^2)}. \tag{2.22}$$

Even if this analogy with the WLC is useful, some care has to be taken with this particular result. First of all, the persistence length is temperature-independent since it is associated to a conformational entropy of the ground state. Secondly, unlike polymers described by the WLC, the persistence length l_e depends on the total length of the filament L through $\kappa_0 = \frac{2\pi}{L}$. From Eq. 2.22, one sees that the effective persistence length l_e is decreasing for L increasing. The chain softens for increasing length L, until l_e reaches its minimal value $l_e^{min} = \dfrac{1}{a\kappa_1^2}$. Moreover, for a fixed length L, if the size of the monomers a is decreased, the number of monomers increases as $L = Na$. Increasing the number of monomers increases the number of closed realisations. Nonetheless, the number of states with shapes close to the circular ring increases more than the ones with large deviations from the circular state. Therefore, the shape fluctuations are reduced, and for $a \to 0$, they are null. Similarly, for $\kappa_1 = \kappa_0$, only one configuration is allowed, such that there are no fluctuations away from the circular shape, *i.e.*, $l_e \to \infty$. Finally, for an open chain, monomers freely chooses curvatures $\pm\kappa_1$, with $\langle\theta\rangle = 0$. For a filament of length L, the fluctuations from the mean θ value along the filament read: $\langle\theta^2(s)\rangle = \dfrac{\kappa_1^2 as}{2}$, such that $\langle\theta^2(L)\rangle = \dfrac{\kappa_1^2 aL}{2}$. In the two dimensional system studied $\langle\theta^2(L)\rangle = \dfrac{L}{2l_p}$, where the persistence length $l_p = \dfrac{1}{a\kappa_1^2}$. Accordingly, in the limit of $\kappa_0 \to 0$, one finds the same result. It is nonetheless important to note that for an open chain, the linear term in κ should be taken into account, and would thus modify slightly the latter result.

To get the total persistence length, it is necessary to include the elastic thermal fluctuations around the ground states to the entropic one, to finally get

$$l_p(L) = \frac{l_B l_e(L)}{l_B + l_e(L)} \tag{2.23}$$

which is always smaller than the persistence length l_B linked to thermal fluctuations acting on curvature (See Fig. 2.5).

We observe a decrease of the persistence length for increasing L, from $l_p^{max} = l_B$ for $\kappa_1 = \kappa_0$, to $l_p^{min} = \dfrac{l_B}{1 + a l_B \kappa_1^2}$. We also can see that the persistence length decreases when the prestrain κ_1 increases with respect to κ_0, which means that the filament softens with increasing prestrain. Moreover, according to Eq. 2.23, if l_B goes to infinity, the value of the persistence length of the filament still remains finite, with $l_p = l_e$, unlike for standard semi-flexible chain, where the persistence length would diverge.

2.5 Crunching of membrane tube

In order to illustrate our model, we study the deformations induced by a polymorphic filament on a tubular membrane. The main point of this section is to know if such a filament can crunch a membrane. Indeed, in Nature, we find many examples of filaments interacting with tubular membranes. For instance, dynamin which wraps around neuronal membrane

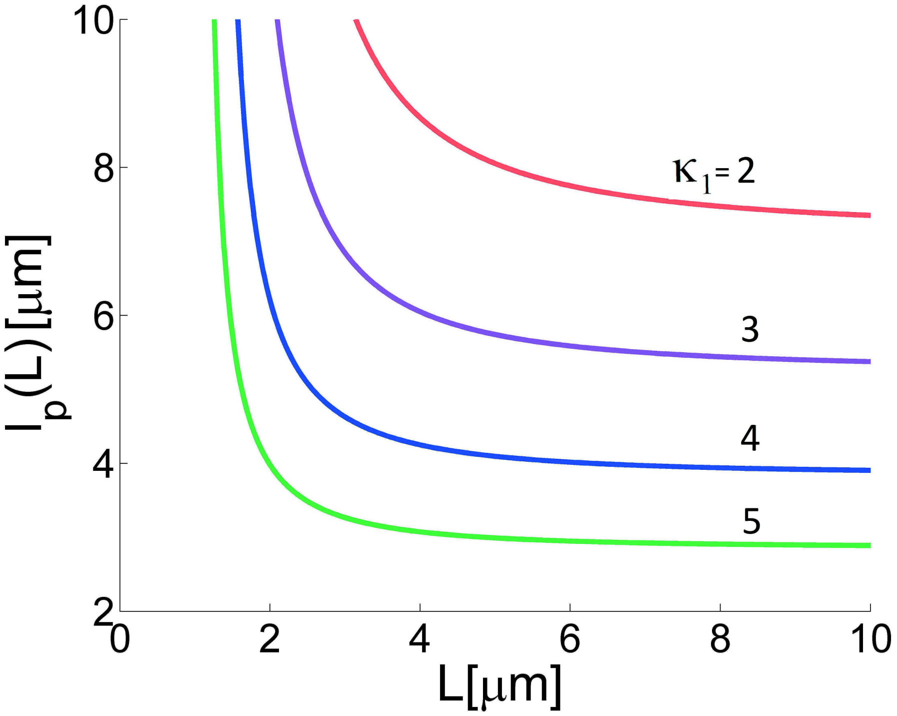

Figure 2.5: The persistence length l_p of crunched filament rings depends on their length (Eq. 2.23). The graph is plotted for $a = 10$ nm, $l_B = 10$ μm, $\kappa_0 = \frac{2\pi}{L}$ and for several polymorphic curvatures κ_1.

to form a helix whose pitch is small during endocytosis is one of the most prominent. FtsZ filament rings, *i.e.*, FtsZ filaments in their Z form, which constrict the membrane of bacteria during cell division are another example of interacting filaments. We do not pretend to solve these problems, but rather see our contribution as one more step in a better understanding of these interactions.

Let us consider a tubular fluid membrane of length L (which is assumed to be infinite below), radius R, and bending stiffness B_m. In the limit of small deformations with respect to the cylindrical state, the energy of the membrane, which is given in Ref. [103] at second order in the radial displacement field u and its derivatives reads:

$$E_{mem} = \iint e(\phi, z) d\phi dz, \tag{2.24}$$

with

$$e(\phi, z) = B_m \left((\partial_\phi^2 u)^2 + 3u^2 + 2R^2(\partial_z^2 u)(\partial_\phi^2 u) - 2R^2(\partial_z u)^2 + R^4(\partial_z^2 u)^2 + 4u(\partial_{\phi^2} u) \right) / (2R^3). \tag{2.25}$$

Note that more details on the stability of the tubular membrane will be given in next chapter. Moreover, like in Ref. [103], we assume that no longitudinal force is applied to the tube. The radial displacement field $u(\phi, z) \ll R$ (see Fig. 2.6) can be expressed as a

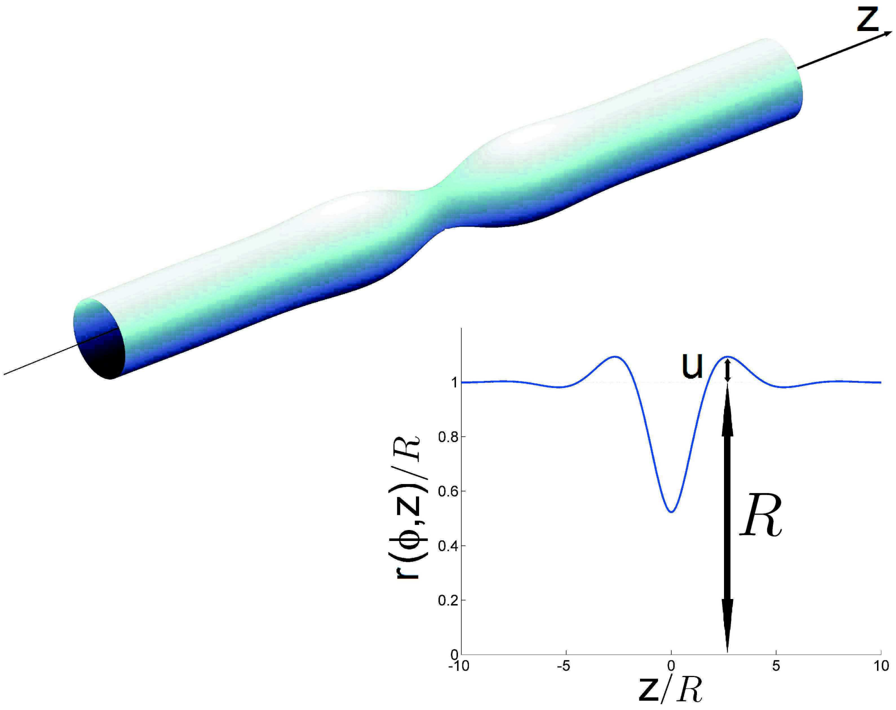

Figure 2.6: Representation of the deformed tubular membrane and the variables describing it, where $r(\phi, z) = R + u(\phi, z)$ is the radius of the tube which depends on the azimuthal angle ϕ and the longitudinal coordinate z. Note that in this figure the displacement is large (of the order of 40%). In the linear regime, the deformation (which is proportional to the applied forces or torques), should be of the order of few percent.

function of the azimuthal angle ϕ and the longitudinal coordinate z by:

$$u(\phi, z) = \sum_{n,m} A_{n,m} \exp(i(k_m z + n\phi)), \tag{2.26}$$

after Fourier modes expansion, where $k_m = \frac{2\pi}{L} m$. The mode n corresponds to the symmetry of the system. For example, for $n = 0$, the ring is circular and applies a local deformation to the tubular membrane. The mode $n = 1$ corresponds to a net external force which is absent in this problem. Indeed, it corresponds to a bending of the tube. The mode $n = 2$ corresponds to what we call the “peanut mode”, where the filament looks like a peanut, and so on. In principle, a crunched filament can display a non-symmetric shape, when described as the sum of different modes.

The energy of the membrane after including the radial displacement field given by Eq. 2.26 reads:

$$E_{mem} = \frac{\pi B_m L}{R^3} \sum_{|n| \neq 1} \sum_{m} M_{n,m} |A_{n,m}|^2, \tag{2.27}$$

where the elastic response function

$$M_{n,m} = (R^2 k_m^2 + n^2 - 1)^2 - 2(n^2 - 1). \tag{2.28}$$

When a polymorphic closed filament wraps around a tubular membrane, it induces a deformation at the position where it is located. In particular, for simplicity, in the case of only one closed filament on an infinite membrane, one can without loss of generality assume that the filament is at the position $z = 0$. The displacement field at this position reads:

$$u(\phi, z=0) = \sum_{|n|\neq 1} \sum_{m} A_{n,m} \exp(in\phi) \tag{2.29}$$

$$= \sum_{|n|\neq 1} a_n \exp(in\phi), \tag{2.30}$$

where $a_n = \sum_m A_{n,m}$ are the filament modes amplitudes. Using the method of Lagrange multiplier (for more details, see Appendix B.2), it is possible to rewrite the membrane modes $A_{n,m}$ as a function of the filament modes a_n. The energy then reads:

$$E_{mem} = \frac{\pi B_m L}{R^3} \sum_{|n|\neq 1} \frac{|a_n|^2}{I_n} \tag{2.31}$$

and

$$u(\phi, z) = \sum_{|n|\neq 1} \frac{a_n J_n(z) \cos(n\phi)}{I_n}, \tag{2.32}$$

where $I(n) = \sum_m \frac{1}{M_{n,m}}$ and $J_n(z) = \sum_m \frac{\exp(ik_m z)}{M_{n,m}} = \sum_m \frac{\cos(k_m z)}{M_{n,m}}$ [1].

To answer the question of membrane fission by a polymorphic filament, consider first the case where the filament behaves like a WLC on large scales. Moreover, consider the case of large $l_B \gg l_e$, such that the persistence length $l_p \approx l_e$ and we can neglect the elastic fluctuations. The total free energy is the sum of the free energy of the filament (Eq. 2.18) and the one of the membrane (which is equal to its energy given by Eq. 2.31), and reads after few lines of calculations (for more details see Appendix B.4):

$$F = F_{WLC} + E_{mem} = \frac{l_e k_B T}{2} \int_0^{l_f} \tilde{\kappa}^2(s) ds + \frac{\pi B_m L}{R^3} \sum_{|n|\neq 1} \frac{|a_n|^2}{I_n} \tag{2.33}$$

$$= \frac{l_e k_B T \kappa_0^2 l_f}{4R^2} \sum_n n^4 |a_n|^2 + \frac{\pi B_m L}{R^3} \sum_{|n|\neq 1} \frac{|a_n|^2}{I_n}, \tag{2.34}$$

where l_f is the length of the filament.

Applying the equipartition theorem to each mode, we obtain:

$$< |a_n|^2 >= \frac{R^2}{2\left(\frac{l_e l_f n^4}{4R^2} + \frac{\pi B_m L}{k_B T R I_n}\right)} \quad \text{for} \quad |n| \neq 1. \tag{2.35}$$

---

[1] These sums have been calculated in the continuous limit (for $L \gg R$) and are given in Appendix B.3. In these expressions γ corresponds to a longitudinal force applied to the membrane, which is not present in this study. To correspond to this particular case, the expressions of I_n and J_n must be taken for $\gamma = 0$.

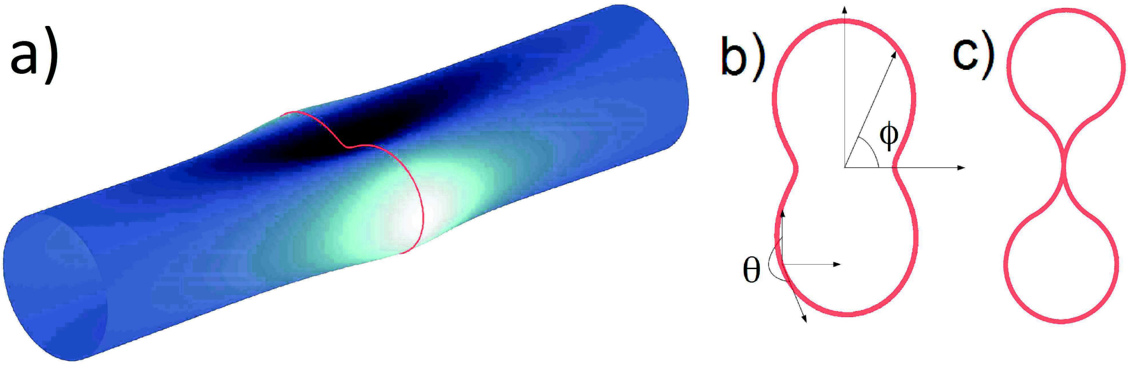

Figure 2.7: a) A crunching polymer ring on a fluid membrane, b) weakly deformed, c) critical deformation with self contact for $\kappa_1/\kappa_0 = 7/3$.

We note that the free fluctuations of the membrane are always reduced by adding the polymorphic crunching ring, even for highly soft filaments ($l_e/R \to 0$). This phenomenon is similar to a reduction of the amplitude of deformation of the polymorphic ring. Assuming that a filament can only break a tubular membrane when two opposite sides of the membrane touch each other, we find that a polymorphic ring lacking cooperativity between its subunit constituents is unable to break tubular membranes.

2.6 Cooperativity

As already mentioned earlier, many bio-filaments, such as dynamin, FtsZ, tubulin and others, display cooperative switching. In Fig. 2.7, one sees the effect of a ring with high cooperativity between the monomers. We assume that the tube breaks when two opposite sides of the membrane touch each other (see Fig. 2.7 (c)). This is the so-called hemi-fission. The condition to reach self contact has been calculated and is for $\kappa_1/\kappa_0 = 7/3$. Nonetheless, as we are in the small deformation regime, it is not possible to deform that much the filament and the tube. Thus, this self contact condition is highly speculative, but gives insight on the possible tube breakage.

The effect of cooperativity can be added to the elastic energy by assuming a cooperative inter-monomer coupling term favouring uniform curvature:

$$E_{coop} = \frac{K}{2} \int_0^L \left(\frac{d\kappa}{ds} \right)^2 ds, \tag{2.36}$$

where K is the inter-monomer coupling constant. For the kind of bio-filament we are interested in, using Euler-Lagrange method is the usual way to solve the problem. However, due to the non-linearity of the bending energy and the closure constraint, it is non-feasible to solve systematically the Euler-Lagrange equation. In the small perturbation regime, this is nonetheless possible (see Appendix B.5). We can see from this perturbative approach that the shape of the filament, depends on the mode number n as follows:

$$n = \sqrt{\frac{\sqrt{\left(6C\kappa_0^2 - B\right)^2 + 4\mu K} - \left(6C\kappa_0^2 - B\right)}{2K\kappa_0^2}}, \tag{2.37}$$

where μ corresponds to the tangential projection of the internal ring tension, and $n = 2, 3, 4, ...$ Values of n being discrete, the parameters should also be quantized. Nonetheless, in the calculations done in appendix B.5, we didn't take into account thermal fluctuations, which allow a wider range of non-discrete values for the parameters. The mode n describes the shape of the filament, where for instance, the mode $n = 2$ corresponds to the "peanut-shaped" filament shown in Fig. 2.7 (c). This shape is obtained for high values of the inter-monomer coupling constant K (as shown by Eq. 2.37). The higher K is, the less regions of different curvatures are displayed by the filament. This is intuitive, as a change in curvature costs a lot of energy for high K values. It is nonetheless important to note that in this approach, the curvature along the filament is continuous.

In the following of this cooperativity study, we assume that the filament is made of discrete units. Monomers have now curvature $\kappa = \pm\kappa_1$, except for a certain number of monomers which link these different regions. Domains switch from regions $\pm\kappa_1$ on a scale $\lambda = 2\sqrt{2}\sqrt{K/B}$ and have a transition energy penalty $J = \frac{2\sqrt{2}}{3}\sqrt{KB}\kappa_1^2$ [2]. Indeed, when K increases, with all other parameters fixed, the derivative of the curvature must be smaller, *i.e*, the length along which the curvature differs from $\pm\kappa_1$ must increase. On the other hand, when B increases, it is less costly to change curvature on a small distance, such that the length λ decreases. Similarly, the same scaling analysis can be done for the transition energy penalty J leading to the latter formula. Knowing the expressions of the λ and J, which are measurable quantities, unlike K and B, we can rewrite the energy as a function of measurable quantities as follows:

$$E_{el} = \frac{3J}{2\lambda\kappa_1^2}\left(\int_0^L \kappa^2\left(\frac{\kappa^2}{2\kappa_1^2} - 1\right)ds + \frac{\lambda^2}{8}\int_0^L \left(\frac{d\kappa}{ds}\right)^2 ds\right). \tag{2.38}$$

One can also define the effective block size, which depends exponentially on the transition energy penalty, as $\xi \sim a\exp\left(\frac{J}{k_BT}\right)$. The block size ξ of $\pm\kappa_1$ blocks can now be considered as the effective monomer size. The total length of the bio-filament now reads: $L = Na = N_b\xi = N_b a_{eff}$, where N_b corresponds to the number of $\pm\kappa_1$ curvature blocks. For short transition length, *i.e.*, for $\lambda \ll a_{eff}$, and intermediate cooperativity $(a < a_{eff} \ll L)$, all results of previous sections stay applicable, with a renormalized monomer size a_{eff}. In particular, the coarse-grained approach is still valid, and the system still behaves like a WLC on larger scales. The main difference being in the effective persistence length which is smaller than the one found previously. Indeed, the effective persistence length (Eq. 2.22) is proportional to $1/a$, such that for $a_{eff} > a$, the persistence length decreases.

For very large effective block sizes ($\xi \gg L$), the domain walls become highly costly, such that the number of regions of $\pm\kappa_1$ is minimized. In practice, this highly cooperative

---

[2] The pre-factors of these two quantities are determined in appendix B.6.

regime is reached for $J \gtrsim 5k_BT$ and cannot be described by a fluctuating WLC, but has a single well-defined ground state. It corresponds to the "peanut-shaped" filament, which displays a two-fold symmetry (see Fig. 2.3, left panel). This shape will be preferred over the simple circle if the energy of the four transition regions becomes less than the penalty for having a uniform curvature, such that:

$$4J < \frac{Bl_f\kappa_1^2}{4}\left(1 - \frac{2\kappa_0^2}{\kappa_1^2} + \frac{\kappa_0^4}{\kappa_1^4}\right). \tag{2.39}$$

A high cooperativity between monomers widens the circular filament regime. Moreover, as the effective persistence length l_e is larger, the filament is stiffer. It makes the filament able to crunch membrane tubes. It is important to notice that this is the only situation where a filament could possibly break a tube. The calculation is only valid in the linear regime, but would at least qualitatively hold in the non-linear regime.

2.7 Conclusion

We have shown in this chapter that the conceptually simple procedure of closure transforms a simple an-harmonic bio-filament with a unique ground state in a complex multi-stable filament. Moreover, this unexpected filament displays an exponentially large number of ground states, depending on its total length. We have shown that in the limit of low cooperativity, the filament can explore, thanks to thermal fluctuations, this multi-stable energy landscape, thus exhibiting anomalous fluctuations. Moreover, it can be modelled as a Worm-Like Chain but with an effective persistence length, which varies in accord with the length of the filament. This effective persistence length is dominated by the configurational fluctuations between the many ground states.

Motivated by FtsZ and dynamin bio-filaments we have started to explore the interaction of such a multi-stable crunching filament with a tubular fluid membrane. We have seen that a crunching ring can deform a membrane tube only in the presence of strong inter-monomer cooperativity. In this cooperative limit the membrane could undergo fission in a novel geometric scenario: the membrane is forced through itself and possibly ruptured by the crunching filament slicing through it.

Chapter 3

How bio-filaments twist membranes

As mentioned in the previous chapters, the interactions between bio-filaments and bio-membranes is of high importance in the biological world. More specifically, we have seen in the last chapter that filaments can display a more complex shape than the one of a standard semi-flexible chain. Moreover, in addition to the shape of the filament, its interaction with the membrane can as well be more complex than the action of a simple normal force. In this chapter we will focus in particular on the case when a filament applies local torques. This can, for instance, happen when the filament is ribbon-like and preferentially interacts with one of its faces (*e.g.* via an amphiphilic region which intercalates into the membrane), while preferentially curving in an incompatible direction. The frustrated filament then exerts a so-called *Darboux torque* on the membrane as we will explain in more detail in Sec. 3.1. Other examples of frustration are a twisted filament, the *"twister"*, that preferentially adsorbs in an untwisted state and a curved filament, the *"bender"*, that preferentially adsorbs in a unbent state. We will explore how such filaments deform typical membrane structures in the linear regime. In our formulation the membrane surface adapts to the filament unlike in [109, 110, 111, 112].

Apart from flat membranes (see Sec. 3.2), one often finds tubular geometries in the biological cell. For instance, dynamin filaments wrap around the membranes of eukaryotic cells during endocytosis [62, 63, 114] forming a helix whose pitch is small. FtsZ filament rings constrict the membranes of tubular bacteria during cell division [66, 67]. It is therefore interesting to study how such bio-filaments interact with a tubular membrane in a general setting (see Sec. 3.3). In this context we will address the question of how several of such bio-filaments interact with each other via the deformations they impose on the membrane on which they adhere. This is a particular realisation of the important theme of surface-mediated interactions between membrane inclusions, intensely studied since the seminal paper by Goulian *et al.* in the 1990s [115].

3.1 Elementary realisations of torque-applying filaments

Filaments can deform membranes not only by applying normal forces but also by the action of torques. One way how a filament can generate torques locally results from a mismatch

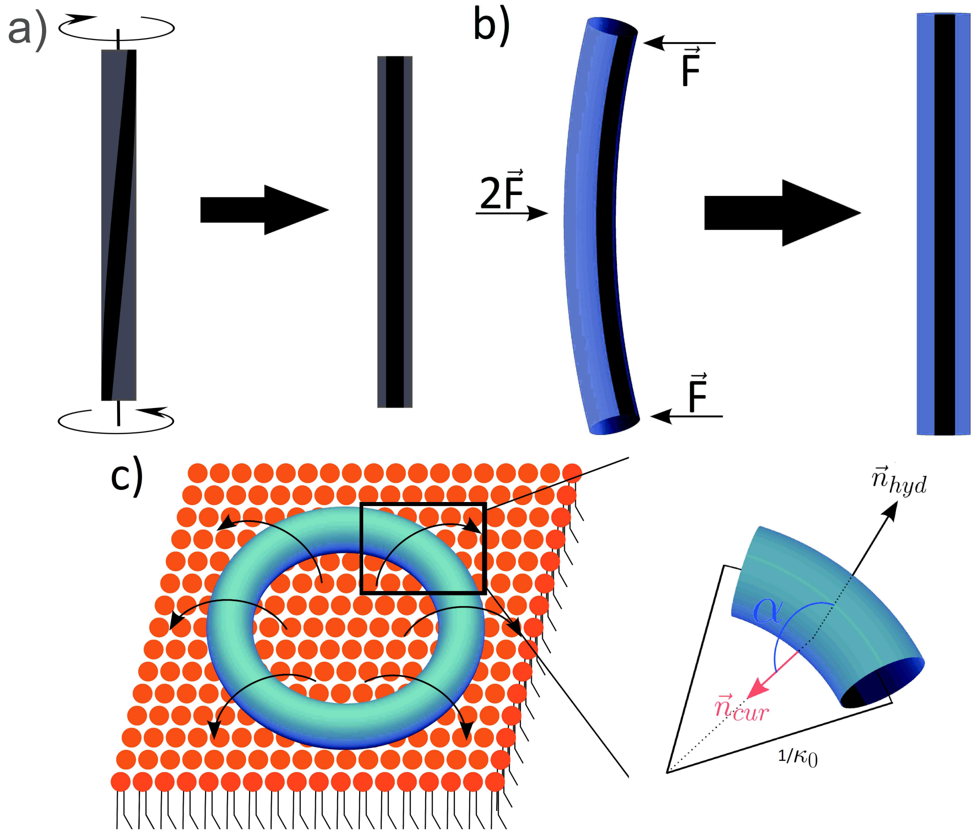

Figure 3.1: Schematic representation of (a) a straight and (b) a curved filament with their hydrophobic parts in black, prestressed to bind to flat membranes, (c) a closed circular filament applying local torques on a membrane (*left*), consisting of monomers of curvature κ_0 with their hydrophobic parts in black (*right*).

between its anchoring hydrophobic face and either (i) internal twist or (ii) spontaneous curvature.

As an example of case (i) consider a straight unbound amphiphilic filament and assume that its subunits are connected in such a way that their hydrophobic faces do not form a line but rather lie on a helical curve (see Fig. 3.1 (a)). To perfectly bind to a flat membrane the filament would need to be twisted such that the hydrophobic faces are aligned. After binding, the filament would then try to untwist inducing a torque density on the membrane which adds up to zero. An elementary realisation of such a system, that we call the *twister*, consists of a torque doublet, *i.e.*, two anti-parallel point torques applied along the filament, in the limit of vanishing distance between the two torques.

For case (ii) we assume that the subunit of an unbound amphiphilic filament is curved intrinsically with curvature κ_0 in a plane defined by the normal vector $\vec{n}_{\text{cur}}$ (see Fig. 3.1 (c)). By applying a prestress to the filament it can be forced to bind to the membrane. Its hydrophobic part penetrates and orients itself normal to the membrane. In other words the hydrophobic vector $\vec{n}_{\text{hyd}}$ aligns with the normal vector of the membrane. However, to release the prestress, the filament rotates around its tangent, thus inducing a spinning of its internal frame. As the filament binds to the membrane, the Darboux frame associated to the membrane spins too [116]. We call this torque applied by the filament the *Darboux torque*. It corresponds to two opposite forces placed at two close points on the surface.[1] Nonetheless, the whole system must be at mechanical equilibrium, such that all forces and torques applied add up to zero. Considering the latter point, it is then clear that the circular filament of Fig. 3.1 (c) is in equilibrium as soon as it has rotated and deformed the membrane, whereas randomly distributed force- or torque-exerting proteins will in general lead to a non-equilibrated system. The *bender* introduced in the introduction of this chapter is a particular realisation of prestressed curved filaments. It corresponds to a torque doublet, similarly to the twister. Nonetheless, the two torques are applied perpendicularly to the filament (see Fig. 3.1 (b)).

There are several cases where no prestress is needed to align the hydrophobic parts of the closed circular filament with the normal vector of a flat or tubular membrane. When the two normals $\vec{n}_{\mathrm{cur}}$ and $\vec{n}_{\mathrm{hyd}}$ are orthogonal, *i.e.*, when $\alpha = 90°$, the filament can bind to a *flat* membrane without applying local torques. Filaments, for which α is equal to $0°$ or $180°$, respectively, preferentially bind to the *inner* part of a tubular membrane in the former case, while binding to the *outer* part of the tubular membrane in the latter. For all intermediate values of α, one needs to prestress the circular filament to bind it to a flat or a tubular membrane, thereby inducing Darboux torques.

We represent the filament by the system of local torques it exerts without discussing the structure of the filament explicitly. In the limit of small deformations, which is assumed, the torques are usually constants (independent of the deformation). The latter assumption can be finally relaxed if the torque-filament structure relation is known (see discussion below Eq. (3.19)).

3.2 Twister, bender and Darboux torques on flat membranes

The elastic energy of a deformed fluid membrane, which is flat in its reference state, is given by [15, 16, 17]

$$E_{mem} = \int dA \left(2B_m H^2 + \sigma\right), \tag{3.1}$$

where dA is the surface area, B_m the bending rigidity, H the mean curvature and σ the surface tension. In the small deformation regime, the displacement field u is normal to the reference plane and the elastic energy E_{mem} up to second order in u and its derivatives reads

$$E_{mem} = \frac{B_m}{2} \int \left(\left(\boldsymbol{\nabla}^2 u\right)^2 + \frac{1}{\lambda^2}\left(\boldsymbol{\nabla} u\right)^2\right) dS, \tag{3.2}$$

---

[1] Note that the hydrophobic part of the monomer and the backbone of the filament are not necessarily aligned. This implies that the filament can apply local torques that are not parallel to its backbone.

where $\lambda = \sqrt{B_m/\sigma}$, $\mathbf{\nabla}$ and dS are the two-dimensional nabla operator and area element of the flat reference plane, respectively.

In Cartesian coordinates, the displacement field can be expanded in modes in the reference plane (x, y) as:

$$\begin{aligned} u(x,y) &= \sum_{n,m=-\infty}^{\infty} C_{n,m} \exp\left(i(k_m x + k_n y)\right) \\ &\xrightarrow{L \gg \lambda} \frac{L^2}{4\pi^2} \int_{-\infty}^{\infty} dk \int_{-\infty}^{\infty} dk' C(k,k') \exp\left(i(kx + k'y)\right), \end{aligned} \tag{3.3}$$

where $k_m = \frac{2\pi}{L} m$, $k_n = \frac{2\pi}{L} n$, and L is the length of the membrane in the x and y-directions.

The energy of the deformed flat membrane can be rewritten in the following manner

$$E_{mem} = B_m \sum_{n,m=-\infty}^{\infty} M_{n,m} |C_{n,m}|^2, \tag{3.4}$$

where $M_{n,m} = \frac{L^2}{2}\left((k_m^2 + k_n^2)^2 + \frac{1}{\lambda^2}(k_m^2 + k_n^2)\right)$ is the (unscaled) elastic response function which has units of length^{-2}.

In this chapter we focus on the fixed forces and torques ensemble [2], where the filaments can freely polymerise or depolymerise unlike the crunching ring on a tubular membrane studied in the previous chapter. This implies that their length is not fixed. For the system to be in mechanical equilibrium, the sums of all forces and torques must be zero. As we focus on filaments that only apply torques, the sum of forces is zero trivially. The energy of the system is given by $E_{tot} = E_{mem} + \sum_{j=1}^{N} E_{M_{ext}}^{(j)}$, where N is the number of filaments on the membrane. The potential energy due to the torques $M_{ext}^{(j)}$ along each filament j on a flat membrane is given by

$$E_{M_{ext}}^{(j)} = -\int_{-\infty}^{\infty} dx \int_{-\infty}^{\infty} dy \left(M_x^{(j)}(x,y) \frac{du(x,y)}{dy} - M_y^{(j)}(x,y) \frac{du(x,y)}{dx} \right), \tag{3.5}$$

where $M_x^{(j)}$ and $M_y^{(j)}$ are the torque densities applied in the x- and y-direction, respectively (see appendix C.1). Note that torques cannot be applied in the direction of the normal of a membrane due to its fluidity. Thus, for a flat membrane one only considers torques in the reference plane. A similar study for general inclusions (applying a random distribution of forces) has been performed by Sens and co-workers [117].

To reach mechanical equilibrium, it is necessary to have at least two anti-parallel point torques. We call this doublet of torques a *twister*, when they are applied along the filament and the distance between both is sent to zero (see case (i) in Sec. 3.1). Similarly, a doublet

---

[2] Two types of "boundary condition" can be chosen corresponding to two different ensembles. On the one hand, it is possible to consider the filaments as boundary conditions fixed in space, which implies that the number of monomers of each filament is fixed (*fixed length ensemble*). On the other hand, they can be treated as objects which induce external forces and torques locally (*fixed forces and torques ensemble*).

of torques applied perpendicularly to the filament is called a *bender*, when the distance between both is sent to zero (see special realisation of case (*ii*) in Sec. 3.1). For the sake of generality we will first give the expression of the displacement field and the energy for many point torques and then describe the twister and bender themselves.[3]

The energy contribution of the j-th point torque can be found by inserting the displacement field, Eq. (3.3), into Eq. (3.5) with $M_{x/y}^{(j)}(x,y) = M_{x/y}^{(j)}\delta(x-x_j)\delta(y-y_j)$:

$$E_{M_{ext}}^{(j)} = -i \sum_{n,m=-\infty}^{\infty} C_{n,m} \left(k_n M_x^{(j)} - k_m M_y^{(j)}\right) \exp\left(i(k_m x_j + k_n y_j)\right). \tag{3.6}$$

By minimizing the total energy $E_{tot} = E_{mem} + \sum_{j=1}^{N} E_{M_{ext}}^{(j)}$ with respect to the $C_{n,m}$, the shape equations read

$$C_{n,m} = \sum_{j=1}^{N} \frac{-i\left(k_n M_x^{(j)} - k_m M_y^{(j)}\right) \exp\left(-i(k_m x_j + k_n y_j)\right)}{2B_m M_{n,m}}. \tag{3.7}$$

Inserting this result into Eqs.(3.4) and (3.6) one finds that the two terms of the total energy of the system are related by $\sum_{j=1}^{N} E_{M_{ext}}^{(j)} = -2E_{mem}$. This result holds in general for any distribution of torques. The energy is thus always negative and reads in the case of N point torques:

$$\begin{aligned} E_{tot} = &- \sum_{n,m=-\infty}^{\infty} \sum_{j=1}^{N} \frac{(k_n M_x^{(j)} - k_m M_y^{(j)})^2}{4B_m M_{n,m}} \\ &- \sum_{n,m=-\infty}^{\infty} \sum_{j<j'} \frac{(k_n M_x^{(j)} - k_m M_y^{(j)})(k_n M_x^{(j')} - k_m M_y^{(j')}) \cos(k_m(x_j - x_{j'}) + k_n(y_j - y_{j'}))}{2B_m M_{n,m}}. \end{aligned} \tag{3.8}$$

With the help of the shape equations, we finally get the displacement field of the membrane as a function of the applied torques. For one point torque at the origin it reads

$$u^{(j)}(x,y) = \frac{(M_x^{(j)} y - M_y^{(j)} x)\lambda^2}{4\pi B_m} \left(\frac{1}{x^2+y^2} - \frac{\mathcal{K}_1(\sqrt{(x^2+y^2)/\lambda^2})}{\lambda\sqrt{x^2+y^2}} \right), \tag{3.9}$$

where $\mathcal{K}_n(x)$ is the n-th modified Bessel function of the second kind [118], and where the summations over the modes are calculated. In general, the total displacement field for N point torques located at $x = x_j$, $y = y_j$ reads: $u(x,y) = \sum_{j=1}^{N} u^{(j)}(x - x_j, y - y_j)$.

In particular, we focus on the twister, which corresponds to two point torques localised at $x = x_1$, $y = y_1$ and $x = -x_1$, $y = y_1$. Without loss of generality, let us assume that the torque is only applied along the filament, oriented along the x-axis. The displacement field for this doublet reads : $u(x,y) = u_{M_x}(x - d/2, y) + u_{-M_x}(x + d/2, y)$, where we impose M_x at $x = d/2$ and $-M_x$ at $x = -d/2$. For $d \to 0$ the doublet becomes a twister which

---

[3] Note that mechanical equilibrium is not necessarily reached in the general case.

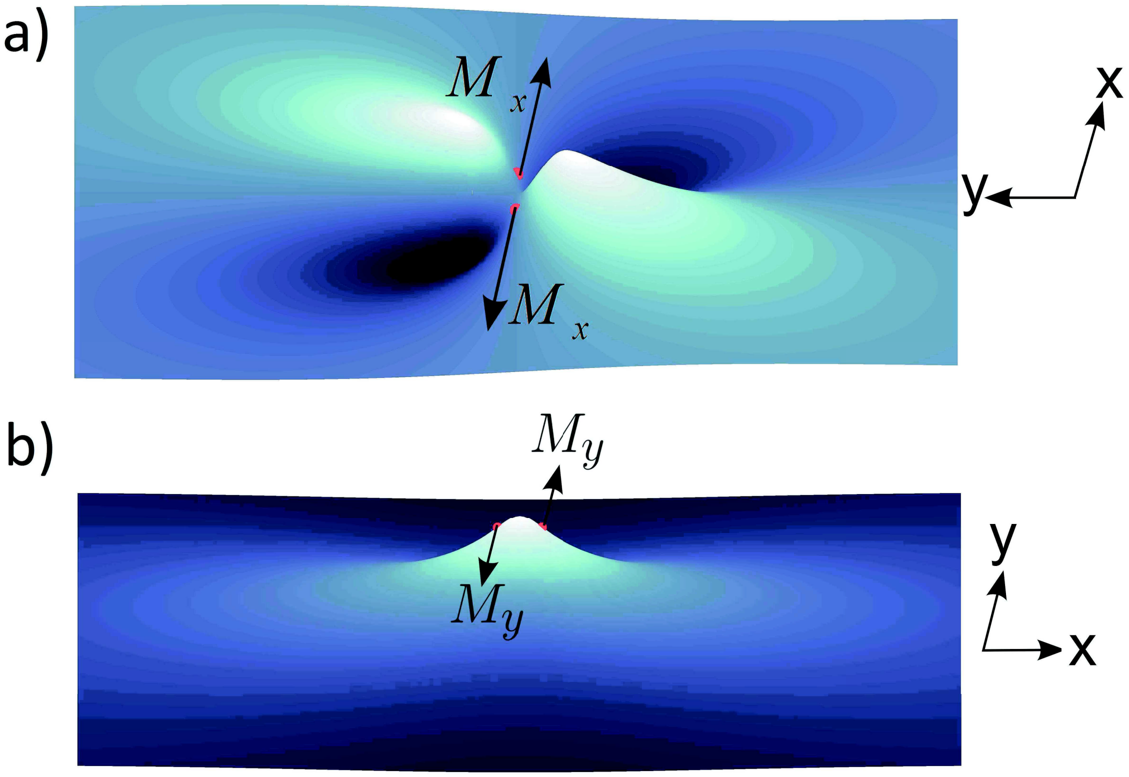

Figure 3.2: Deformations of a flat membrane due to (a) a twister and (b) a bender (torque doublets) applying Darboux torques.

deforms the membrane as shown in Fig. 3.2 (a). For $\rho = \sqrt{x^2 + y^2} \ll \lambda$, $d \ll \lambda$ and $\rho \gg d$, the displacement field in cylindrical coordinates reads

$$u(\rho, \phi) = \frac{M_x \sin(2\phi) d}{16\pi B_m} \tag{3.10}$$

to lowest order in d/ρ. A single point torque reshapes the membrane in an antisymmetric manner, with the axis of symmetry given by the direction of the torque. As the two torques of the twister are opposite to each other, they induce an additional two-fold symmetry encoded in the sine function. For $\rho \gg \lambda$ and $d \ll \rho$ (far field), the displacement field reads

$$u(\rho, \phi) = \frac{M_x \sin(2\phi)}{4\pi\sigma} \frac{d}{\rho^2} \tag{3.11}$$

to lowest order in d/ρ. The two-fold symmetry is still present even at infinity. Interestingly, the displacement field does not decrease exponentially, but as a power law $u(\rho, \phi) \propto \rho^{-2}$. The deformation is thus not short-range, but rather long-range, as was found in similar cases as well, such as in Ref. [119] for interacting inclusions. In this regime it is the surface tension which controls the shape, whereas bending dominates for distances $\rho \ll \lambda$.

Similarly, let us study the bender. Without loss of generality, assume that the two point torques are localised at $x_1 = d/2$, $y_1 = 0$ and $x_2 = -d/2$, $y_2 = 0$, such that the

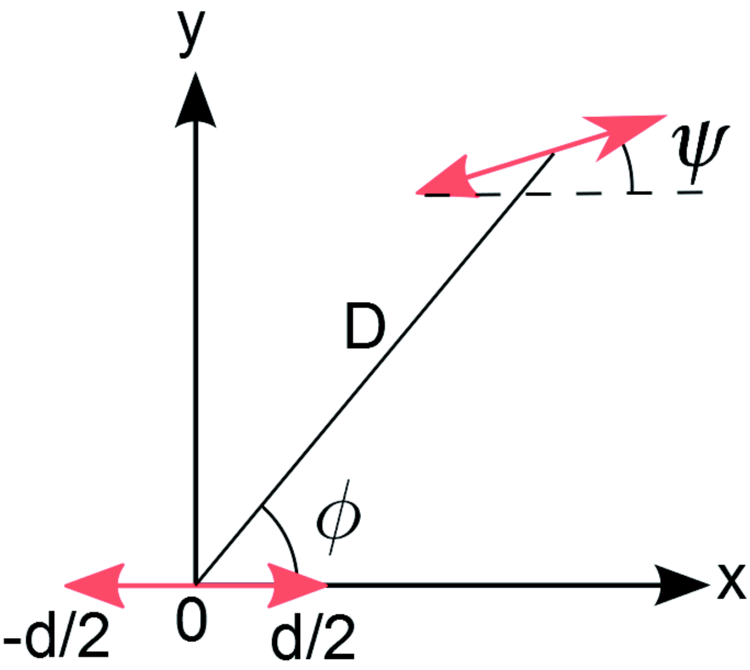

Figure 3.3: Scheme of two twisters (in red) of size d separated by a distance $D \gg d$. The angle ϕ corresponds to the azimuthal angle, whereas ψ holds for the orientation of the second twister with respect to the first one (the one at the origin of the frame).

bender is oriented along the x-axis. The displacement field for this torque doublet reads: $u(x, y) = u_{M_y}(x - d/2, y) + u_{-M_y}(x + d/2, y)$, where we impose M_y at $x_1 = d/2$ and $-M_y$ at $x_2 = -d/2$. For $d \ll \rho \ll \lambda$, the displacement field can be approximated by

$$u(\rho, \phi) = \frac{M_y d}{8\pi B_m} \left(\cos^2(\phi) - \ln(\rho/\lambda)\right). \tag{3.12}$$

Interestingly, the two-fold symmetry still exists for the bender, and is hidden only in the $\cos^2(\phi)$. The logarithmic term, which corresponds to the decay of the out-of-plane displacement field, does not display any angular dependence. For $\rho \gg \lambda$ and $d \ll \rho$, the displacement field reads

$$u(\rho, \phi) = -\frac{M_y \cos(2\phi)}{4\pi\sigma} \frac{d}{\rho^2} \tag{3.13}$$

to lowest order in d/ρ. This result is similar to the one of the twister, with the axis of symmetry still given by the direction of the torques. It is interesting to note that all deformations due to straight filaments can be approximate by a twister and a bender.

Let us now focus on two identical twisters on a flat membrane[4]. For simplicity, we will only consider the limiting case of large distances between twisters and we will assume one twister is located at the origin of the frame (see Fig. 3.3). For a twister at the origin the deformation is given by $u^T(x, y) = u^{(1)}(x - d/2, y) + u^{(2)}(x + d/2, y)$. Its interaction energy

---

[4] We will not consider the case of two benders as the results are the same.

with a second twister is equal to

$$
\begin{aligned}
E_{int} = & -\int dx\delta(x-x_1)\int dy\delta(y-y_1)\left(M\cos(\psi)\frac{du^T(x,y)}{dy} - M\sin(\psi)\frac{du^T(x,y)}{dx}\right) \\
& + \int dx\delta(x-x_2)\int dy\delta(y-y_2)\left(M\cos(\psi)\frac{du^T(x,y)}{dy} - M\sin(\psi)\frac{du^T(x,y)}{dx}\right),
\end{aligned}
\tag{3.14}
$$

where x_1 and y_1 are the coordinates of the positive point torque of the second twister, and x_2 and y_2 are the coordinates of the negative point torque of the second twister and all torques have an absolute value of M.

In the limit of $\rho \gg d$ the displacement field of a single twister is given by Eq. 3.11, *i.e.*, $u(\rho,\phi) = \frac{M}{4\pi\sigma}\frac{d}{\rho^2}\sin(2\phi)$. In Cartesian coordinates:

$$
u^T(x,y) = \frac{M}{2\pi\sigma}\frac{d\ x\ y}{(x^2+y^2)^2}.
$$

As $\dfrac{du^T(x,y)}{dy} = \dfrac{Md}{2\pi\sigma}\dfrac{x(x^2-3y^2)}{(x^2+y^2)^3}$ and $\dfrac{du^T(x,y)}{dx} = \dfrac{Md}{2\pi\sigma}\dfrac{y(y^2-3x^2)}{(x^2+y^2)^3}$, and with:

$$
\begin{aligned}
x_1 &= D\cos(\phi) + d/2\cos(\psi) \qquad & x_2 &= D\cos(\phi) - d/2\cos(\psi) \\
y_1 &= D\sin(\phi) + d/2\sin(\psi) \qquad & y_2 &= D\sin(\phi) - d/2\sin(\psi),
\end{aligned}
$$

one gets at first order with $D \gg \lambda$ and $D \gg d$:

$$
E_{int} \approx \frac{3M^2}{2\pi\sigma}\frac{d^2}{D^4}\cos(4\phi - 2\psi)\ ,
$$

where ψ is the angle between the orientation of the first and the second twister (see Fig. 3.4). D is the distance between the two middles of the twisters[5]. The interaction energy decays thus with D^{-4} and depends on the respective orientations of the two twisters. For the case where $\lambda \gg \rho \gg d$, the expression of the out-of-plane displacement field as it is given in the text is not sufficient to get a correct answer. One has to consider higher order terms and finally gets a similar expression for the interaction energy of two twisters:

$$
E_{int} \approx \frac{M^2}{8\pi B_m}\frac{d^2}{D^2}\cos(4\phi - 2\psi). \tag{3.15}
$$

The only difference resides in the fact that the energy decays with D^{-2}. Interestingly, two identical twisters do not attract each other to form long chains, they repulse each other. The creation of long filaments thus is not possible if all the twisters present on the membrane are identical [6]. Nonetheless, if proteins (assimilated to twister) have two preferred states, one where the hydrophobic part lies on a left-handed helix and the other one

---

[5] It follows that D is different from ρ: $\rho = \sqrt{x_1^2 + y_1^2}$ or $\rho = \sqrt{x_2^2 + y_2^2}$.

[6] Twisters attract each other depending on their relative orientations, but will not lead to the creation of filaments. They would more create clusters of twisters

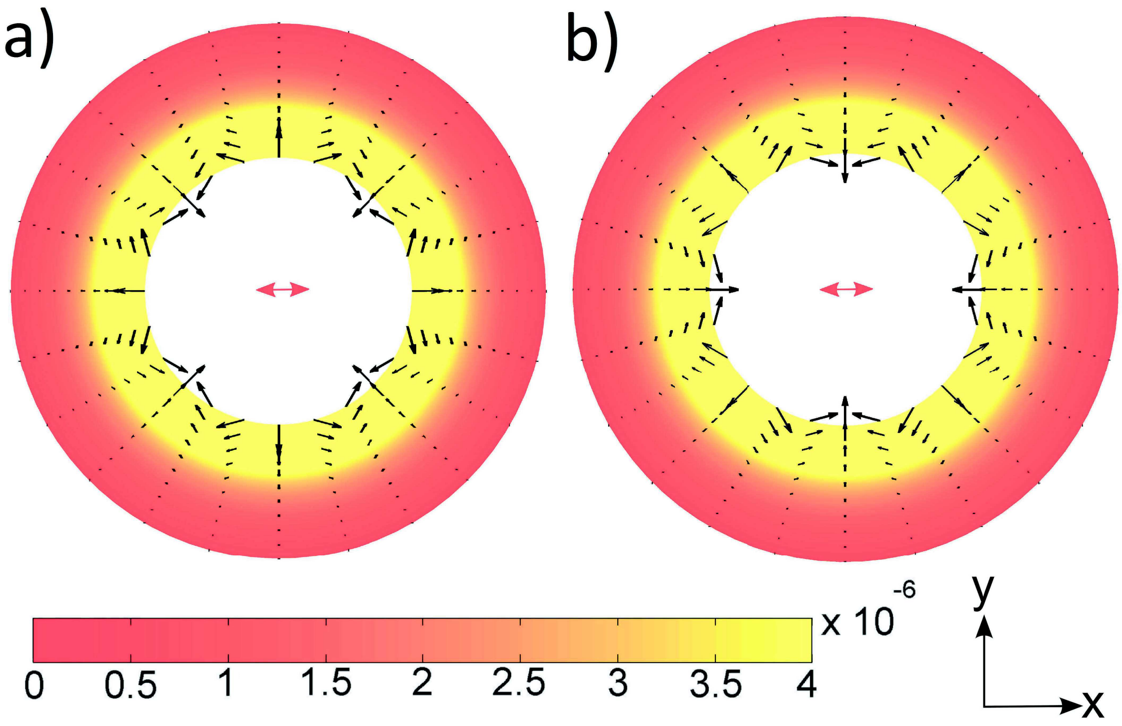

Figure 3.4: Forces landscapes between two twisters, where the central one, oriented along the x-axis is represented in red, for $d/\lambda = 0.1$, $M/B_m = 1$ and $4 < D/\lambda < 8$. The vector fields represent the orientation of these forces, while the colormap describes the intensity of these forces. The second twister is (a) parallel ($\psi = 0$) and (b) perpendicular ($\psi = \pi/2$) to the central twister.

where the hydrophobic part lies on a right-handed helix, the formation of long filaments is conceivable. The filament will correspond to the alternation of left and right-handed twisted proteins.

Another elementary realisation of a torque-applying filament consists of the circular ring as introduced in Sec. 3.1 (see Fig. 3.1 (b)). To determine the deformations of a flat membrane due to the applied Darboux torques we choose polar coordinates. The displacement field is then given by a Fourier-Bessel series [118]

$$u(\rho, \phi) = \sum_{m=1}^{\infty} \frac{C_{0,m}}{\sqrt{2\pi}} \mathcal{J}_0(k_m \rho), \tag{3.16}$$

where ρ_0 corresponds to the radius of curvature in the surface plane of the circular ring and $\mathcal{J}_0(x)$ is the zeroth Bessel function of the first kind. The k_m follow from the boundary conditions at $\rho = L$ [120].

Using the same method as previously, and summing over all the modes, we can rewrite

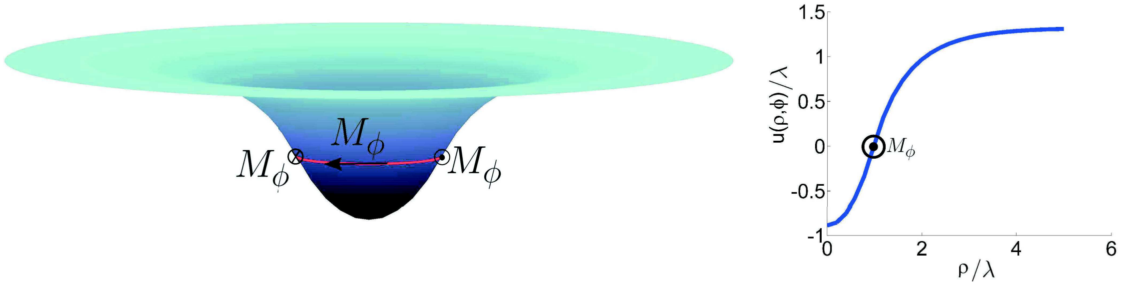

Figure 3.5: Deformations of a flat membrane due to a closed circular filament applying Darboux torques.

the displacement field $u(\rho, \phi)$ and the energy of the system as follows

$$u(\rho,\phi) = \frac{-\rho_0 (M_\phi \lambda) \mathcal{K}_1(\rho_0/\lambda)}{B_m} \left(\mathcal{I}_0\left(\frac{\rho}{\lambda}\right) - \mathcal{I}_0\left(\frac{\rho_0}{\lambda}\right) \right) \quad \text{for} \quad \rho < \rho_0 \tag{3.17}$$

$$u(\rho,\phi) = \frac{\rho_0 (M_\phi \lambda) \mathcal{I}_1(\rho_0/\lambda)}{B_m} \left(\mathcal{K}_0\left(\frac{\rho}{\lambda}\right) - \mathcal{K}_0\left(\frac{\rho_0}{\lambda}\right) \right) \quad \text{for} \quad \rho > \rho_0, \tag{3.18}$$

and

$$E_{tot} = -\frac{\pi (M_\phi \lambda)^2 \rho_0^2}{B_m \lambda^2} \mathcal{K}_1(\rho_0/\lambda) \mathcal{I}_1(\rho_0/\lambda) \ , \tag{3.19}$$

where M_ϕ is the torque per unit length applied by the filament (see appendix C.1) and $\mathcal{I}_n(x)$ is the n-th modified Bessel function of the first kind. A more direct method to obtain the same results using Euler-Lagrange formalism is described in appendix C.3.

Due to the Darboux torques the circular filament creates an invagination in the membrane, a precursor of vesicle formation (see Fig. 3.5). The depth of the invagination is given by

$$\mathcal{D} = |u(\rho \to \infty) - u(\rho = 0)| = \left| \frac{(M_\phi \lambda) \lambda}{B_m} \left(\frac{\rho_0 \mathcal{K}_1(\rho_0/\lambda)}{\lambda} - 1 \right) \right| . \tag{3.20}$$

Let us again take a look at the limiting cases, *i.e*, when ρ_0/λ is either small or large. When the size of the ring is small compared to the characteristic length λ the depth reads $\mathcal{D} = \left| \frac{(M_\phi \lambda)}{2B_m} \ln(\rho_0/\lambda) \frac{\rho_0^2}{\lambda} \right|$. For $\rho_0 \to \infty$, the depth is equal to $\mathcal{D} = |\frac{M_\phi}{\sigma}|$. Increasing the size of the filament increases the depth, until it reaches its maximal value, the actual value of the applied torque per unit length divided by the surface tension.

It is possible to find a relation between M_ϕ and ρ_0 by assuming that the intrinsically curved filament behaves like a Worm-Like Chain. From [121] one can show that $(M_\phi \lambda)\, \rho_0 = 2\pi B_f \cos(\alpha)$ on a flat membrane, where B_f is the bending stiffness of the filament. This result is consistent with the results of Sec. 3.1: when the two normals $\vec{n}_{\mathrm{cur}}$ and $\vec{n}_{\mathrm{hyd}}$ are orthogonal, $\alpha = 90°$, and the Darboux torque vanishes at equilibrium.

The formalism described in this chapter is valid when the variation of the angle α is small. In this case and for $\rho_0/\lambda \ll 1$, we obtain $B_f/B_m \ll \lambda$. Since the persistence length of the filament l_p is defined such that $B_f = l_p k_B T$, and for a membrane bending stiffness $B_m \approx 10 k_B T$, we finally get $l_p \lesssim 10\lambda$. Depending on the surface tension σ, $50nm < \lambda < 5\mu m$, such that the persistence length $l_p \lesssim 50\mu m$ at best. Similarly, for $\rho_0 \gg \lambda$, one finds that $l_p \lesssim 10\rho_0$. For ρ_0 of the order of $1\mu m$, intermediate filaments ($\approx 1\mu m$) thus can fit into our theory. This model is also applicable for actin filaments ($\approx 17\mu m$) for a surface tension close to the one of rupture of membranes.

3.3 Closed bio-filament rings on tubular membranes

Membranes in biological systems are not necessarily flat. To analyse exemplarily how torque-applying filaments interact with curved geometries, we focus on tubular membranes from now on. The elastic energy of such a membrane is given by

$$E_{mem} = \int \mathrm{d}A \left(2B_m H^2 + \sigma\right) - P \int \mathrm{d}V - FL \,, \tag{3.21}$$

where the surface integral corresponds to the energy of the flat case, Eq. (3.1). Additionally, one has to account for a pressure difference P between the inside and outside of the tube ($P = P_{in} - P_{out}$ with dV the infinitesimal volume element) and an external longitudinal force F which controls the length L of the membrane. Before including the filament(s) in our calculations, we will recapitulate Ref. [103], in which the stability of tubular membranes was studied in detail.

In the case of a cylinder, the mean curvature is equal to $H = -\frac{1}{2R}$ where R is the radius of the cylinder. To obtain the radius of the tube at equilibrium, we set the first variation of the energy with respect to L and R to zero. This yields two relations between the five variables R, P, F, B_m, and σ:

$$F = 2\pi R\sigma - \pi R^2 P + \frac{B_m \pi}{R}, \tag{3.22}$$

$$\sigma = RP + \frac{B_m}{2R^3}. \tag{3.23}$$

When the membrane is constrained by one or more bio-filaments it will react to the imposed constraints and will reshape. The radius r of the membrane will not be constant any more, but will depend on the local position such that $r(\phi, z) = R + u(\phi, z)$, where $u(\phi, z)$ is the radial displacement field, z the longitudinal axis coordinate and ϕ the azimuthal angle. The energy up to second order in u and its derivatives is given by [103]:

$$E_{mem} = \int_{-L/2}^{L/2} \int_0^{2\pi} e_{mem}(\phi, z) \mathrm{d}\phi \mathrm{d}z, \tag{3.24}$$

with

$$\begin{aligned} e_{mem}(\phi, z) =& B_m[(\partial_\phi^2 u)^2 + 3u^2 + 2r^2(\partial_z^2 u)(\partial_\phi^2 u) - 2r^2(\partial_z u)^2 \\ &+ r^4(\partial_z^2 u)^2 + 4u(\partial_\phi^2 u)]/(2R^3) \\ &+ F[u^2 - (\partial_\phi u)^2 - r^2(\partial_z u)^2]/(2\pi R^2). \end{aligned} \tag{3.25}$$

The radial deformation of the membrane can be decomposed into Fourier modes analogous to the flat membrane case (see Eq. (3.3)):

$$u(\phi, z) = \sum_{m,n=-\infty}^{\infty} C_{n,m} \exp\left(i(n\phi + k_m z)\right), \tag{3.26}$$

where $k_m = \frac{2\pi}{L} m$ is the wave vector. The energy then reads

$$E_{mem} = E_0 \sum_{m,n=-\infty}^{\infty} M_{n,m} \left|C_{n,m}\right|^2 \ , \tag{3.27}$$

where the (scaled) elastic response function is given by

$$M_{n,m} = \left(R^2 k_m^2 + n^2 - 1\right)^2 - 2(n^2-1) + \gamma(R^2 k_m^2 + n^2 - 1), \tag{3.28}$$

with $E_0 = \pi B_m L / R^3$ and $\gamma = FR/\pi B_m$.[7]

For the modes $n = \pm 1$ and $k_m = 0$, the energy cost to deform the membrane is zero. Since these modes correspond to trivial translational modes, we are allowed to neglect them in the following. As mentioned in [103], mean-square amplitudes of thermal fluctuations are easily obtained using the equipartition theorem:

$$< |u|^2 >= u_0^2 \sum_{n,m=-\infty}^{\infty} \frac{1}{M_{n,m}}, \quad \text{where} \quad u_0 = \sqrt{\frac{k_B T R}{2 B_m \pi L}}. \tag{3.29}$$

All modes $n \geq 2$ are stable, while the modes $n = 0, 1$ are not always stable, depending on the parameter γ. The first critical modes, which can potentially lead to instabilities, are the modes $n = 1$, $m = 1$ and $n = 0$, $m = 0$. However, it turns out [103] that the tube is stable for *all* modes within the range [8]

$$-\left(\frac{2\pi R}{L}\right)^2 < \gamma < 3. \tag{3.30}$$

This implies that even a vanishing force F, *i.e.*, $\gamma = 0$, can lead to a stable tube as long as the tube is finite. Rewriting Eqs. (3.22) and (3.23), we get the pressure and the surface tension as a function of γ, B_m and R:

$$P = \frac{(\gamma - 2) B_m}{R^3} \tag{3.31}$$

$$\sigma = \frac{(2\gamma - 3) B_m}{2R^2}. \tag{3.32}$$

---

[7] In the large L limit, the sum over m can be replaced by an integral and Eqs. (3.26) and (3.27) read

$$u(\phi, z) = \sum_{n=-\infty}^{\infty} \int_{-\infty}^{\infty} \frac{L dk}{2\pi} C_n(k) \exp\left(i(n\phi + kz)\right) \quad \text{and} \quad E_{mem} = L \sum_{n=-\infty}^{\infty} \int_{-\infty}^{\infty} \frac{dk}{2\pi} M_n(k) \left|C_n(k)\right|^2 \ ,$$

where $M_n(k)$ can be obtained from $M_{n,m}$ by replacing k_m with k.

[8] Note that this study is only valid for tubes without ends. In real biological systems, as for instance during endocytosis, the tube is linked at both ends. These ends play a role on the stability of the tubular membranes. Due to these boundaries at both ends, the forces needed to stabilise tubular membranes would take different values. In particular, negative forces might not be valid for tube stabilisation any more.

The radius of the tube follows as $R = \sqrt{\frac{2\gamma-3}{2}\frac{B_m}{\sigma}}$. Since the radius is always positive, the surface tension, but also the pressure difference are found to be negative for certain values of γ. In particular, without an external longitudinal force, both σ and P are negative. To impose a positive P and σ, the longitudinal force has to be in the range $\frac{2\pi B_m}{R} < F < \frac{3\pi B_m}{R}$.

In the following, we will specialise the formalism to important cases and analyse how the tubular membrane reshapes under given torque distributions in the fixed forces and torques ensemble. To reach mechanical equilibrium, a single monomer or protein cannot apply an external torque without being coupled to something else such as other proteins or the cytoskeleton [9]. In a first step we will implicitly assume that such a coupling exists in order to analyse the linear response of the membrane to the application of point torques [10].

In the case of several proteins which exert a local point torque on a tubular membrane, the energy of protein j is given by an expression similar to Eq. (3.5) (see appendix C.1), with $M^{(j)}_{z/\phi}(\phi, z) = M^{(j)}_{z/\phi}\delta(\phi - \phi_j)\delta(z - z_j)$ (see appendix C.4). The total energy and the displacement field for one protein read:

$$E_{tot} = -\sum_{n,m=-\infty}^{\infty} \frac{(k_m R M_\phi - n M_z)^2}{4\pi B_m M_{n,m} L/R} \tag{3.33}$$

and

$$u(\phi, z) = \sum_{n,m=-\infty}^{\infty} \frac{(k_m R M_\phi - n M_z)\, R}{2\pi B_m M_{n,m} L/R} \sin\left(k_m(z - z_1) + n(\phi - \phi_1)\right), \tag{3.34}$$

where the protein is located at $z = z_1$ and $\phi = \phi_1$.

Interestingly, the main deformations of the tubular membrane are due to Goldstone modes [122], *i.e.*, the modes $n = \pm 1$ with $k_m \neq 0$. These modes of deformation are soft modes, such that the energy cost vanishes for $L \to \infty$. To a first approximation each cross-section of constant z does not change its circular shape and is only shifted perpendicular to the longitudinal axis (see Fig. 3.6 (a)).

By polymerising individual proteins into a closed filament one can multiply the resulting deformations, which can ultimately lead to membrane fission such as in the case of FtsZ rings [66, 67].[11] The general expressions for N closed parallel filaments can be found in appendix C.4. In order to illustrate these expressions, let us consider the case of one torque-exerting closed filament ring first. A purely circular filament ($n = 0$), which does not exert any force on the membrane, does not displace the membrane at the position

---

[9] The cytoskeleton or the other proteins must themselves be coupled to the membrane to reach mechanical equilibrium.

[10] Interestingly, for a single point torque, the system is not at mechanical equilibrium, however, in the Monge approximation, rotation of the whole system is highly energetic. This implies that the system does not rotate, and seems at equilibrium. Therefore, for a system of point torques, the superposition principle can safely be applied.

[11] Note that one can show that a twister on a tubular membrane preferentially orients along the longitudinal axis of the tube.

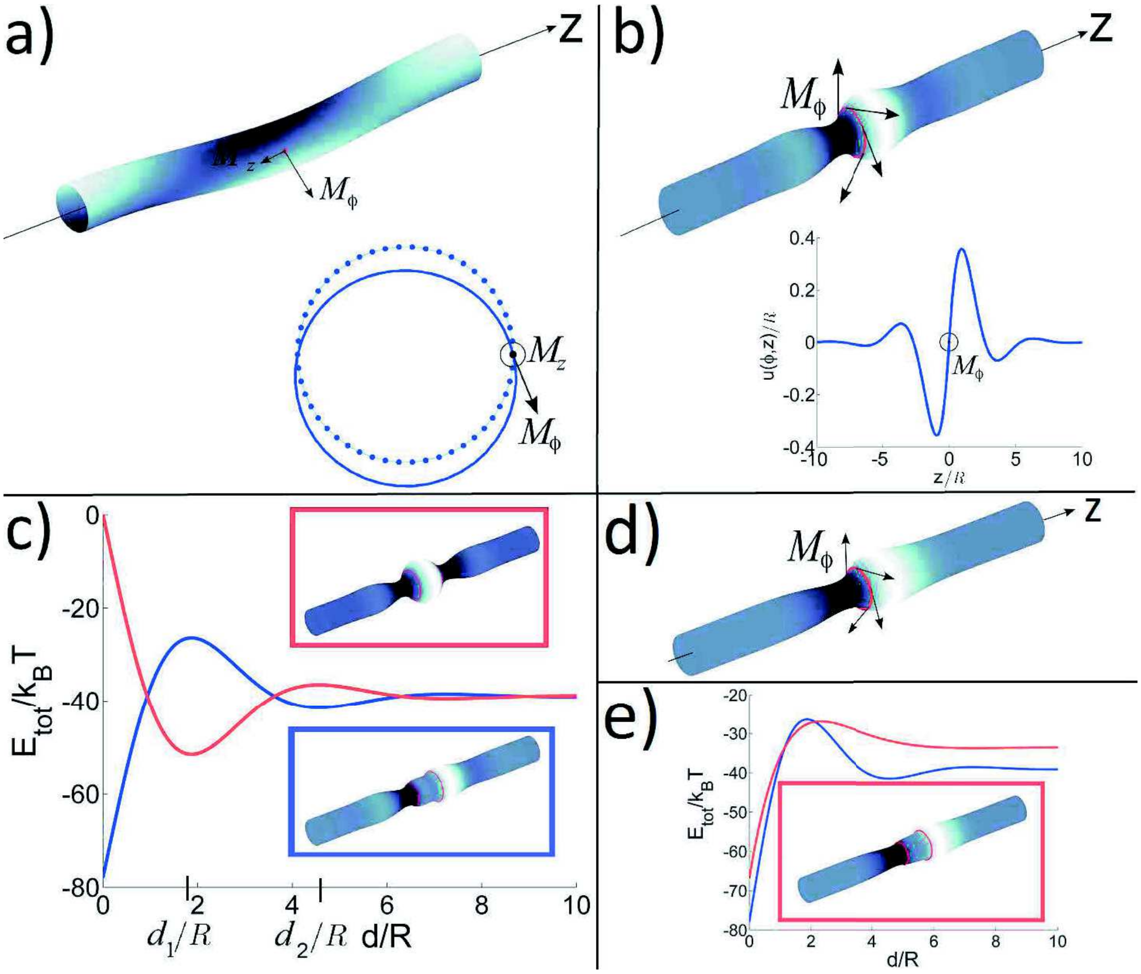

Figure 3.6: Deformations of a tubular membrane due to (a) a single point torque, and (b) a circular filament. (c) Total energies and equilibrium shapes of two interacting circular torque distributions. The blue curve in the energy diagrams correspond to the case of parallel torques, the red curve to the case of opposite torques. Note that all these figures correspond to the case of vanishing longitudinal force ($\gamma = 0$). (d) Deformations of a tubular membrane due to a circular filament for $\gamma = 2.2$. In this regime, the surface tension and difference of pressure both are positive. (e) Total energies of two interacting circular torque distribution for $\gamma = 0$ in blue and $\gamma = 2.2$ in red. In the red box, the equilibrium shape for $\gamma = 2.2$ is represented.

where it is situated, *i.e.*, $u(\phi, z_1) = 0$. A local torque density $M_{z,0}$ in the z-direction will not deform the membrane, as the corresponding force doublets cancel each other when adjacent local forces are summed up individually along the filament. The corresponding contribution to the energy of the system is zero (see Eq. (C.28)). However, the total torque of such a torque distribution is oriented along the z axis and cannot be equilibrated by the membrane due to its fluidity. We will thus set $M_{z,0} = 0$ in the following. Local torques in the ϕ-direction can be equilibrated.

The displacement field and the energy of a tubular membrane with a circular filament at $z = z_1$ thus read (see appendix C.4)

$$E = -\frac{\pi (M_{\phi,0})^2}{B_m L/R} K_0 \tag{3.35}$$

and

$$u(\phi, z) = \frac{M_{\phi,0}}{B_m} \sum_{m=-\infty}^{\infty} \frac{k_m R^2}{M_{0,m} L/R} \sin(k_m(z - z_1)) \ , \tag{3.36}$$

where $K_0 = \sum_{m=-\infty}^{\infty} \frac{(k_m R)^2}{M_{0,m}}$ (see appendix B.3 for these expressions in the large L limit). One observes an infinite number of oscillations of sharply decreasing amplitude (see Fig. 3.6 (b)). These oscillations in the radius of the tube can be explained by the competition between the pressure P, the surface tension σ and the rigidity of the membrane B_m [68].

How do several of these filaments interact with each other? To get a hold on this question, we will focus on two closed torque-exerting bio-filaments (see appendix C.4 for a discussion of the general case). The length of the filaments is not fixed but depends on the distance between them since we are working in the fixed forces and torques ensemble. General expressions for the interaction between the filaments can be determined by using the stress tensor approach [123, 124, 125]. In this article we take the standard approach by studying the energy of the system.

In order to illustrate the interactions between two such filaments, let us consider two equivalent closed circular torque distribution. The energy of the system and the radial displacement field read

$$E_{tot} = -\frac{\pi}{B_m L/R} \left(\left(\left(M_{\phi,0}^{(1)} \right)^2 + \left(M_{\phi,0}^{(2)} \right)^2 \right) K_0 + 2 M_{\phi,0}^{(1)} M_{\phi,0}^{(2)} N_0 \right) \tag{3.37}$$

and

$$u(\phi, z) = \frac{R}{B_m L/R} \sum_{m=-\infty}^{\infty} \sum_{j=1,2} \frac{k_m R}{M_{0,m}} M_{\phi,0}^{(j)} \sin(k_m(z - z_j)). \tag{3.38}$$

Equivalent expressions for more complicated cases can directly be obtained from Eqs. (C.30) and (C.31). In particular, the ellipsoidal distribution of torques, the "crunching ring" described in the previous chapter, is discussed in details in appendix C.5.

The energy of two circular torque distributions, Eq. (3.37), exhibits a damped oscillatory behaviour (see Fig. 3.6 (c)). One finds that the local extrema are at the distances $d_N \approx \frac{\sqrt{2}}{\sqrt{\sqrt{3}+1}} \left(\tan^{-1}(-\sqrt{2}) + N\pi \right) R$ with $N \in \mathbb{N}$. Whereas $d = 0$ and $d_2 \approx 4.558R$ are the lowest minima for the case of parallel torques (blue curve), one finds the global minimum for the case of opposite torques at $d_1 \approx 1.871R$. It is interesting to note that increasing the value of the longitudinal force F smoothens the oscillatory behaviour as shown on Fig. 3.6 (d). Moreover, one finds that the energy barriers to cross from principal to secondary minima, and *vice versa*, are reduced (see Fig. 3.6 (e)). Finally, the principal minimum is wider for $F > 0$.

Can two circular torque distributions with parallel torques overcome the energy barrier and get from the first local into the global minimum? To answer this question in a realistic setting, consider a membrane of bending rigidity $B_m = 15k_BT$, radius $R = 50$ nm, and length $L/R = 100$. One finds that rings of 30 proteins, applying a torque of the order of $0.5k_BT$ each, can cross the energy barrier which is around $15k_BT$. On the contrary, the rings will most likely stay in the global minimum once they are in this configuration since the energy barrier to cross to get to the next minimum is approximatively $50k_BT$. Note that these energies are large, and imply deformations slightly larger than the one we should consider in the linear regime.

3.4 Torque-induced membrane wrapping

Motivated by biological filaments such as dynamin [114, 126] and filopodia [128], we finally consider how a helical filament can deform a tubular membrane when wrapping around it. In contrast to previous work [62, 63] we focus on the question what happens when the filament applies a constant local torque distribution instead of a force. Similar shapes can, for example, be found in several other biological entities such as bacteria [127] or plant cells [129]. One note of caution is, however, due here. Our theoretical results are in the linear regime albeit non-linear effects will surely play an important role in a biophysical setting at high deformation.

For such a filament Eq. (C.8) of appendix C.1 can be written as:

$$E_{fil} = -\int_{\phi_{min}}^{\phi_{max}} d\phi \int_{-L/2}^{L/2} dz \delta\left(z - \frac{\ell\phi}{2\pi}\right)\left(M_\phi \frac{du(z,\phi)}{dz} - \frac{M_z}{R}\frac{du(z,\phi)}{d\phi}\right), \tag{3.39}$$

where the displacement field $u(\phi, z)$ is given by Eq. (3.26) and ℓ is the pitch of the helix. As previously, the system must be at mechanical equilibrium, which implies that the filament cannot apply a constant local torque along the z direction, *i.e.*, $M_z = 0$. We will focus on the case of an infinite filament of length $L \gg R$ wrapping around an infinite membrane. To simplify the mathematical treatment we assume that the azimuthal angle ϕ lies in an interval which is proportional to 2π, such that $\phi_{max} - \phi_{min} = 2\pi N$. The helix turns $N \in \mathbb{N}$ times and its length is $L = N\ell$. The energy and the displacement field of such a system summed over all the modes read:

$$E_{tot} = -\frac{\pi^2 L/R\left(\frac{2\pi}{(\ell/R)^2}M_\phi\right)^2}{B_m\sqrt{\Delta}}\left(A\cot\left(A\pi\right) - B\cot\left(B\pi\right)\right) \tag{3.40}$$

and

$$u(\phi, z) = -\left(\frac{2\pi}{\ell/R}\right)^2 \frac{M_\phi R}{2B_m\sqrt{\Delta}} \left(\frac{\sin\left((\pi - \phi + \frac{2\pi}{\ell}z)A\right)}{\sin\left(A\pi\right)} - \frac{\sin\left((\pi - \phi + \frac{2\pi}{\ell}z)B\right)}{\sin\left(B\pi\right)}\right), \tag{3.41}$$

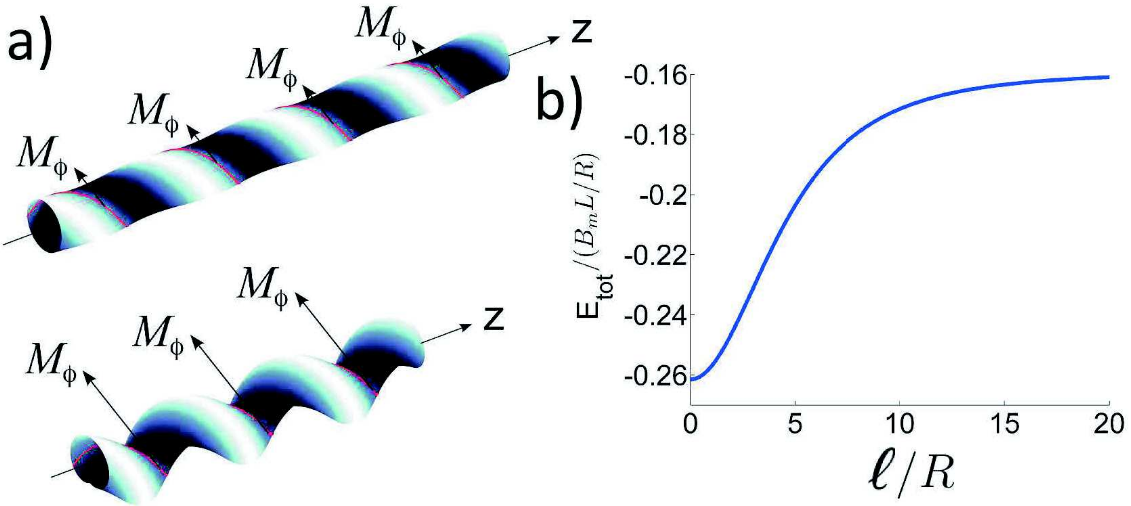

Figure 3.7: (a) Deformations of a tubular membrane due to a helical torque distribution with low (*up*) and high (*down*) M_ϕ. (b) Energy profile as a function of the reduced pitch of the filament ℓ/r.

where $\sqrt{\Delta} = 2\sqrt{1 - 2\left(\frac{2\pi}{\ell/R}\right)^2 - 2\left(\frac{2\pi}{\ell/R}\right)^4}$, $A = \frac{\sqrt{\left(\frac{2\pi}{\ell/R}\right)^2 + 2 - \frac{\sqrt{\Delta}}{2}}}{\left(\frac{2\pi}{\ell/R}\right)^2 + 1}$, $B = \frac{\sqrt{\left(\frac{2\pi}{\ell/R}\right)^2 + 2 + \frac{\sqrt{\Delta}}{2}}}{\left(\frac{2\pi}{\ell/R}\right)^2 + 1}$, and $0 < \phi - \frac{2\pi}{l} z < 2\pi$.[12]

Interestingly, the membrane reshapes in such a way that the whole tube coils. Since the filament is supposed to be much stiffer than the membrane, the pitches of the membrane and the filament are the same (Fig. 3.7 (a)). In the intermediate regime, *i.e.*, when the filament and the membrane have a stiffness of the same order of magnitude, the pitch of the filament and the one of the helix will be different.

Can the deformations lead to a breakage of the tubular membrane? To answer this question, let us discuss the energy and its associated shape. The energy (3.40) decreases quadratically for increasing local torque M_ϕ and fixed pitch. This leads to a supercoiling of the membrane (Fig. 3.7 (a)). When the torque is high enough, two pieces of the membrane start to touch each other, and the membrane penetrates itself.

When this phenomenon of auto-penetration starts, the membrane can, in principle, break, leading to a collapse of the tube. Subunits, which are susceptible to apply a Darboux torque (see Sec. 3.1) can thus induce a fission of the membrane by polymerising into a helical filament. One word of caution is, however, due here: our calculations are in the linear regime and are thus only valid when the amplitude of deformation $D = \frac{\partial u}{\partial z}$ is much smaller than 1, *i.e.*, $D \ll 1$. For simplicity, let us study the amplitude at $z = \phi = 0$. One

---

[12] Note that the total torque applied to the tubular membrane is directly related to the torque per protein *via* the expression $m_\phi = \frac{b/RM_\phi}{2\pi N\sqrt{1+\left(\frac{\ell/R}{2\pi}\right)^2}}$, where b is the size of the protein.

finds:

$$D = -\left(\frac{2\pi}{\ell/R}\right)^3 \frac{M_\phi}{2B_m\sqrt{\Delta}} \left(A\cot\left(A\pi\right) - B\cot\left(B\pi\right)\right). \tag{3.42}$$

At first order, for $\ell/R \to 0$, $D \approx -\frac{M_\phi}{12B_m}\ell/R$, and for $\ell/R \to \infty$, $D \approx -\frac{M_\phi}{2\pi^2 B_m}\ell/R$. For a fixed local torque M_ϕ, the energy (3.40) increases non-linearly for increasing pitch ℓ (see Fig. 3.7 (b)). In the limit of $\ell/R \to 0$, the torque applied by the filament can be slightly larger than the membrane stiffness, without going into the non-linear regime.

3.5 Conclusions

We have discussed the reshaping of flat and tubular fluid membranes under the constraints of adhering stiff filaments. To force an amphiphilic filament to adhere to a membrane, one in general has to apply a prestress to the filament, such that its hydrophobic part penetrates and orients itself normal to the membrane. Depending on the applied prestress, this can induce a local torque distribution and thus a deformation of the membrane. This phenomenon leads to mechanical equilibrium as long as all local torques compensate each other.

In our study we have considered different kinds of bio-filaments. With the help of linear response theory we were able to derive general expressions for the membrane shape in terms of the torques applied by the filament. Specializing these expressions allowed us to analyse the reaction of the membrane to the *twister* and the *bender*, *i.e.*, two adjacent opposite point torques along, and perpendicular to the backbone of the filament, respectively. The twister, for instance, corresponds to a straight filament with a helical hydrophobic region. The bender corresponds to a bent filament, with its hydrophobic part in the inner or outer sides of the curved filament. The long-range interactions of two twisters have been discussed for distances larger and smaller than the characteristic length λ.

Allowing the monomers to polymerise to form closed filaments, we have studied the lowest mode of deformation of one single filament applying a local torque distribution. The interaction between two equal filaments can be repulsive or attractive depending on the respective orientations of the torques. When the filaments apply the same torque distribution, the global minimum corresponds to the configuration where both filaments are on top of each other. One finds local minima which are more stable than in the case of the point torque. An estimate using physical values for two circular filaments yields a separation of 225 nm with a barrier of about $15\,k_BT$ when each monomer applies a torque of about $1\,k_BT$.

Finally, we specialised our formalism to the case of a helical filament applying a constant torque locally. Increasing this torque leads to a supercoiling of the membrane which could subsequently induce membrane fission in the non-linear regime similar to what is observed in biological systems containing, for example, dynamin filaments.

Chapter 4

The Spiroplasma

Biological cells and bio-filaments interactions are also involved in the cell motility. For instance, unicellular organisms move by following gradients of chemicals. This is the so-called chemotaxis. Most of the bacteria follow sugar gradients[1], which will be utilised to transform Adenosine diphosphate (ADP) into Adenosine triphosphate (ATP), which is one of the main nucleotides used by bio-filaments to perform work [2]. This chemical reaction is the so-called fermentation [3]. The inverse reaction to the latter one is activated by the hydrolysis of ATP. The ATP nucleotide is transformed into ADP and a phosphate molecule.

4.1 Cell motility

To follow the gradients of sugar, most of the bacteria display one or several flagella. For example, the bacteria *Salmonella*, which cause typhoid fever or *E. Coli*, which are present in mammal gastrointestinal tract, use a flagellum to move. Interestingly some eukaryotic cells also display a flagellum. This is for instance the case of sperm cells. Nonetheless, the flagella differ in their way of functioning. Indeed, in prokaryotic cells, flagella work on the basis of a motor which induces the movement of a rotor (see Fig.4.1 (a)). The bacterial flagella are composed of a lot of proteins. In particular, flagellin is the protein which assembles to form the filament outside of the bacteria, *i.e.*, the rotor. This outer filament is linked to the cell wall *via* a hook. Due to the rotation of the rotor, the bacterium moves.

On the other hand, in eukaryotic cells, flagella, which are organelles, are activated by the action of dynein motors on microtubules (see Fig. 4.1 (b)). Eukaryotic flagella are long entities which are organised in an ordered assembly of microtubules known as the

---

[1] Interestingly, some bacteria -like cyanobacteria- are photosynthetic, meaning that they produce sugar via a chemical reaction:

$$6H_2O + 6CO_2 \rightarrow C_6H_{12}O_6 + 6O_2. \tag{4.1}$$

The reaction between the water and carbon dioxide molecules is activated by light, which are transformed into sugar and dioxygen. This sugar is then used for fermentation. These kind of bacteria do not need to move to get sugar. However, the need of water might force them to do so.

[2] The other nucleotide furnishing energy is GTP as already mentioned in the previous chapters. It arises from the chemical reaction between sugar and GDP.

[3] The reaction is complex as other molecules also are involved in it.

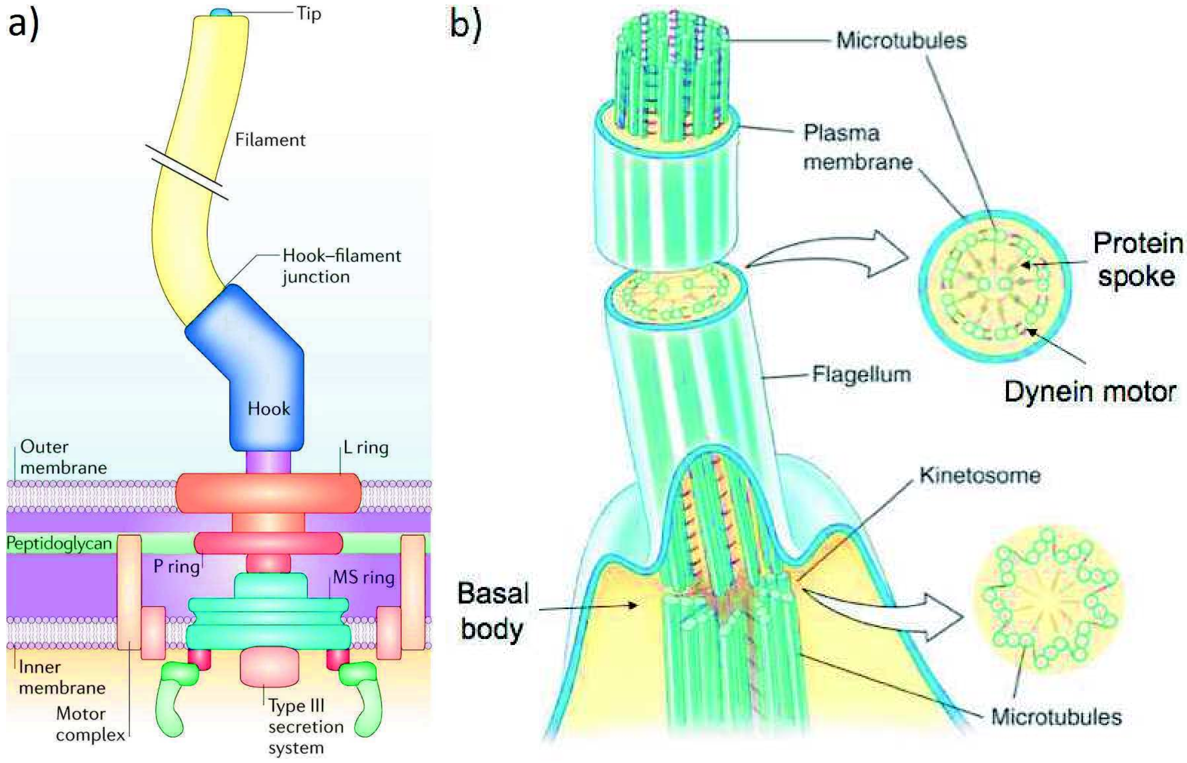

Figure 4.1: Scheme of flagella in (a) prokaryotic [130] and (b) eukaryotic [131] cells.

axoneme. The axoneme is in general composed of a cylindrical tube made of 9 doublets of microtubules. Along all microtubules, one finds dynein motors, which can move upon ATP hydrolysis along the microtubules. These doublets are linked thanks to a protein called Nexin. In the center of this tube, one finds two microtubules which are also linked to each other thanks to Nexin proteins. Moreover, the so-called Protein Spoke, also known as the Radial Spoke is a protein linked to the microtubule doublets and pointing towards the two central microtubules. The role of these proteins on the motility of the cell is poorly understood yet. Nonetheless, it is known that dynein motors exert forces inducing the gliding of the microtubules. The Nexin proteins play an important role in converting the gliding of the microtubules into curvature.

Eukaryotic cells can also display an other way of locomotion: the cilia. The cilia are structurally close to the flagella. The axoneme is for instance also present in cilia. There are three important differences between these two organelles. As mentioned above, flagella are long filaments, which is not the case of cilia. Indeed, cilia are short appendages. Secondly, there are usually less than 10 flagella for a single eukaryotic cell, where one can find hundreds of cilia for a single cell. Finally, the motion of the cilia and the flagella are also different. Where flagella show a two-dimensional wave-like behaviour, cilia present a more complicated three-dimensional movement (see Fig. 4.2).

Interestingly, cells can move by means of several other mechanisms. For instance, cells can adhere to surfaces, and thanks to the action of actin filaments, polymerisation, adhe-

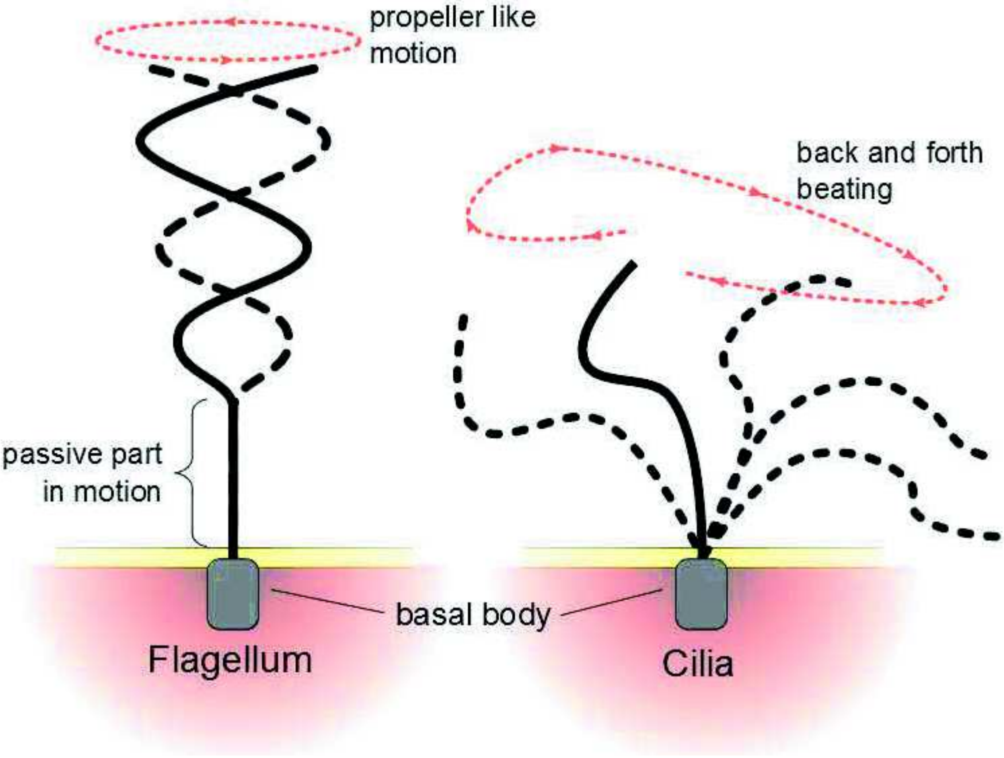

Figure 4.2: Scheme of the differences between the motions and shapes of the flagella and the cilia [132].

sion and de-adhesion process, can move [133]. Indeed, one side of the cell adheres to the surface. On the other side, the cell detaches from the surface, and after contraction of the actin filaments at this location, the cell moves to the newly attached point. Moreover, cells can also have passive motions, meaning that they do not present any intrinsic way of locomotion, but rather let the environment move it. This is for instance the case of red blood cells, which are just pumped through the blood vessels. An other interesting motility apparatus is the one of multicellular organisms. In particular, we, like animals, use our muscles to move. The contraction of the muscles is principally driven by myosin motors and actin filaments in *sarcomeres*. Sarcomeres are the basic unit of the muscle tissues. All these mechanisms, except for the passive motility are governed by the filaments of the cytoskeleton of the eukaryotic cells.

A lot of the prokaryotic cells possess a cytoskeleton involved in cell division, for instance, and move thanks to flagellum, which can be seen as a part of the cytoskeleton too. Nonetheless, not all prokaryotic cells possess a flagellum, but still can move. In particular, this is the case of the bacteria *Spiroplasma melliferum* which can be responsible for a cataract.

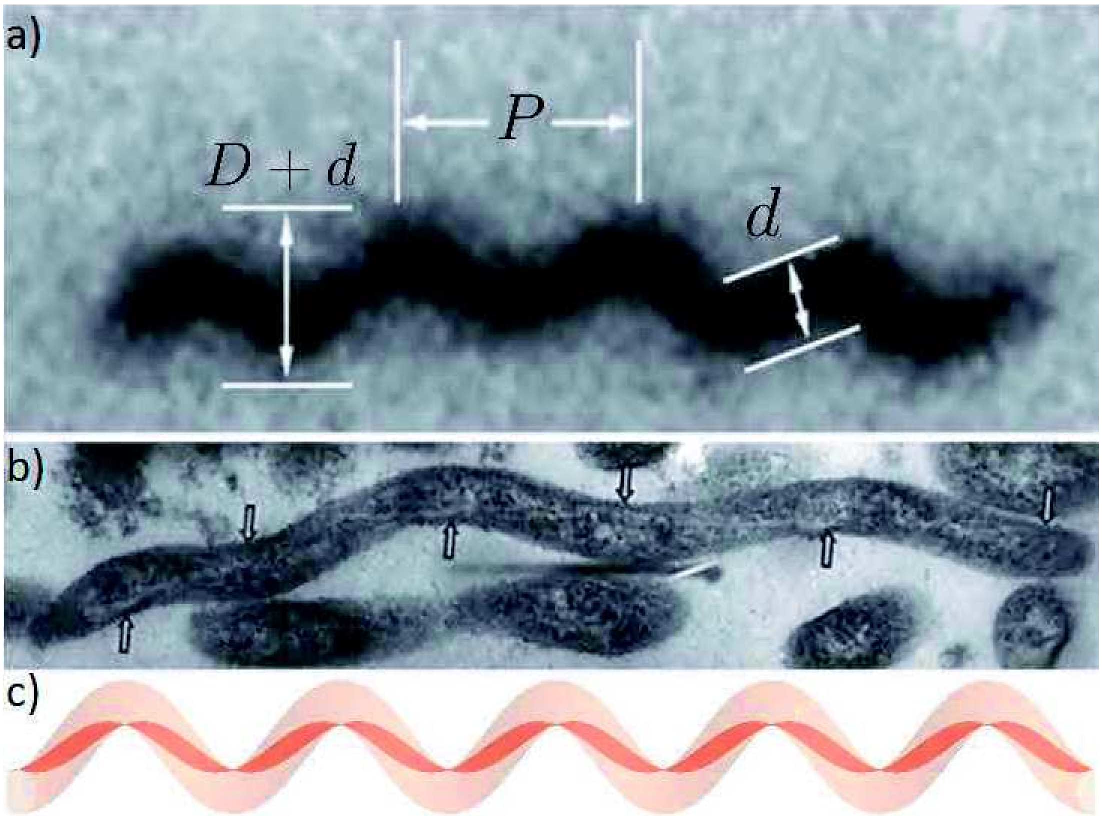

Figure 4.3: A Spiroplasma cell, its geometry and cytoskeletal organisation. a) High-intensity, dark-field video image (with reversed contrast) of Spiroplasma melliferum BC3 cells [134, 135]. The cell is approximatively in the focal plane and normal to the optical axis of the microscope. $P \approx 0.9$ μm, $d \approx 0.2$ μm and $d + D \approx 0.6$ μm correspond to the pitch, the cell diameter and the coil diameter, respectively. b) Electron micrograph image which shows the interior of a longitudinal, median thin section of the cell [134, 135]. The cytoskeletal ribbon follows the shortest helical path and is localised by the arrows. c) Scheme of an average Spiroplasma cell. The bacterial cytoskeleton is represented by the colored surface.

4.2 Description of the Spiroplasma

Spiroplasmas are members of the so-called *Mollicutes* class of organisms. The Mollicutes are the smallest and simplest living and self-replicating cells [136]. On the one hand, the smallest genome of this kind of organisms (the one of *Mycoplasma genitalium* which is responsible of urethritis for instance) is only two times larger than the one of a virus. On the other hand, the largest genome (the one of Spiroplasma LB 12) is two times smaller than the one of *E. Coli* [137]. In addition to their lack of flagellum, Mollicutes are special in the sense that they lack a cell wall. Instead of this wall, they possess what can be defined as a bacterial cytoskeleton.

Spiroplasmas are even more unique bacteria as they display a well-defined helical structure, where most of the bacteria are rod-like shaped. This particular shape principally

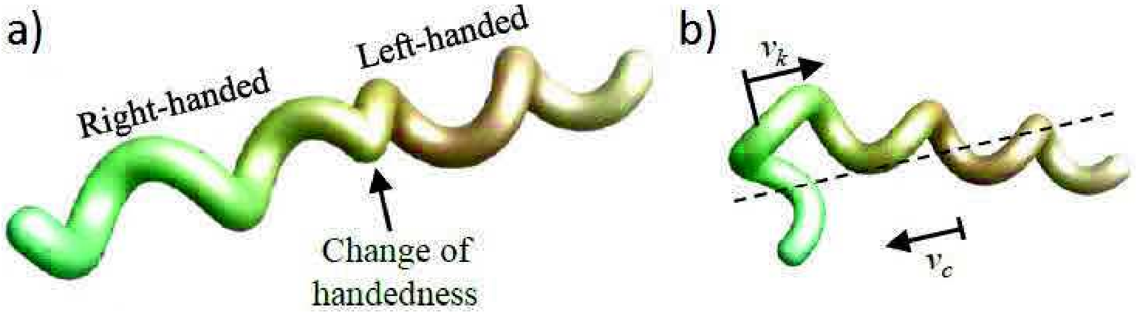

Figure 4.4: a) Scheme representing the change of handedness and b) the propagation of the kink along the Spiroplasma [140].

comes from the shape of its cytoskeleton, which is composed of several proteins, such as FtsZ or MreB, but also a protein specific to the Spiroplasma: the *fib* protein [138, 139]. The subunit (when the Spiroplasma is at rest) can be seen as a circular tetramer of diameter $\approx$ 10 nm [100]. These tetramers assemble in order to form long fibrils. Moreover, 7 of these fibrils assemble in the orthogonal direction, forming a thin elastic sheet parallel to the membrane. The *fib* fibers can not attach directly to the membrane, thus involving MreB proteins. The MreB proteins lie between the *fib* fibers and the cell membrane. Interestingly, this cytoskeleton lies on the shortest helical path along the body. It is assumed that the MreB filaments give the cell a rod-like shape (similarly to other bacteria), but the *fib* proteins are responsible of the helicity of the cell [98]. On the average, Spiroplasma cells are made of approximatively 5 helical turns (Fig. 4.3 (c)). The unit helical repeat of the cell is $P \approx 900$ nm long, the whole cell being ≈ 4.5 μm long. The diameter of the cell tube is $d \approx 190$ nm, and the coil diameter is $d + D \approx 570nm$, such that $D \approx 2d$.

Similarly to eukaryotic cells, Spiroplasmas move thanks to their cytoskeleton. Indeed, the *fib* tetramers can switch from a circular to an ellipsoidal state upon ATP hydrolysis. The contraction of the fibers leads to a change of the length and a change of helicity of the thin elastic cytoskeleton. This change in the helicity of the cytoskeleton induces the same behaviour of the membrane of the cell locally. Interestingly, the contraction of the cytoskeleton begins at one end of the cell. To join the different handedness, the membrane bends, and in order to release the stress, the cell kinks. It is the propagation of this kink at a given speed v_k that moves the Spiroplasma. Indeed, when the kink propagates along the body of the cell, it creates a hydrodynamic flow which gives rise to the movement of the cell at the speed v_c in the direction opposite to the kink (see Fig.4.4).

The propagation of this kink has been studied both experimentally and theoretically [99, 141]. Shaevitz *et al.* studied experimentally the propagation of kinks in long Spiroplasma cells. The number of helical repeats was close to 10. In this particular case of long bacteria, the cell does not kink once, but twice. The first kink propagates along the bacteria, and after a certain distance, a second kink propagates at the same speed and in the same direction. The angle between the two opposite helicities θ_{bend} has been found to be close to 35°. In standard medium, kinks moved along the cell at a speed of $v_k \approx 10.5$ μm.s^{-1}. Cells themselves moved at a speed of $v_c \approx 3.3$ μm.s^{-1} in the direction opposite to the one of the kink. In the theoretical model developed by Wada and Netz, they considered the cytoskeleton as a thin helical elastic rod. They found, according to simulations, an angle $\theta_{bend} \approx 31°$ for an optimal propulsion efficiency, which is close to the one obtained in the latter experiment ($\theta_{bend} \approx 35°$). However, with their simulation parameters, they found that the ratio of the cell and kink speed are close to 7%. The cell according to their model is slower than the one found in experiments.

4.3 The cytoskeleton as a thin elastic sheet

In our model, we propose, unlike Wada and Netz, to treat the cytoskeleton as a thin elastic sheet. According to the experiments done by Trachtenberg [134, 142], the width of the cytoskeleton w is approximatively 7 times larger than its thickness t. The length of the cytoskeleton L is equal to the length of the Spiroplasma itself (few microns), such that we can assume that $L \gg w \gg t$. The cytoskeleton is seen as a thin elastic sheet. Typically, one solves the Föppl-Von Kármán equations, in order to get a solution for thin elastic sheets. For instance, this theory has been used to describe the shape of leafs by taking into account edge stresses due to their growth [143]. In the latter theory, it is assumed that the sheet can bend (similarly to membranes), but also stretch. Similarly to the membrane theory, the displacement and the strains must be small. It is also assumed that after deformation, the normal of the surface still corresponds to the initial normal of the surface (Monge frame). An other assumption, is that the studied surface is flat initially, and deforms due to the constraints applied to it. The energy of the surface can be divided in two quantities, the bending and the stretching energy, which read:

$$E_b = \frac{Yt^3}{24(1-\nu^2)} \iint dx\ dy \left((\Delta\omega)^2 - (1-\nu)[\omega,\omega] \right) \tag{4.2}$$

and

$$E_s = \frac{Yt}{2(1-\nu^2)} \iint dx\ dy \left((\epsilon_{xx}+\epsilon_{yy})^2 - 2(1-\nu)\left(\epsilon_{xx}\epsilon_{yy} - \epsilon_{xy}^2\right) \right), \tag{4.3}$$

where Y and ν correspond to the Young modulus and the Poisson ratio, respectively. Furthermore, t and ω correspond to the thickness of the surface and the out-of-plane displacement field, respectively. $\frac{[\omega,\omega]}{2} = \left(\frac{\partial^2\omega}{\partial x^2}\frac{\partial^2\omega}{\partial y^2} - \left(\frac{\partial^2\omega}{\partial x \partial y}\right)^2 \right)$ corresponds to the Gaussian curvature, and the $\epsilon_{\alpha\beta}$ are the components of the strain tensor. Minimising the elastic energy $E_{el} = E_s + E_b$ with respect to the displacements u_x, u_y[4] and ω leads to 3 equations, which correspond to the in and out-of-plane mechanical equilibrium equations, and read:

$$\begin{aligned} &\frac{Yt^3}{12\left(1-\nu^2\right)}\Delta^2\omega - t\frac{\partial^2}{\partial x_\alpha \partial x_\beta}\sigma_{\alpha\beta} = 0 \\ &\frac{\partial \sigma_{\alpha\beta}}{\partial x_\beta} = 0 \quad \text{for} \quad \alpha = x, y, \end{aligned} \tag{4.4}$$

---

[4] The in-plane displacements u_x and u_y are directly linked to the strain components *via* $\epsilon_{\alpha\beta} = \frac{1}{2}\left(\frac{\partial u_\alpha}{\partial x_\beta} + \frac{\partial u_\beta}{\partial x_\alpha} + \frac{\partial u_\gamma}{\partial x_\alpha}\frac{\partial u_\gamma}{\partial x_\beta}\right)$.

where the $\sigma_{\alpha\beta}$ are the components of the stress tensor.

Interestingly, in our system, the sheet is a highly curved and twisted surface. We thus can not just solve the Föppl-Von Kármán equations and get the solution to our problem as we are not any more in the Monge approximation. In the paper of Efrati *et al.* [144], they describe a theory for what they call non-Euclidean plates. Non-Euclidean plates are a class of elastic bodies which do not display any stress-free configuration. This theory is also applicable to surfaces with a stress-free configuration, and is not restricted to the Monge frame. This theory is thus useful to treat the problem of the Spiroplasma.

Thanks to a few assumptions similar to the one of the Föppl-Von Kármán theory, one finds that the elastic energy reads $E_{el} = E_s + E_b$, where

$$E_s = t \int \omega_s \sqrt{|\bar{g}|} dx^1 dx^2 \tag{4.5}$$

and

$$E_b = t^3 \int \omega_b \sqrt{|\bar{g}|} dx^1 dx^2, \tag{4.6}$$

where the $\bar{g}_{\alpha\beta}$ are the components of the reference metric, and $|..|$ denotes the determinant of the matrix. Moreover, x^1 and x^2 correspond to the two variables describing the surface and the integral is performed over the whole surface. Finally, the energy densities are given by:

$$\omega_s = \frac{Y}{8(1+\nu)} \left(\frac{\nu}{1-\nu} \bar{g}^{\alpha\beta} \bar{g}^{\gamma\delta} + \bar{g}^{\alpha\gamma} \bar{g}^{\beta\delta} \right) (a_{\alpha\beta} - \bar{g}_{\alpha\beta}) (a_{\gamma\delta} - \bar{g}_{\gamma\delta}) \tag{4.7}$$

and

$$\omega_b = \frac{Y}{24(1+\nu)} \left(\frac{\nu}{1-\nu} \bar{g}^{\alpha\beta} \bar{g}^{\gamma\delta} + \bar{g}^{\alpha\gamma} \bar{g}^{\beta\delta} \right) b_{\alpha\beta} b_{\gamma\delta}, \tag{4.8}$$

where $a_{\alpha\beta}$ and $b_{\alpha\beta}$ correspond to the first and second fundamental forms of the mid-surface of the constrained sheet[5] and $\bar{g}^{\alpha\beta}$ are the components of the inverse reference metric. Similarly to the Föppl-Von Kármán theory, one can minimise the energy and find a set of equations that need to be solved by taking into account boundary conditions (see appendix D.1).

4.4 Preliminary results and perspectives

In our model, let us first assume that the cytoskeleton is flat at rest, and that it is its interaction with a sheet of MreB proteins that leads to a prestrain. We think that the prestrain leads to a symmetry breaking and the formation of left or right-handed helices as shown in Fig. 4.5. Moreover, the cytoskeleton follows the shortest helical path along the

---

[5] The first fundamental from corresponds to the metric of the surface, while the second fundamental form is directly linked to the principal curvatures of the surface.

body of the bacterium. It is interesting to notice that the Gaussian curvature of the sheet then is negative. We assume that the negative Gaussian curvature plays an important role in the mechanism of sheet positioning and kink propagation.

In the following, we only consider the cytoskeleton, as we assume it to be stiffer than the biological membrane. Indeed, it is the cytoskeleton that gives the shape of the bacterium, and not the cell membrane. Following the theory developed by Efrati *et al.*, we first need to define the parameters of the sheet in its reference state, but also in its final state. All the geometric parameters of the sheet (first and second fundamentals, Christoffel symbols and mean and Gaussian curvatures) are given in appendices D.2. The useful one for this calculation are the first and second fundamental forms of the surface, which read:

$$\begin{aligned} a_{11} &= (1-R\kappa\cos(\phi))^2+R^2\tau^2 && \text{and} \quad b_{11}=\kappa\cos(\phi)\left(1-R\kappa\cos(\phi)\right)-R\tau^2 \\ a_{12} &= R\tau && \text{and} \quad b_{12}=-\tau \\ a_{22} &= 1 && \text{and} \quad b_{22}=-\frac{1}{R}, \end{aligned} \tag{4.9}$$

where R is the radius of curvature of the sheet, and $\tau=\frac{h}{h^2+r^2}$ and $\kappa=\frac{r}{h^2+r^2}$ are the torsion and curvature of the centerline defining the center of the circle of radius R.

Implementing all these parameters in the energy densities (Eq. 4.7 and 4.8), we found that the energy densities read:

$$\omega_s=\frac{Y}{8(1-\nu^2)}\left((1-R\kappa\cos(\phi))^2+R^2\tau^2-1\right)^2+\frac{Y}{4(1+\nu)}R^2\tau^2 \tag{4.10}$$

and

$$\begin{aligned}\omega_b =&\frac{Y}{24(1-\nu^2)}\left(\kappa\cos(\phi)\left(1-R\kappa\cos(\phi)\right)-R\tau^2-\frac{1}{R}\right)^2\\ &+\frac{Y}{12(1+\nu)}\frac{\kappa}{R}\cos(\phi)\left(1-R\kappa\cos(\phi)\right). \end{aligned}\tag{4.11}$$

As a first conclusion, one sees that the energy of the right or left-handed helix, for the same curvature and pitch are the same. Nonetheless, the strains differ, depending on the helicity of the sheet. Indeed, the $2D$ strain tensor $\epsilon^{2D}_{\alpha\beta}=\frac{1}{2}\left(a_{\alpha\beta}-\bar{g}_{\alpha\beta}\right)$ can be rewritten as:

$$\begin{pmatrix}\epsilon^{2D}_{11}\\ \epsilon^{2D}_{22}\\ \epsilon^{2D}_{12}\end{pmatrix}=\begin{pmatrix}\frac{1}{2}\left((1-R\kappa\cos(\phi))^2+R^2\tau^2-1\right)\\ 0\\ \frac{R\tau}{2}\end{pmatrix}. \tag{4.12}$$

Note that one can find the stresses thanks to the Kirchhoff-Love assumptions which lead the following strain-stress relation:

$$\begin{pmatrix}\sigma^{2D}_{11}\\ \sigma^{2D}_{22}\\ \sigma^{2D}_{12}\end{pmatrix}=\begin{pmatrix}1&\nu&0\\ \nu&1&0\\ 0&0&1-\nu\end{pmatrix}\begin{pmatrix}\epsilon^{2D}_{11}\\ \epsilon^{2D}_{22}\\ \epsilon^{2D}_{12}\end{pmatrix}. \tag{4.13}$$

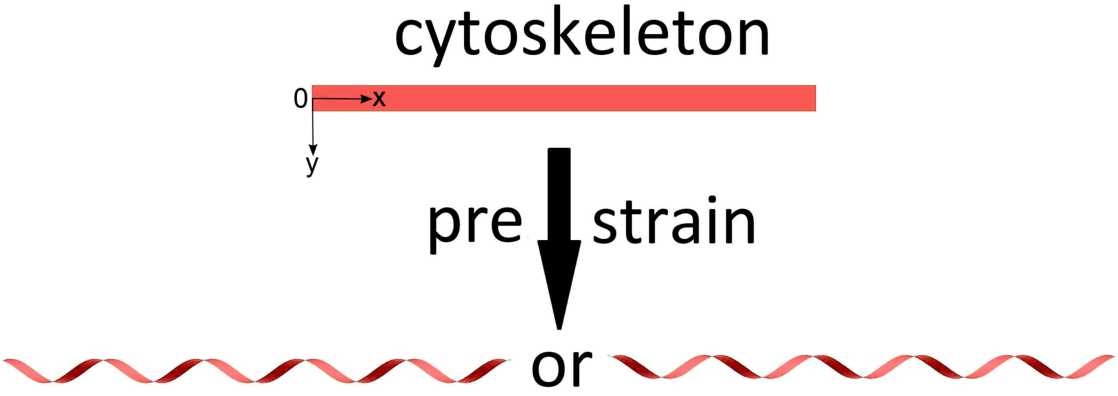

Figure 4.5: Schematic representation of the Spiroplasma. *Up*: The cytoskeleton in its ground state. *Down*: The cytoskeleton in a Spiroplasma bacterium in its rest configuration.

It is clear from these expressions that for right and left-handed helical sheets, the strains ϵ_{11}^{2D} and ϵ_{22}^{2D} are equal. However, the strains ϵ_{12}^{2D} are opposite for the two different torsions $\pm\tau$. Symmetry breaking will be absent as the energies of the left and right-handed helices are larger than the energy of the flat sheet. The following step is thus to prestrain the flat cytoskeleton and see how it will minimise its energy. As an ansatz, we impose a prestrain of the form:

$$\epsilon_{xx}^{2D} = \frac{\epsilon_0}{2}\left(\left(\frac{y}{w}\right)^2 - \frac{1}{3}\right), \tag{4.14}$$

which corresponds to a longitudinal elongation of the sheet with a parabolic-like stretch distribution. In addition, the sum of all prestrains is assumed to be equal to zero.

The new surface can be described by the following first fundamental form:

$$\bar{g}_{\alpha\beta} = \begin{pmatrix} 1+\epsilon_0\left(\left(\frac{y}{w}\right)^2 - \frac{1}{3}\right) & 0 \\ 0 & 1 \end{pmatrix} = \begin{pmatrix} \bar{g} & 0 \\ 0 & 1 \end{pmatrix}, \tag{4.15}$$

the inverse metric

$$\bar{g}^{\alpha\beta} = \begin{pmatrix} \frac{1}{\bar{g}} & 0 \\ 0 & 1 \end{pmatrix}. \tag{4.16}$$

The sheet being prestrained to adopt this conformation according to our ansatz, this corresponds to the non-stress free reference state and metric introduced in the paper by Efrati *et al.* [144]. It will change conformation, in order to minimise its elastic energy. As a first step, we will study the favoured configuration of the sheet between the flat and left or right-handed states. From the formulation derived by Efrati *et al.*, we calculate the energy of both states, starting with the flat one. The sheet does not bend in the flat state, such that the bending energy is null. The stretching energy density of the flat sheet reads:

$$\omega_s = \frac{Y}{8\left(1-\nu^2\right)}\frac{\left(1-\bar{g}\right)^2}{\bar{g}^2}, \tag{4.17}$$

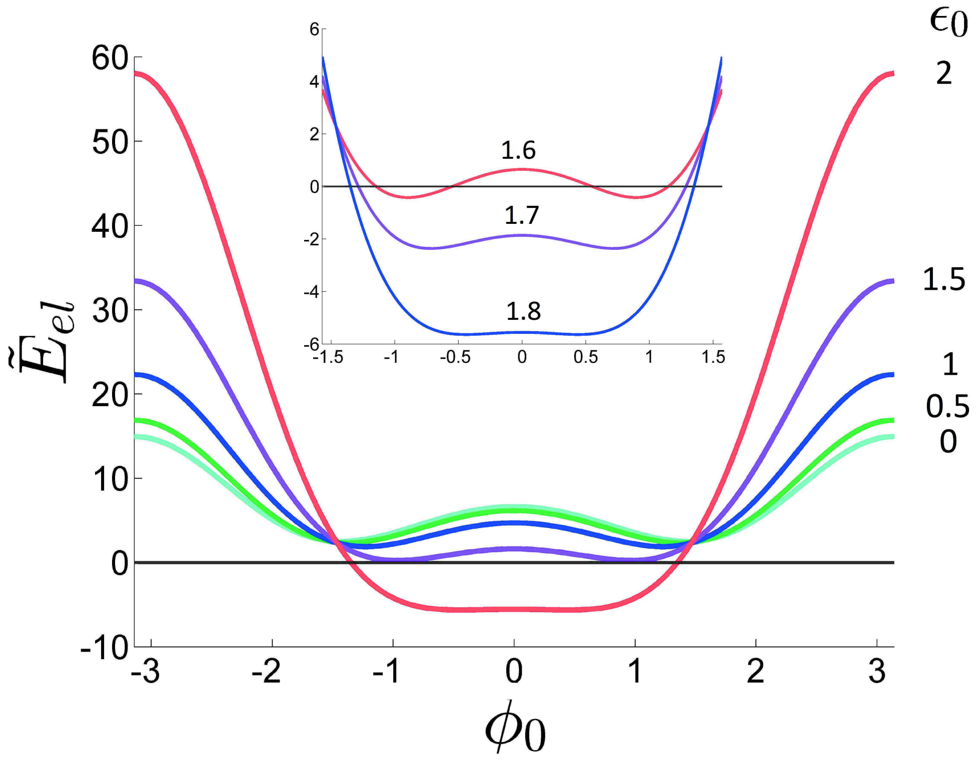

Figure 4.6: Reduced difference of energy between the helical and flat sheet for different amplitudes as a function of the location of the center of the sheet along the y-axis.

and the total elastic energy is $E_{el,1} = Lt \int_{-w}^{w} \sqrt{\bar{g}} \omega_s dy$, where L is the length of the sheet, t its thickness and $2w$ its width. On the other hand, the energy densities of the helical surface read:

$$\omega_s = \frac{Y}{8\left(1-\nu^2\right)} \left(\frac{\left(1 - R\kappa \cos(\phi)\right)^2 + R^2\tau^2}{\bar{g}} - 1 \right)^2 + \frac{Y}{4(1+\nu)} \frac{R^2\tau^2}{\bar{g}}, \tag{4.18}$$

and

$$\begin{aligned} \omega_b = & \frac{Y}{24\left(1-\nu^2\right)} \left(\frac{\kappa \cos(\phi) \left(1 - R\kappa \cos(\phi)\right) - R\tau^2}{\bar{g}} - \frac{1}{R} \right)^2 \\ & + \frac{Y}{12\left(1+\nu\right)} \frac{\kappa \cos(\phi) \left(1 - R\kappa\cos(\phi)\right)}{R\bar{g}}, \end{aligned} \tag{4.19}$$

and the elastic energy of this configuration $E_{el,2}$ can be calculated thanks to the sum of stretching and bending energies given by Eqs. 4.7 and 4.8. To know which of these two states is the energetically favoured one, we study the difference of elastic energies between these two states $E_{el} = E_{el,2} - E_{el,1}$. In Fig. 4.6, the reduced difference of elastic energies $\tilde{E}_{el} = \dfrac{E_{el}\left(1-\nu^2\right)}{YLt}$ is plotted as a function of the position of the center of the sheet on the tubular helix ϕ_0, where $\phi_0 = 0$ when the the center of the sheet follows the shortest helical path [6]. For $\tilde{E}_{el} < 0$, the symmetry is broken and leads to two different states, the left or

---

[6] As mentioned in appendix D.2, $\phi = y/R + \phi_0$.

right-handed helices. It appears from the chosen ansatz that the symmetry breaking occurs for high values of the prestrain only. For $\epsilon_0 \gtrsim 1.5$, which corresponds to a prestrain at both edges of the order of 50%, the sheet adopts the left or right-handed helix. Nonetheless, for such values of the prestrain, we are not any more in the small strain limit. It is interesting to notice that for ϵ values slightly larger than 1.5, the sheet displays four identical states, two for each handedness. Indeed, in Fig.4.6, the energy is minimal for two values of ϕ_0, which leads to a second symmetry breaking with the center of the sheet located closer and closer to the shortest path.

It is important to note that the right or left-handed states might not minimise the elastic of the sheet, and that the latter ansatz might not be the right one to describe the prestrain applied to the cytoskeleton of the Spiroplasma. Indeed, to find the solution minimising the elastic energy, we should solve the equations of the metric of the sheet described in appendix D.1, which might lead to a different state. Moreover, the formulation of the ansatz might also be wrong as we do not clearly understand yet where the prestrain comes from, even if we suppose that it comes from the interaction between the MreB and *fib* fiber sheets. When all these uncertainties will have been fixed, a next step would be to introduce the change of helicity on the shape of the sheet. The method is to solve the boundary value problem defined in appendix D.1. We would have to consider that the sheet is left-handed at one side, and right-handed at the other side. As a first step, to simplify the calculation, we propose the study of the case where the kink is in the middle of the sheet, due to the simplifications implied by the symmetry of the system.

4.5 Conclusion

We have discussed in this chapter the motility of cells, and more particularly the flagella and the helical change of Spiroplasma. We first described the flagella existing in both eukaryotic and prokaryotic cells, which differ in their functioning. More precisely, prokaryotic flagella work on the principle of a rotor and stator, when the eukaryotic flagella induce movements due to the bending of the cytoskeleton. As a second step, we discussed the motion of the helically-shaped Spiroplasma, a bacteria, which displays a bacterial cystoskeleton. Spiroplasma cells are known to move thanks to the contraction and elongation of this cytoskeleton, which induces the propagation of a kink along its body. The kink present in the bacteria is created in order to minimise the energy of the bacteria when it displays both helicity along its body. Its propagation leads to the displacement of the Spiroplasma in the direction opposite to the kink.

We proposed a model to describe the propagation of the kink along the cell. We discussed, as a first step, the change of conformation of the cytoskeleton (which we describe as a thin elastic sheet) from a flat state to a helical shape. The two helical states are not equal as the strains are different. Nonetheless, we want to develop a theory where the left and right-handedness of the cytoskeleton arises thanks to a symmetry breaking. The idea is that the sheet is prestrained, and wants to minimise its energy under such a condition. From the ansatz we formulated, the left and right-handed helices are similar in energy, and do minimise the elastic energy for large prestrains. Moreover, the cytoskeleton follows the shortest helical path, which is for a sheet of negative Gaussian curvature. According to the ansatz discussed above, the sheet can adopt a conformation of negative Gaussian curvature depending on the amplitude of the prestrain, but not in the small strain limit. Moreover, we are not sure for the moment that the form of the prestrain corresponds to the one which constrains the cytoskeleton of the Spiroplasma. A deeper analysis must be done to understand this fascinating motility apparatus.

Chapter 5

Conclusion and perspectives

In this thesis, the elasticity of bio-filaments, such as FtsZ or dynamin, and their interactions with biological membranes has been studied. Traditionally, such bio-filaments are considered as thin elastic rods with a single elastic modulus, the bending stiffness. The Worm-Like Chain model (WLC) is one of the most used model as it successfully describes the dynamics of some bio-filaments, like DNA. Nonetheless, recent experiments showed that a large variety of bio-filaments, such as microtubules, actin filaments, FtsZ rings, dynamin helices among others can not fully be described by this theory. One of the reasons for this incompatibility can come from the polymorphism of the subunit constituents (the proteins) of such filaments. It has been shown, for example, that FtsZ proteins, that are involved in prokaryotic cell division, display two stable states, the straight and the curved state. The FtsZ proteins are in the straight state at rest, and after an activation, thanks to the release of chemical energy, become curved. As the WLC model assumes that the subunit constituents are isotropic, that they can bend in all directions, without any difference, and that they display one rest configuration, this theory does not apply.

Chapter 2 was dedicated to the development of a simplified theoretical model allowing the presence of more than one stable state of the subunit constituents. In addition, these states can have different energies, such that one state is preferentially displayed by the subunits. Inspired by the FtsZ rings and the helical dynamin filaments, which can in a first approximation be treated as a stack of closed rings, we enforced the closure of filaments constituted by such subunits. As a first step, we studied the effects of the change of the mean curvature κ_0 of the filament ring. The degeneracy of the ground state of such filaments coupled to the elastic fluctuations of the subunits leads to a persistence length dependence on the length of the filament, but also on the prestrain applied to the filament to enforce the closure condition. The filament paradoxically softens through prestrain. Finally, we applied this theory to a possible mechanism of tubular membrane breakage. As a result, we found that a high cooperativity between the subunits is necessary to lead to the hemi-fission of the membrane, and tube breakage.

In addition to the polymorphism of proteins, we treated the question of how bio-filaments can apply torques locally to membranes. Indeed, some proteins, like dynamin and FtsZ, are thought not only to constrict the membrane they are linked to (*via* other proteins which are embedded in the membrane), but also to twist it. In this model, the torques are only present for amphiphilic molecules, as it is the mismatch between the intrinsic curvature of the proteins and their anchoring hydrophobic part that leads to the torques. In our work, we assume that the proteins, or assembly of proteins must be prestressed in order to be anchored to the membranes. It appears that when bound to the membrane, the proteins (filaments) will want to release this prestress to minimise their energy. This leads to a competition between the membrane elasticity and the proteins' (filaments') deformations. In the small deformation regime, we studied several geometries of filaments deforming flat or tubular membranes. In a second step, we focused on the membrane mediated-interactions between two filaments, and finally considered a helical distribution of torques around a tubular membrane, assumed to represent the dynamin filaments at the neck of clathrin-coated vesicles. We are aware that being in the linear regime, we can not solve the problem of membrane fission. Nonetheless, numerical simulations could give a better understanding of our model. Moreover, in the future, a deeper study of the interactions of two proteins, that we called *twister* (or similarly *bender*), would also be interesting and give insights on the formation of "twister filaments".

Finally, in the last chapter, we were interested in the motility of prokaryotic and eukaryotic cells. In particular, we briefly discussed the flagella and cilia modes of propulsion. In the rest of the chapter, we introduced the Spiroplasma bacterium, which is a helically-shaped wall-less bacterium, possessing a cytoskeleton. Thanks to a change of conformation of the cytoskeleton, that we see as a thin elastic sheet, the bacterium can change its helicity and propagate a kink along its body, which leads to the motility of the cell. In the overview of our plan for the future, we presented the main ingredients we think are responsible of this kink propagation: symmetry breaking and negative Gaussian curvature. In a first step, we would like to study statically the change of helicity.

Appendix A

A.1 Small Angle X-Ray Scattering (SAXS)

From the scattered intensity (see 1.4 (b) in the main text), one sees Bragg peaks, which are widen due to the effect of thermal fluctuations on the shape of membranes. The scattered intensity graph gives as a result the smectic period $d = \bar{d} + \delta$ of the lamellar phase and the thickness of the water layers $\bar{d}$ and membranes δ. The smectic period of stacks is inversely proportional to the volume fraction of membranes Φ_m. To obtain the bending modulus of the membranes, the profile of the Bragg peaks is analysed through the structure factor of the system. Firstly, the scattered intensity is linked to the density of particles in the system $\rho(\vec{r})$ by:

$$I(\vec{q}) = \left\langle \left| \int_V \rho(\vec{r}) e^{i\vec{q}.\vec{r}} d^3\vec{r} \right|^2 \right\rangle, \tag{A.1}$$

where $\vec{q}$ is the wave vector of the scattered beam and $\langle ... \rangle$ corresponds to a time average. This intensity usually is decomposed in two terms as follows:

$$I(\vec{q}) \propto \frac{P(\vec{q})S(\vec{q})}{q^2}, \tag{A.2}$$

where $P(\vec{q})$ is the form factor which is linked to the structure of the particles and $S(\vec{q})$ is the structure factors which describes the positions of the particles in the sample. Note that in the case of SAXS, the wave vectors being in the range of $1 - 100$ nm, the structure and form factors only give insights on the membranes themselves and not on each particles. For a system of N membranes, the structure factor is defined in the reciprocal space by:

$$S(\vec{q}) = \frac{1}{N} \left\langle \sum_{j,k} e^{-i\vec{q}\left(\vec{R}_j - \vec{R}_k\right)} \right\rangle, \tag{A.3}$$

where $R_{j/k}$ are the positions of the different membranes.

It is then possible to show that in the case of oriented samples, the asymptotic behaviors of the structure factors in the directions perpendicular and parallel to the layer plane are given by power laws [145]:

$$S(0, 0, q_\perp) \propto |q_\perp - q_m|^{\eta_m - 2} \tag{A.4}$$

$$S(q_\parallel, 0, q_m) \propto q_\parallel^{2\eta_m - 4}. \tag{A.5}$$

Note that for non ordered lamellar phases, the asymptotic behavior of the structure factor reads:

$$S(q) \propto |q - q_m|^{1-\eta_m}, \tag{A.6}$$

where $q_m = mq_0 = \frac{2\pi}{d}m$ is the position of the n-th harmonic of the structure factor, and η_m is the Caillé exponent equal to [146]:

$$\eta_m = \frac{k_B T m^2 q_0^2}{8\pi\sqrt{BB_m}}, \tag{A.7}$$

where B_m is the bending stiffness of membranes, B the compression modulus of the stack, k_B is the Boltzmann constant and T the temperature. According to this formula, it is not possible to extract the bending modulus of the membranes. However, a theoretical model developed by Helfrich in Ref. [147], gives a relation between the bending modulus B_m and the strength of the inter-membranes interactions.

The elastic energy of such a system is given by a bending term and a quadratic interaction term between membranes:

$$E_{el} = \frac{B_m}{2}\sum_{n=1}^{N}\int d^2r_\parallel \left(\Delta u_n\right)^2 + \frac{B}{2}\sum_{n=1}^{N}\int d^2r_\parallel \left(u_{n+1}(r_\parallel) - u_n(r_\parallel)\right)^2, \tag{A.8}$$

where Δ corresponds to the in-plane Laplacian and $u_n(\vec{r})$ to the out-of-plane displacement of the n-th membrane. In the continuous limit, the energy can be rewritten, with n the number of layers per unit length, as:

$$E_{el} = \int dz \int d^2\vec{r}_\parallel \left(\frac{nB_m}{2}\left(\Delta u\right)^2 + \frac{B}{2n}\left(\frac{\partial u}{\partial z}\right)^2\right). \tag{A.9}$$

The energy being quadratic, the Fourier modes, defined such that $u(\vec{r}) = \sum_{\vec{q}} u_{\vec{q}} \exp\left(i\vec{q}.\vec{r}\right)$, are decoupled. Thanks to the equipartition theorem, one gets:

$$\left\langle |u_{\vec{q}}|^2 \right\rangle = \frac{k_B T}{V\left((B/n)q_\perp^2 + nB_m q_\parallel^4\right)}, \tag{A.10}$$

where the modes are decomposed into in- $(q_\parallel)$ and out-of-plane (q_z) components, and V is the volume of the sample. Note that for all T, the amplitudes of all the modes can diverge for $\vec{q} \to \vec{0}$, *i.e.*, for large wavelength of deformations.

The next step of this calculation consists of calculating the difference of free energy ΔF between unstacked and stacked states, corresponding respectively to $B = 0$ and $B \neq 0$. The free energy of the system can be decomposed into an internal energy, corresponding to the elastic energy of membranes and an entropy term, such that the difference of free energy ΔF reads:

$$\Delta F = \Delta U - T\Delta S. \tag{A.11}$$

Assuming the distribution of amplitudes to be Gaussian, and neglecting the mode-mode correlations, we can decompose the contributions to the free energy as decoupled, such that:

$\Delta U = \sum_{\vec{q}} \Delta U_{\vec{q}}$ and $\Delta S = \sum_{\vec{q}} \Delta S_{\vec{q}}$. Firstly, from the equipartition theorem (Eq. A.10), one gets the difference of elastic energy per mode:

$$\Delta U_{\vec{q}} = -\frac{k_B T}{2} \frac{(B/n) q_\perp^2}{(B/n) q_\perp^2 + n B_m q_\parallel^4}. \tag{A.12}$$

Secondly, starting from a Gaussian distribution, and counting the possible number of states for different distances between the membranes d, one gets the difference of entropy per mode as:

$$\Delta S_{\vec{q}} = -\frac{k_B}{2} \left(\frac{(B/n) q_\perp^2}{(B/n) q_\perp^2 + n B_m q_\parallel^4} - \ln \left(\frac{n B_m q_\parallel^4}{(B/n) q_\perp^2 + n B_m q_\parallel^4} \right) \right). \tag{A.13}$$

Replacing the sum over the modes by an integral such that $\displaystyle\sum_{\vec{q}} \rightarrow \frac{V}{(2\pi)^3} \int_{-q_{\perp c}}^{q_{\perp c}} \int_0^{q_{\parallel c}} \pi d q_\parallel^2 d q_\perp$, where $q_{\perp c} = \pi/d$ and $q_{\parallel c}$ are cutoff values, and assuming that $\dfrac{n q_{\perp c} \sqrt{B_m}}{q_{\parallel c}^2 \sqrt{B}} \ll 1$, leads at first order to:

$$\Delta F = \frac{3\pi^2 n V (k_B T)^2}{128 B_m d^2}. \tag{A.14}$$

It is possible to determine B from the reduced free energy $\frac{\Delta F}{V}$ thanks to:

$$B = \frac{1}{n} \frac{\partial^2}{\partial d^2} \frac{\Delta F}{V}.$$

Finally, the following result holds:

$$B B_m = \frac{9\pi^2}{64} \frac{(k_B T)^2}{d^4}, \tag{A.15}$$

such that the Caillé coefficients (Eq. A.7) read

$$\eta_m = \frac{4}{3} m^2. \tag{A.16}$$

Note that if the thickness of the membrane δ is taken into account, the Caillé coefficients read :

$$\eta_m = \frac{4}{3} \left(1 - \frac{\delta}{d} \right)^2 m^2. \tag{A.17}$$

This relation still only gives the Caillé coefficients without giving the bending modulus B_m itself. Nonetheless, the Bragg peaks are not symmetrical, and this asymmetry comes from the fluctuations too. For a finite-sized system, the structure factor is then modified, and after averaging on all the orientations of the sample, is given in Ref. [20] by Safinya et al.. It depends on the parameter $\lambda = \sqrt{\dfrac{B_m}{d^2 B}}$ in particular which is linked to the Bragg peaks asymmetry. Knowing λ and the Caillé exponents η_m, one can extract the bending modulus B_m of the lamellar membranes and the inter-membranes interaction strength B. In this paper by Safinya et al. [20], they did a precise study of SAXS on lamellar phases, and got bending modulus of the order of k_BT for a mixture of SDS (Sodium Dodecyl Sulfate), pentanol, water, and dodecane.

An other way to decouple the two variables is to determine the compressibility modulus thanks to the compression of a stack of bilayers *via* a Surface Force Apparatus [30], as mentioned in the main text.

A.2 Micropipette Aspiration

Starting from the Helfrich Hamiltonian given in the main text in Eq. 1.1 and assuming that the membrane does not change its topology (meaning that the Gaussian curvature term can be neglected) and in the small deformation regime, one gets:

$$E_{Hel} = \int \left(\frac{B_m}{2} \left(\frac{\partial^2 u}{\partial x^2} + \frac{\partial^2 u}{\partial y^2} \right)^2 + \frac{\sigma}{2} \left(\left(\frac{\partial u}{\partial x} \right)^2 + \left(\frac{\partial u}{\partial y} \right)^2 \right) \right) dxdy. \tag{A.18}$$

Decomposing the out-of-plane deformation as a Fourier series

$$u(x,y) = \sum_{\vec{q}} u_{\vec{q}} \exp\left(i\vec{q}.\vec{r} \right), \tag{A.19}$$

where $\vec{q} = q_x\vec{i} + q_y\vec{j}$ in Cartesian coordinate, and $q_{x/y} = \frac{2\pi}{L_{x/y}}$, where $L_{x/y}$ are the lengths of the membrane in the x and y-directions. The Helfrich energy after implementing the Fourier series of the out-of-plane deformation in the Hamiltonian, and using the fact that $\iint dx\ dy \exp\left(i \left(\vec{q} - \vec{q'} \right) .\vec{r} \right) = A_0 \delta_{\vec{q},\vec{q'}}$ becomes:

$$E_{Hel} = \frac{A_0}{2} \sum_{\vec{q}} \left(B_m q^4 + \sigma q^2 \right) u_{\vec{q}} u_{-\vec{q}}, \tag{A.20}$$

where A_0 is the projected area, corresponding to $\iint dxdy = L_x L_y$. From the equipartition theorem, one gets that:

$$\langle |u_{\vec{q}}^2| \rangle = \frac{k_B T}{A_0 \left(B_m q^4 + \sigma q^2 \right)}. \tag{A.21}$$

From differential geometry, one gets that the area of the membrane is given by:

$$A = \int dS = \int \sqrt{g} dxdy, \tag{A.22}$$

where $g = det(g_{ij})$, correspond to the determinant of the metric tensor. In the Monge frame, it is given by:

$$\sqrt{g} = \sqrt{1 + \left(\frac{\partial u}{\partial x} \right)^2 + \left(\frac{\partial u}{\partial y} \right)^2} \approx 1 + \frac{1}{2} \left(\left(\frac{\partial u}{\partial x} \right)^2 + \left(\frac{\partial u}{\partial y} \right)^2 \right), \tag{A.23}$$

which gives the following expression:

$$A = A_0 + \frac{1}{2}\sum_{\vec{q}} A_0 q^2 |u_{\vec{q}}|^2. \tag{A.24}$$

Averaging over time the area, and using the expression found thanks to the equipartition theorem (Eq. A.21), one gets the difference between the area of the membrane and the projection of its area ΔA as:

$$\Delta A = \langle A - A_0 \rangle = \frac{1}{2}\sum_{\vec{q}} \frac{k_B T}{B_m q^2 + \sigma}. \tag{A.25}$$

Going to the continuous limit, *i.e.*, $L_{x,y} \to \infty$, one gets:

$$\Delta A = \frac{A_0}{2}\iint \frac{dq_x dq_y}{(2\pi)^2}\frac{k_B T}{B_m q^2 + \sigma} \tag{A.26}$$

$$\Rightarrow \Delta\mu = \frac{\Delta A}{A_0} = \frac{1}{2}\int_{q_{min}}^{q_{max}} \frac{dq}{2\pi}\frac{k_B T}{B_m q^2 + \sigma}, \tag{A.27}$$

where q_{min} and q_{max} correspond to cutoff wave-vectors respectively corresponding to the largest and smallest possible deformations of the membrane. The largest deformation is of the order of the system such that $q_{min}^2 = \frac{(2\pi)^2}{A_0}$, whereas the smallest one is of the order of the thickness t of the membrane, such that $q_{max}^2 = \frac{(2\pi)^2}{t^2}$. The latter integral then gives:

$$\Delta\mu = \frac{k_B T}{8\pi B_m}\ln\left(\frac{B_m q_{max}^2 + \sigma}{B_m q_{min}^2 + \sigma}\right), \tag{A.28}$$

where one usually defines $\sigma_{max} = B_m q_{max}^2$ and $\sigma_{min} = B_m q_{min}^2$. In a micropipette experiment, the following relation typically holds $\sigma_{max} \gg \sigma \gg \sigma_{min}$, such that the relative difference of area $\Delta\mu$ reads:

$$\Delta\mu \approx \frac{k_B T}{8\pi B_m}\ln\left(\frac{\sigma_{max}}{\sigma}\right). \tag{A.29}$$

This calculation has been done for the case of an initially flat membrane fluctuating. In the case of a micropipette experiment, the membrane forms a vesicle, which is approximatively spherical. The same method can be used, the main difference being that the radius of the sphere has to be decomposed in spherical harmonics. However, the relative difference of area is the same for vesicles that do not fluctuate a lot.

To determine the bending modulus of the vesicular membrane, one typically studies the relative difference of area $\Delta\mu$ for several differences of pressure between the pipette and the medium. One quantity of particular interest is the relative apparent surface $\Delta\alpha$ for two differences of pressure ΔP_1 and ΔP_2 with $\Delta P_1 < \Delta P_2$:

$$\Delta\alpha = \frac{A_2^a - A_1^a}{A_1^a}, \tag{A.30}$$

where the exponent a denotes the fact that it is the apparent area of surface and not the real area A. Introducing it in the latter expression, one gets:

$$\Delta\alpha = \frac{\dfrac{A - A_1^a}{A_1^a} - \dfrac{A - A_2^a}{A_2^a}}{1 + \dfrac{A - A_2^a}{A_2^a}} \tag{A.31}$$

$$= \frac{\Delta\mu_1 - \Delta\mu_2}{1 + \Delta\mu_2} \tag{A.32}$$

$$= \frac{\dfrac{k_B T}{8\pi B_m} \ln\left(\dfrac{\sigma_2}{\sigma_1}\right)}{1 + \dfrac{k_B T}{8\pi B_m} \ln\left(\dfrac{\sigma_{max}}{\sigma_2}\right)}. \tag{A.33}$$

For classical experiments, the bending modulus is of the order of tens of $k_B T$, the thickness of the bilayer $t \approx 5$ nm and the surface tension of the order of 10^{-7} to 10^{-5} N.m^{-1}. Thus, the ratio σ_{max}/σ is of the order of 10^5, which allows to approximate the denominator as being close to 1 up to 5% maximum. The measurement of the surface tension itself is not direct, but is done via two Laplace laws applied at the interfaces vesicle-medium and vesicle-micropipette. The pressure inside the vesicle P_{in} is higher than the outer pressures, such that the Laplace laws give:

$$P_{in} - P_{out} = \frac{2\sigma}{R_v} \qquad \text{Interface vesicle-medium,} \tag{A.34}$$

$$P_{in} - P_p = \frac{2\sigma}{R_p} \qquad \text{Interface vesicle-micropipette.} \tag{A.35}$$

Thus, the surface tension can be rewritten as a function of the difference of pressure ΔP between the inside of the micropipette and the medium reads:

$$\sigma = \frac{R_p}{2\left(1 - \dfrac{R_p}{R_v}\right)} \Delta P. \tag{A.36}$$

Finally, the relative apparent surface $\Delta\alpha$ as a function of the measurable quantities reads:

$$\Delta\alpha = \frac{k_B T}{8\pi B_m} \ln\left(\frac{R_{v1}\Delta P_1 \left(R_{v2} - R_p\right)}{R_{v2}\Delta P_2 \left(R_{v1} - R_p\right)}\right). \tag{A.37}$$

An other way to express $\Delta\alpha$ is to determine the apparent areas of the studied system. For instance, for a free spherical vesicle, the apparent area is given by: $A_0^a = 4\pi R_0^{a2}$. However, when the vesicle is sucked in the micropipette, it has a quasi-spherical shape out of the pipette and a cylindrical one inside it, with half a sphere at the end of the tube closing it. The total apparent area is then equal to:

$$A^a = 2\pi R_v^2 \left(1 + \sqrt{1 - \left(\frac{R_p}{R_v}\right)^2}\right) + 2\pi R_p \left(L - R_p\right) + 2\pi R_p^2 \tag{A.38}$$

$$= 2\pi R_v^2 \left(1 + \sqrt{1 - \left(\frac{R_p}{R_v}\right)^2}\right) + 2\pi R_p L, \tag{A.39}$$

where the first and second terms respectively correspond to the area outside and inside the micropipette. In typical experiments, the radius of the micropipette is around one quarter of the radius of the vesicle, such that in a first approximation, the apparent area can be rewritten as:

$$A^a = 4\pi R_v^2 + 2\pi R_p L - \pi R_p^2. \tag{A.40}$$

The volume of the vesicle similarly can be written as:

$$V = \frac{4}{3}\pi R_v^3 + \pi R_p^2 \left(L - R_p\right) + \frac{2}{3}\pi R_p^3. \tag{A.41}$$

Finally, the interesting quantity to determine $\Delta\alpha$ is the difference of apparent area, which is given at first order by:

$$A_2^a - A_1^a = 8\pi R_{v1}\Delta R_v + 2\pi R_p \Delta L, \tag{A.42}$$

where the $\Delta P_2 > \Delta P_1$, such that the vesicle is more aspired in the pipette, meaning that $\Delta L = L_2 - L_1$ is positive and $\Delta R_v = R_{v2} - R_{v1}$ is negative. A last approximation is done on the volume of the vesicle which is assumed to be constant, such that at first order one gets:

$$\Delta R_v = -\frac{R_p^2}{4R_{v1}^2}\Delta L. \tag{A.43}$$

Implementing the latter result in Eq. A.40, and dividing it by A_1^a, one gets $\Delta\alpha$ as a function of the measurable variables:

$$\Delta\alpha = \frac{2R_p \Delta L \left(R_{v1} - R_p\right)}{R_{v1}\left(4R_{v1}^2 + 2R_p L_1 - R_p^2\right)}, \tag{A.44}$$

such that from Eq. A.37, one gets the bending modulus of the vesicular membrane as:

$$B_m = \frac{k_B T}{8\pi}\frac{R_{v1}\left(4R_{v1}^2 + 2R_p L_1 - R_p^2\right)}{2R_p \Delta L \left(R_{v1} - R_p\right)} \ln\left(\frac{R_{v1}\Delta P_1 \left(R_{v2} - R_p\right)}{R_{v2}\Delta P_2 \left(R_{v1} - R_p\right)}\right). \tag{A.45}$$

Note that in principle, the surface tension is given by: $\sigma = \frac{\partial E}{\partial A}$, and in the elastic limit, the difference of surface tension between two states is given by:

$$\Delta\sigma = \sigma_2 - \sigma_1 = K_A \frac{\Delta A}{A_0}, \tag{A.46}$$

where K_A is the membrane compressibility. This corresponds to an elongation of the membrane, which is highly energetic for membranes, and in first approximation can be neglected. However, a more general expression for the relative apparent surface $\Delta\alpha$ (Eq A.33) reads:

$$\Delta\alpha = \frac{k_B T}{8\pi B_m}\ln\left(\frac{\sigma_2}{\sigma_1}\right) + \frac{\sigma_2 - \sigma_1}{K_A}. \tag{A.47}$$

A.3 Details on the Worm-Like Chain model

For simplicity, let us consider an isotropic polymer rod which does not twist and does not preferentially curve. It is described by its following energy:

$$E_{WLC} = \frac{B_f}{2} \int_0^L \kappa(s)^2 ds, \tag{A.48}$$

where B_f is the filament flexural modulus, $L = N\ell$ is the contour length of the filament and N the number of subunits of length ℓ. In this continuous model, the number of subunits is assumed to be large and ℓ going to zero.

Consider firstly that this elastic filament of length s has a constant curvature $\kappa(s) = \kappa = \phi/s$, where ϕ corresponds to the tangent angle to the curve. The elastic energy of this filament then is equal to:

$$E_{WLC} = \frac{B_f}{2}\kappa^2 s = \frac{B_f}{2}\left(\frac{\phi}{s}\right)^2 s. \tag{A.49}$$

Due to the thermal fluctuations and to its rigidity, to filaments will bend differently. A way to get more details on how the filaments will bend is to determine the mean square bending angle by taking a thermal average. In the following, the pre-factor 2 appears as the filaments can bend in two directions independently:

$$\langle \phi^2 \rangle = 2\frac{\displaystyle\int \exp\left(-E_{WLC}/(k_B T)\right)\phi^2 d\phi}{\displaystyle\int \exp\left(-E_{WLC}/(k_B T)\right) d\phi} = 2\frac{k_B T}{B_f} s. \tag{A.50}$$

To describe the filament, one usually defines a frame (called the Frenet frame) linked to the position $\vec{r}$ of the filament in space. The three orthogonal vectors of the Frenet frame are:

- the unit tangent vector $\vec{t} = \frac{d\vec{r}}{ds}$, tangent to the filament
- the normal vector such that: $\frac{d\vec{t}}{ds} = \kappa(s)\vec{n}$
- the bi-normal vector such that: $\vec{b} = \vec{t} \wedge \vec{n}$.

One calculates the correlations between the tangent vectors at two different positions s and s' as follows:

$$\langle \vec{t}(s_1).\vec{t}(s_2) \rangle = \langle \cos(\phi(s)) \rangle = \exp(-|s_1 - s_2|/l_p), \tag{A.51}$$

where $|s_1 - s_2|$ corresponds to the distance between the two points studied along the filament. It is assumed that the correlation is exponentially lost, with characteristic length -called the persistence length- l_p. For small distances $s \ll l_p$, the deviation from the linear rod is small, such that it is possible to expand the cosine as: $\cos(\phi(s)) \approx 1 - \phi^2/2$. At first order, the exponential can also be expanded as: $\exp(-s/l_p) \approx 1 - s/l_p$, where $s = |s_1 - s_2|$.

Finally the correlation between the tangent vectors becomes: $\langle\phi^2(s)\rangle = \frac{2s}{l_p}$.

From Eq. A.50, one gets the persistence length as a function of the bending rigidity of the filament:

$$l_p = \frac{B_f}{k_B T}. \tag{A.52}$$

As mentioned in the main text, different shapes can exist depending on the persistence length of the filament. It can be rod-like, semi-flexible or flexible. In these three conformations, the end-to-end distance $\vec{R} = \int_0^L \vec{t}(s)ds$ differs. The mean square end-to-end distance is obtained from:

$$\langle R^2\rangle = \int_0^L ds \int_0^L ds' \langle\vec{t}(s).\vec{t}(s')\rangle \tag{A.53}$$

$$= \int_0^L ds \int_0^L ds' \exp(-|s-s'|/l_p) \tag{A.54}$$

$$= 2l_p^2 \left(\frac{L}{l_p} - 1 + \exp\left(-\frac{L}{l_p}\right)\right). \tag{A.55}$$

The limiting cases are discussed in the main text. Let us now focus on the so-called gyration radius of the filament. It corresponds to the mean distance between the center of mass and the subunits of the filament and is defined by:

$$\langle R_g^2\rangle = \frac{1}{L^2}\int_0^L ds \int_s^L ds' \langle R^2(s-s')\rangle, \tag{A.56}$$

where the second integral is performed from s to L to avoid double counting. The end-to-end distance is valid for any subsection of the filament, such that by inserting the result from Eq. A.55 in Eq. A.56 and integrating, we get:

$$\langle R_g^2\rangle = \frac{l_p}{3L}\left(L^3 - 3L^2 l_p + 6L l_p - 6l_p^3\left(1 - \exp\left(-\frac{L}{l_p}\right)\right)\right). \tag{A.57}$$

As for the end-to-end distance, two limiting cases are interesting. On the one hand, for $L/l_p \ll 1$, $\langle R_g^2\rangle \approx \frac{1}{12}L^2$. On the other hand, for $L/l_p \gg 1$, $\langle R_g^2\rangle \approx \frac{1}{3}L l_p$. The results are similar to the one obtained for the end-to-end distance, up to numerical pre-factors.

Appendix B

B.1 Free energy of a closed filament

Let us develop the expression of the free energy for a large number N of monomers of size a, such that $L = Na$. The energy, which is in the discrete case:

$$E = 2a\sum_{n=1}^{N/4}\left(-B\kappa_n^2 + C\kappa_n^4\right), \tag{B.1}$$

becomes

$$E = 2aB\sum_{n=1}^{N/4}\left(-\left(\sigma_n\kappa_1+\Delta\kappa\right)^2+\frac{1}{2\kappa_1^2}\left(\sigma_n\kappa_1+\Delta\kappa\right)^4\right), \tag{B.2}$$

which becomes, using the relation given in Eq. 2.14:

$$E = NaB\left(-\frac{\kappa_1^2}{4}+\frac{\Delta_\kappa^2}{\kappa_1^2}\left(\kappa_1^2+\kappa_0\Delta_\kappa-\frac{3}{4}\Delta_\kappa^2\right)\right). \tag{B.3}$$

The entropic term reads:

$$S = k_B\ln W = k_B\ln\frac{N!}{n_+!n_-!}, \tag{B.4}$$

which becomes

$$S = Nk_B\left(\ln 2-\frac{1}{2}\left(1+\frac{\kappa_0-\Delta_\kappa}{\kappa_1}\right)\ln\left(1+\frac{\kappa_0-\Delta_\kappa}{\kappa_1}\right)-\frac{1}{2}\left(1-\frac{\kappa_0-\Delta_\kappa}{\kappa_1}\right)\ln\left(1-\frac{\kappa_0-\Delta_\kappa}{\kappa_1}\right)\right) \tag{B.5}$$

for a large number of monomers N, thanks to the Stirling formula:

$$\ln(n!) \approx n\ln(n) - n. \tag{B.6}$$

The minimization of the free energy F with respect to Δ_κ

$$\frac{dF}{d\Delta_\kappa} = 0, \tag{B.7}$$

leads to the self-consistent equation

$$\Delta_\kappa = \frac{\kappa_0-\kappa_1+(\kappa_0+\kappa_1)\exp\left(-\epsilon\right)}{1+\exp\left(-\epsilon\right)}, \tag{B.8}$$

where

$$\epsilon = \frac{2aB\Delta_\kappa}{k_BT\kappa_1}(2\kappa_1^2+3\kappa_0\Delta_\kappa-3\Delta_\kappa^2). \tag{B.9}$$

B.2 Method of Lagrange multipliers

The energy of the membrane is given as a function of the amplitudes of the modes of the membrane $A_{n,m}$. Nonetheless, we would like to express it as a function of the amplitudes of the modes of the crunching filament. To do so, let us start from the energy of the membrane, which reads:

$$E_{mem} = \frac{\pi B_m L}{R^3} \sum_{|n|\neq 1} \sum_m M_{n,m} |A_{n,m}|^2, \tag{B.10}$$

where $M_{n,m} = (R^2 k_m^2 + n^2 - 1)^2 - 2(n^2 - 1)$. The radial displacement field reads:

$$u(\phi, z) = \sum_{|n|\neq 1} \sum_m A_{n,m} \exp(i(k_m z + n\phi)), \tag{B.11}$$

and in particular, at $z = 0$, where the crunching ring is located:

$$u(\phi, z = 0) = \sum_{|n|\neq 1} a_n \exp(in\phi), \tag{B.12}$$

where $a_n = \sum_m A_{n,m}$ corresponds to the amplitudes of the modes of the filament.

Using the method of Lagrange multipliers, the energy then reads:

$$\begin{aligned} E_{mem} =& \frac{\pi B_m L}{R^3} \sum_{|n|\neq 1} \sum_m M_{n,m} |A_{n,m}|^2 \\ & - \sum_{|n|\neq 1} \lambda_n \left(\sum_m A_{n,m} - a_n \right) - \sum_{|n|\neq 1} \lambda_n^* \left(\sum_m A_{n,m}^* - a_n^* \right), \end{aligned} \tag{B.13}$$

where λ_n and λ_n^* are the Lagrange multipliers associated to the constraint on the amplitudes of modes, and where the exponent * corresponds to the conjugate of the variable. Minimizing the energy of the membrane with respect to the amplitudes of the modes gives the following shape equations:

$$A_{n,m} = \frac{\lambda_n^* R^3}{\pi B_m L M_{n,m}}. \tag{B.14}$$

From the latter expression, we can easily rewrite the amplitudes of the modes of the filament as:

$$a_n = \sum_m A_{n,m} = \frac{\lambda_n^* R^3}{\pi B_m L} \sum_m \frac{1}{M_{n,m}} = \frac{\lambda_n^* R^3}{\pi B_m L} I_n, \tag{B.15}$$

where $I_n = \sum_m \frac{1}{M_{n,m}}$. This permits us to rewrite the Lagrange multipliers and the amplitudes of the modes of the membrane as functions of the amplitudes of the modes of the filament:

$$\lambda_n^* = \frac{\pi B_m L}{R^3} \frac{a_n}{I_n} \tag{B.16}$$

and

$$A_{n,m} = \frac{a_n}{I_n M_{n,m}}. \tag{B.17}$$

Finally, the energy of the membrane and the radial displacement field read:

$$E_{mem} = \frac{\pi B_m L}{R^3} \sum_{|n| \neq 1} \frac{|a_n|^2}{I_n} \tag{B.18}$$

and

$$u(\phi, z) = \sum_{|n| \neq 1} \frac{a_n J_n(z) \cos(n\phi)}{I_n}, \tag{B.19}$$

where $J_n(z) = \sum_m \frac{\exp(ik_m z)}{M_{n,m}} = \sum_m \frac{\cos(k_m z)}{M_{n,m}}$.

B.3 Integrals

In the large L limit, it is possible to rewrite all the summations over the modes in the z-direction.

For $|n| \neq 1$, we pose $a^2 = n^2 - 1$ and

$$\nu = \sqrt{\frac{2a^2 + \gamma - \sqrt{\gamma^2 + 8a^2}}{2}} \quad \text{and} \quad \beta = \sqrt{\frac{2a^2 + \gamma + \sqrt{\gamma^2 + 8a^2}}{2}}.$$

One obtains:

$$I_n = \sum_{m=-\infty}^{\infty} \frac{1}{M_{n,m}} \approx \frac{L/R}{2\sqrt{\gamma^2 + 8a^2}} \left(\frac{1}{\nu} - \frac{1}{\beta} \right). \tag{B.20}$$

$$J_n = \sum_{m=-\infty}^{\infty} \frac{\cos(k_m d)}{M_{n,m}} \approx \frac{L/R}{2\sqrt{\gamma^2 + 8a^2}} \left(\frac{e^{-\nu|d|/R}}{\nu} - \frac{e^{-\beta|d|/R}}{\beta} \right). \tag{B.21}$$

$$K_n = \sum_{m=-\infty}^{\infty} \frac{(k_m R)^2}{M_{n,m}} \approx \frac{L/R}{2\sqrt{\gamma^2 + 8a^2}} \left(\beta - \nu \right). \tag{B.22}$$

$$L_n = -\frac{\partial J_n}{\partial d} R = \sum_{m=-\infty}^{\infty} \frac{(k_m R) \sin(k_m d)}{M_{n,m}} \approx \frac{L/R}{2\sqrt{\gamma^2 + 8a^2}} \left(e^{-\nu|d|/R} - e^{-\beta|d|/R} \right). \tag{B.23}$$

$$N_n = -\frac{\partial^2 J_n}{\partial d^2} R^2 = \sum_{m=-\infty}^{\infty} \frac{(k_m R)^2 \cos(k_m d)}{M_{n,m}} \approx \frac{L/R}{2\sqrt{\gamma^2 + 8a^2}} \left(\beta e^{-\beta|d|/R} - \nu e^{-\nu|d|/R} \right). \tag{B.24}$$

For $|n| = 1$, one has $a^2 = 0$. We pose $k = \frac{2\pi}{L}$ and obtain:

$$I_{|1|} = \sum_{m\neq 0} \frac{1}{M_{|1|,m}} \approx \frac{(L/R)^2}{12\gamma} + \frac{1}{\gamma^2} - \frac{\coth\left(\frac{\sqrt{\gamma}}{kR}(\pi - k|d|)\right)}{2(\gamma)^{3/2}} L/R. \tag{B.25}$$

$$J_{|1|} = \sum_{m\neq 0} \frac{\cos(k_m d)}{M_{|1|,m}} \approx \frac{(L/R)^2}{2\pi^2\gamma}\left(\frac{\pi^2}{6} - \frac{\pi k d}{2} + \frac{k^2 d^2}{4} - \frac{\pi k R}{2\sqrt{\gamma}} \frac{\cosh\left(\frac{\sqrt{\gamma}}{kR}(\pi - kd)\right)}{\sinh\left(\frac{\sqrt{\gamma}}{kR}\pi\right)} + \frac{(kR)^2}{2\gamma}\right). \tag{B.26}$$

$$K_{|1|} = \sum_{m\neq 0} \frac{(k_m R)^2}{M_{|1|,m}} \approx \frac{L/R}{2\sqrt{\gamma}} \coth\left(\frac{\sqrt{\gamma}}{kR}(\pi - k|d|)\right) - \frac{1}{\gamma}. \tag{B.27}$$

$$L_{|1|} = \sum_{m\neq 0} \frac{(k_m R)\sin(k_m d)}{M_{|1|,m}} \approx \frac{L/R}{\pi\gamma}\left(\frac{\pi - kd}{2} - \frac{\pi}{2}\frac{\sinh\left(\frac{\sqrt{\gamma}}{kR}(\pi - kd)\right)}{\sinh\left(\frac{\sqrt{\gamma}}{kR}\pi\right)}\right). \tag{B.28}$$

$$N_{|1|} = \sum_{m\neq 0} \frac{(k_m R)^2\cos(k_m d)}{M_{|1|,m}} \approx \frac{L/R}{2\sqrt{\gamma}} \frac{\cosh\left(\frac{\sqrt{\gamma}}{kR}(\pi - kd)\right)}{\sinh\left(\frac{\sqrt{\gamma}}{kR}\pi\right)} - \frac{1}{\gamma}. \tag{B.29}$$

B.4 Modes expansion

On the one hand, in the internal frame of the filament, the tangent vector can be expressed as a function of the tangent angle θ (see Fig. B.1) in Cartesian coordinates by:

$$\vec{t} = \cos(\theta)\vec{e}_x + \sin(\theta)\vec{e}_y, \tag{B.30}$$

where

$$\theta = \kappa_0 s + \delta\theta(s) = \theta_0 + \sum_{|n|\neq 1}\left(a_n^\theta \cos(n\theta_0) + b_n^\theta \sin(n\theta_0)\right). \tag{B.31}$$

On the other hand, the tangent vector can be expressed in Cartesian coordinates with respect to the azimuthal component ϕ by (see Fig. B.1):

$$\vec{t} = \frac{1}{N}\left(\frac{\partial x}{\partial \phi}\vec{e}_x + \frac{\partial y}{\partial \phi}\vec{e}_y\right), \tag{B.32}$$

where $N = R + u(\phi) = R + \sum_{|n|\neq 1}(a_n \cos(n\phi) + b_n \sin(n\phi))$ corresponds to the normalization of the vector $\vec{t}$.

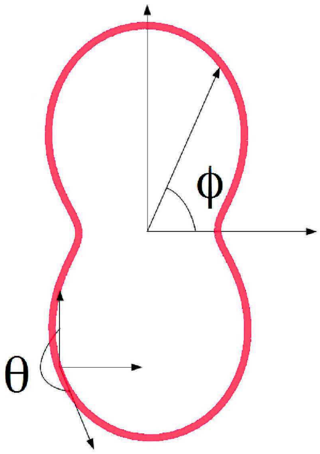

Figure B.1: A crunching polymer ring on a fluid membrane weakly deformed.

Including the components of the position of the filament ($x = (R + u(\phi))\cos(\phi)$ and $y = (R + u(\phi))\sin(\phi)$) in the tangent vector gives to lowest order:

$$\vec{t} = \cos(\phi)\vec{e}_y - \sin(\phi)\vec{e}_x + \frac{1}{R}\frac{\partial u}{\partial \phi}\left(\cos(\phi)\vec{e}_x + \sin(\phi)\vec{e}_y\right). \tag{B.33}$$

Similarly, implementing Eq. B.31 in Eq. B.30 and doing the expansion to lowest order gives:

$$\vec{t} = \cos(\theta_0)\vec{e}_x + \sin(\theta_0)\vec{e}_y + \delta\theta\left(\cos(\theta_0)\vec{e}_y - \sin(\theta_0)\vec{e}_x\right). \tag{B.34}$$

At lowest order, for small deformations of the circular ring, the tangent and azimuthal angles are linked by the following relation: $\theta_0 = \phi - \pi/2$, such that:

$$\begin{aligned}\delta\theta &= \frac{1}{R}\frac{\partial u}{\partial \phi} \\ &= \sum_{|n|\neq 1}\frac{n}{R}\left(a_n^I\cos(n\phi) - a_n^R\sin(n\phi)\right),\end{aligned} \tag{B.35}$$

where $a_n = a_n^R + i a_n^I$.

The free energy of the filament can then be rewritten as follows:

$$\begin{aligned}F_{WLC} &= \frac{l_e k_B T \kappa_0^2}{2R^2}\int_0^L \sum_{n,n'\neq 1} n^2 n'^2\left(a_n^R\cos(n\phi) + a_n^I\sin(n\phi)\right)\left(a_{n'}^R\cos(n'\phi) + a_{n'}^I\sin(n'\phi)\right)ds \\ &= \frac{l_e k_B T \kappa_0^2 L}{4R^2}\sum_n n^4|a_n|^2.\end{aligned} \tag{B.36}$$

B.5 Closed cooperative non-linear chain

Consider the non-linear chain described by the effective energy given by Eq. 2.10:

$$E_{elastic} = \int_0^{l_f}\left(-\frac{B}{2}\theta'^2 + \frac{C}{2}\theta'^4\right)ds, \tag{B.37}$$

where $\kappa = \frac{d\theta}{ds} = \theta'$. If we take into account a coupling between the subunits, and the closure constraint, the total energy of the filament reads:

$$E_{tot} = \int_0^{l_f} \left(-\frac{B}{2}\theta'^2 + \frac{C}{2}\theta'^4 \right) ds + \frac{K}{2} \int_0^{l_f} \theta''^2 ds + \lambda_1 \int_0^{l_f} \cos(\theta) ds + \lambda_2 \int_0^{l_f} \sin(\theta) ds, \quad \text{(B.38)}$$

where λ_1 and λ_2 are Lagrange multipliers. Minimizing the total energy of the filament corresponds to solving the Euler-Lagrange equation:

$$\frac{\partial E_{tot}}{\partial \theta} - \frac{d}{ds}\left(\frac{\partial E_{tot}}{\partial \theta'}\right) + \frac{d^2}{ds^2}\left(\frac{\partial E_{tot}}{\partial \theta''}\right) = 0, \quad \text{(B.39)}$$

which leads to the following differential equation:

$$K\theta'''' + B\theta'' - 2C\left(\theta'^3\right)' + \lambda_2 \cos(\theta) - \lambda_1 \sin(\theta) = 0. \quad \text{(B.40)}$$

To solve this non-linear differential equation, we apply a small perturbation to the circular state and expand the Euler-Lagrange equation. For a circular ring, the polar angle θ is expanded as follows: $\theta = \theta_0 + \delta\theta$, where $\theta_0 = \frac{2\pi}{l_f}s = \kappa_0 s$. Inserting this ansatz in the latter differential equation, and performing a Taylor expansion to first order in $\delta\theta$, we obtain:

$$K\delta\theta'''' + (B - 6C\kappa_0^2)\delta\theta'' - (\lambda_1 \cos(\theta_0) + \lambda_2 \sin(\theta_0))\delta\theta + \lambda_2 \cos(\theta_0) - \lambda_1 \sin(\theta_0) = 0. \quad \text{(B.41)}$$

We immediately see that this expression can be simplified by introducing the tangential projection of the internal ring tension μ, such that:

$$\begin{cases} \lambda_1 = \mu \cos(\theta_0) \\ \lambda_2 = \mu \sin(\theta_0). \end{cases} \quad \text{(B.42)}$$

Inserting these expressions in Eq. B.41, we obtain a further simplification:

$$\delta\theta'''' - \alpha\delta\theta'' - \beta\delta\theta = 0, \quad \text{(B.43)}$$

where

$$\alpha = \frac{6C\kappa_0^2 - B}{K} \text{ and } \beta = \frac{\mu}{K}. \quad \text{(B.44)}$$

The solution of this equation is a sum of four exponential, where two of them have a real exponent and the two others an imaginary exponent. However, the angular ($\theta(l_f) - \theta(0) = 2\pi$) and closure constraints (Eq. 2.8) also need to be expanded to first order and give:

$$\begin{cases} \delta\theta(l_f) - \delta\theta(0) = 0 \\ \int_0^{l_f} \sin(\theta_0)\delta\theta ds = \int_0^{l_f} \cos(\theta_0)\delta\theta ds = 0. \end{cases} \quad \text{(B.45)}$$

To fulfil the first condition on the tangent angle, the two terms with real exponential must vanish, such that the small tangent angle deformation from the circular ring reads:

$$\delta\theta = A\exp(i\gamma s) + B\exp(-i\gamma s), \quad \text{(B.46)}$$

where

$$\gamma = \sqrt{\frac{\sqrt{(6C\kappa_0^2 - B)^2 + 4\mu K} - (6C\kappa_0^2 - B)}{2K}}. \tag{B.47}$$

Furthermore, we obtain a "quantization condition" on γ: $\gamma = \kappa_0 n$, with $n = 1, 2, 3, \ldots$. From the closure constraint, we get that it is impossible to have the mode $n = 1$. Finally, the solution is:

$$\delta\theta = A\exp(in\kappa_0 s) + B\exp(-in\kappa_0 s), \tag{B.48}$$

and

$$n = \sqrt{\frac{\sqrt{(6C\kappa_0^2 - B)^2 + 4\mu K} - (6C\kappa_0^2 - B)}{2K\kappa_0^2}}. \tag{B.49}$$

B.6 Determination of the domains wall characteristics

Consider the non-linear chain described by the effective energy given by Eq. 2.10:

$$E_{elastic} = \int_0^{l_f} \left(-\frac{B}{2}\kappa^2 + \frac{C}{2}\kappa^4\right) ds, \tag{B.50}$$

where $\kappa = \frac{d\theta}{ds} = \theta'$ is the curvature along the curve and l_f the length of the filament. Moreover, let us take into account a coupling between the subunits given by Eq. 2.36:

$$E_{coop} = \frac{K}{2}\int_0^{l_f} \left(\frac{d\kappa}{ds}\right)^2 ds, \tag{B.51}$$

where K is the inter-monomer coupling constant. Assuming that we study a region of length l_s, where $a \ll l_s \ll l_f$ and a is the size of the monomers, one can neglect the closure condition, such that the total energy of this small region of the closed filament reads:

$$E_s = \int_0^{l_s} \left(-\frac{B}{2}\kappa^2 + \frac{C}{2}\kappa^4\right) ds + \frac{K}{2}\int_0^{l_s} \kappa'^2 ds. \tag{B.52}$$

Minimizing the total energy of the filament corresponds to solving the Euler-Lagrange equation:

$$\frac{\partial E_s}{\partial \kappa} - \frac{d}{ds}\left(\frac{\partial E_s}{\partial \kappa'}\right) = 0, \tag{B.53}$$

which leads to the following differential equation:

$$K\kappa'' + B\kappa - 2C\kappa^3 = 0. \tag{B.54}$$

Multiplying this equation by κ' allows us to rewrite the latter equation as follows:

$$K\kappa'^2 - C\kappa^4 + B\kappa^2 = D. \tag{B.55}$$

Using the facts that $\kappa_1 = \sqrt{\frac{B}{2C}}$, and that κ' is equal to zero only in regions where the curvature of the monomers is $\kappa = \pm\kappa_1$, we determined the constant $D = \frac{B\kappa_1^2}{2}$. We rewrite the latter equation as

$$\frac{K}{2}\kappa'^2 = \frac{B\kappa_1^2}{4}\left(1 - \frac{\kappa^2}{\kappa_1^2}\right)^2, \tag{B.56}$$

or

$$ds = \sqrt{\frac{2K}{B}}\frac{d\kappa}{\kappa_1\left(1 - \frac{\kappa^2}{\kappa_1^2}\right)}. \tag{B.57}$$

Inserting these two expressions in the energy, and considering that there is only one wall domain in the region of length l_s, we find that:

$$E_s = \underbrace{\frac{-B\kappa_1^2 l_s}{4}}_{E(\pm\kappa_1)} + \underbrace{\frac{2\sqrt{2}}{3}\sqrt{KB}\kappa_1^2}_{J}, \tag{B.58}$$

where J corresponds to the transition energy penalty. To switch from regions of curvature κ_1 to regions of curvature $-\kappa_1$ is not abrupt. It is done over a certain characteristic length, which is found by integrating Eq. B.57 and reads:

$$s = \underbrace{2\sqrt{\frac{2K}{B}}}_{\lambda}\operatorname{arctanh}\left(\frac{\kappa}{\kappa_1}\right) + E, \tag{B.59}$$

where E is the position along the filament where $\kappa = 0$, and λ is the characteristic length of the filament.

Appendix C

C.1 Definition of the point torque

The expression for the total energy of a torque distribution on the membrane will be derived for a flat membrane in Cartesian coordinates. For the flat membrane in polar cylindrical coordinates and the tubular membrane the expressions are similar and we will only present the final result.

We start with the energy of two opposite forces placed at two neighbouring points, separated by a distance $\Delta x \ll 1$ in the x-direction and $\Delta y \ll 1$ in the y-direction. The total energy reads:

$$\begin{aligned} E_{tot} = E_{mem} - F \int dx \delta(x - x_1) \int dy\, \delta(y - y_1) u(x, y) \\ + F \int dx\, \delta(x - (x_1 + \Delta x)) \int dy\, \delta(y - (y_1 + \Delta y)) u(x, y). \end{aligned} \tag{C.1}$$

The Taylor expansion up to first order of the delta functions gives:

$$\begin{aligned} \delta(x - (x_1 + \Delta x))\, \delta(y - (y_1 + \Delta y)) = &(\delta(x - x_1) - \delta'(x - x_1)\, \Delta x) \\ &\times (\delta(y - y_1) - \delta'(y - y_1)\, \Delta y) \\ = &\delta(x - x_1)\, \delta(y - y_1) - \delta'(x - x_1)\, \delta(y - y_1)\, \Delta x \\ &- \delta(x - x_1)\, \delta'(y - y_1)\, \Delta y. \end{aligned} \tag{C.2}$$

Therefore, the last term in Eq. (C.1) can be rewritten as follows

$$\begin{aligned} &\int dx\, \delta(x - (x_1 + \Delta x)) \int dy\, \delta(y - (y_1 + \Delta y)) u(x, y) \\ = &\int dx\, \delta(x - x_1) \int dy\, \delta(y - y_1) u(x, y) - \Delta x \int dy\, \delta(y - y_1) \int dx\, \delta'(x - x_1) u(x, y) \\ &- \Delta y \int dx\, \delta(x - x_1) \int dy\, \delta'(y - y_1) u(x, y)\ . \end{aligned} \tag{C.3}$$

Integration by parts

$$\begin{aligned} &\int dx\, \delta(x - (x_1 + \Delta x)) \int dy\, \delta(y - (y_1 + \Delta y)) u(x, y) \\ = &\int dx\, \delta(x - x_1) \int dy\, \delta(y - y_1) u(x, y) + \Delta x \int dy\, \delta(y - y_1) \int dx\, \delta(x - x_1) \frac{du(x, y)}{dx} \\ &+ \Delta y \int dx\, \delta(x - x_1) \int dy\, \delta(y - y_1) \frac{du(x, y)}{dy}\ . \end{aligned} \tag{C.4}$$

yields the total energy:

$$\begin{aligned}E_{tot} &= E_{mem} + F\Delta x \int dy\, \delta(y-y_1) \int dx\, \delta(x-x_1) \frac{du(x,y)}{dx} \\ &+ F\Delta y \int dx\, \delta(x-x_1) \int dy\, \delta(y-y_1) \frac{du(x,y)}{dy}. \end{aligned} \tag{C.5}$$

Considering the limit of infinitesimal torque $F\Delta x \to M_y$ and $F\Delta y \to -M_x$, it is possible to finally rewrite the total energy as follows :

$$E_{tot} = E_{mem} - \int dy \int dx \left(M_x(x,y) \frac{du(x,y)}{dy} - M_y(x,y) \frac{du(x,y)}{dx} \right), \tag{C.6}$$

where $M_{x/y}(x,y) = M_{x/y}\delta(x-x_1)\delta(y-y_1)$ are the point torque densities along the x and y-axis, respectively.

For a flat membrane in polar coordinates the total energy reads:

$$E_{tot} = E_{mem} - \int d\phi \int \frac{\rho}{\lambda} d\rho \left(M_\rho(\rho,\phi) \frac{du(\rho,\phi)}{\lambda d\phi} - M_\phi(\rho,\phi) \frac{du(\rho,\phi)}{d\rho} \right), \tag{C.7}$$

where $M_{\rho/\phi}(\rho,\phi) = M_{\rho/\phi}\delta(\rho-\rho_1)\delta(\phi-\phi_1)$ are the point torque densities along the ρ and ϕ-axis, respectively, and $F\Delta\rho \to M_\phi$, $F\lambda\Delta\phi \to -M_\rho$.

And, for a tubular membrane:

$$E_{tot} = E_{mem} - \int dz \int d\phi \left(M_\phi(\phi,z) \frac{du(\phi,z)}{dz} - \frac{M_z(\phi,z)}{R} \frac{du(\phi,z)}{d\phi} \right), \tag{C.8}$$

where $M_{\phi/z}(\phi,z) = M_{\phi,z}\delta(\phi-\phi_1)\delta(z-z_1)$ are the point torque densities along the ϕ and z-axis, respectively, and $F\Delta z \to -M_\phi$ and $FR\Delta\phi \to M_z$.

C.2 Continuous twister

In the text, the twister is defined by two opposite point torques exerted at both ends of the filament. In this Appendix, we propose to study the twister, but defined now as a filament applying a non homogeneous torque. We assume that the torque of the twister is given by:

$$\begin{aligned} M_x(x,y) &= \frac{2M_x x}{d}\delta(y) && \text{for } -d/2 < x < d/2 \\ &= 0 && \text{otherwise,} \end{aligned} \tag{C.9}$$

where d is the size of the filament and M_x is the torque density.

The energy of the twister (Eq. 3.5) reads:

$$\begin{aligned} E_{M_{ext}} &= -\int_{-d/2}^{d/2} dx \int_{-\infty}^{\infty} dy M_(x,y) \frac{du(x,y)}{dy} \\ &= -\frac{2M_x}{d} \sum_{n,m} C_{n,m} k_n \int_{-d/2}^{d/2} dx\ x \exp\left(ik_m x\right). \end{aligned} \tag{C.10}$$

This energy can be rewritten as:

$$E_{M_{ext}} = -\frac{4M_x}{d}\sum_{n,m}\frac{C_{n,m}k_n}{k_m}\left(\frac{d}{2}\cos\left(k_m d/2\right) - \frac{\sin\left(k_m d/2\right)}{k_m}\right). \tag{C.11}$$

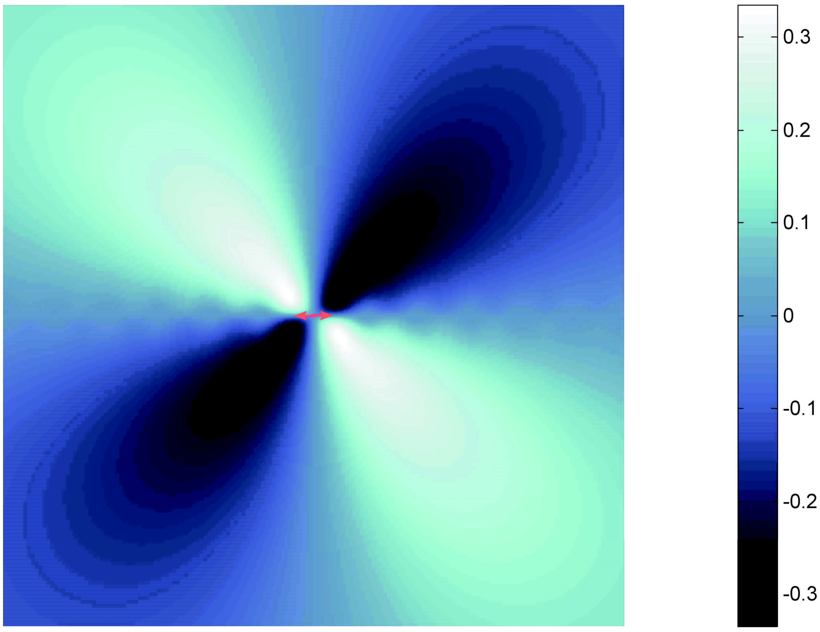

Figure C.1: Representation of the continuous twister and the deformation it induces.

Minimising the total energy of the system, *i.e.*, $E_{tot} = E_{mem} + E_{M_{ext}}$, where E_{mem} is given in the main text by Eq. 3.4 leads to the following shape equations:

$$C_{n,m} = \frac{2M_x}{dB_m}\frac{k_n}{k_m M_{n,m}}\left(\frac{d}{2}\cos\left(k_m d/2\right) - \frac{\sin\left(k_m d/2\right)}{k_m}\right). \tag{C.12}$$

The out-of-plane displacement field and the total energy read:

$$u(x,y) = \sum_{n,m}\frac{2M_x}{dB_m}\frac{k_n}{k_m M_{n,m}}\left(\frac{d}{2}\cos\left(k_m d/2\right) - \frac{\sin\left(k_m d/2\right)}{k_m}\right)\sin\left(k_m x\right)\sin\left(k_n y\right) \tag{C.13}$$

and

$$E_{tot} = -\frac{4M_x^2}{d^2 B_m}\sum_{n,m}\frac{k_n^2}{k_m^2 M_{n,m}}\left(\frac{d}{2}\cos\left(k_m d/2\right) - \frac{\sin\left(k_m d/2\right)}{k_m}\right)^2. \tag{C.14}$$

C.3 Circular ring on a flat membrane

For a flat membrane, the energy is given by Eq 3.2 in the main text:

$$E_{mem} = \frac{B_m}{2}\int\left(\left(\boldsymbol{\nabla}^2 u\right)^2 + \frac{1}{\lambda^2}\left(\boldsymbol{\nabla} u\right)^2\right)dS, \tag{C.15}$$

where $\lambda = \sqrt{\frac{B_m}{\sigma}}$. According to Euler-Lagrange, we get that:

$$\Delta\left(\Delta u - \frac{1}{\lambda^2}u\right) = 0. \tag{C.16}$$

We can rewrite this equation as:

$$\Delta u - \frac{1}{\lambda^2}u = h, \tag{C.17}$$

where h is the harmonic function satisfying $\Delta h = 0$.

As the studied system is a circular ring, we choose cylindrical coordinates to solve the problem. The Laplacian in this framework can be simplified as u and h do not depend on the azimuthal angle ϕ. The Laplacian of h thus becomes:

$$\frac{1}{\rho}\frac{\partial}{\partial\rho}\left(\rho\frac{\partial}{\partial\rho}h\right) = 0. \tag{C.18}$$

Moreover, we decompose the space in two parts. The first one corresponds to the part inside the circular filament (from $\rho = 0$ to $\rho = \rho_0$), while the second one corresponds to the part outside the circular filament (from $\rho = \rho_0$ to $\rho \to \infty$). Solving the latter equation in each region leads to:

$$h = A\ln(\rho/\lambda) - B, \tag{C.19}$$

which is valid for $0 < \rho < \infty$. One can show that the Laplacian is not null on all the space. Indeed, according to Gauss theorem, the integral of the Laplacian of $\ln(\rho)$ on a circle center at the origin is equal to 2π, for all radii. The Laplacian of the logarithm is null everywhere, except at the origin. The function $\ln(\rho)$ thus is not a harmonic function but a Green function up to a prefactor. The logarithm must thus be disregarded on the first region (for $0 \leq \rho \leq \rho_0$). Moreover, in the second region, one can suppress the logarithm by stating that the function u must not diverge. Integrating the function h leads to a divergence at infinity due to the logarithm. This divergence would lead to a divergence of u as well. In order to resolve this problem, the amplitude of the logarithm in the second region also has to be null. The solution thus is:

$$\begin{aligned} h &= -B_1 \quad \text{in region 1} \\ h &= -B_2 \quad \text{in region 2.} \end{aligned} \tag{C.20}$$

Now that we have defined the function h, we can solve the Eq. C.17, which solution is obtained thanks to the method of the constant variation, and is a sum of modified Bessel function of first and second kind:

$$\begin{aligned} u(\rho) &= C_1 + \alpha_1\mathcal{I}_0\left(\frac{\rho}{\lambda}\right) + \beta_1\mathcal{K}_0\left(\frac{\rho}{\lambda}\right) \quad \text{in region 1} \\ u(\rho) &= C_2 + \alpha_2\mathcal{I}_0\left(\frac{\rho}{\lambda}\right) + \beta_2\mathcal{K}_0\left(\frac{\rho}{\lambda}\right) + A_2\ln\left(\frac{\rho}{\lambda}\right) \quad \text{in region 2.} \end{aligned} \tag{C.21}$$

In the first region, the modified Bessel function of second kind $\mathcal{K}_0(\rho/\lambda)$ diverges, such that we take $\beta_1 = 0$. In the second region, the modified Bessel function of first kind $\mathcal{I}_0(\rho/\lambda)$ diverges, similarly to the logarithm. These two terms cannot compensate as the Bessel function diverges as an exponential. We thus have to take $A_2 = \alpha_2 = 0$. The out-of-plane displacement field then reads

$$\begin{aligned} u(\rho) &= C_1 + \alpha_1 \mathcal{I}_0\left(\frac{\rho}{\lambda}\right) \quad \text{in region 1} \\ u(\rho) &= C_2 + \beta_2 \mathcal{K}_0\left(\frac{\rho}{\lambda}\right) \quad \text{in region 2.} \end{aligned} \tag{C.22}$$

The constants are determined thanks to the boundary conditions. Firstly, assuming that at $\rho = \rho_0$, $u = 0$, we can rewrite the two constants C_1 and C_2 as functions of α_1 and β_2. Secondly, thanks to the continuity of the first derivative of u at $\rho = \rho_0$, we can express α_1 as a function of β_2. Finally, the last constant is resolved via the discontinuity of the second derivative of u at $\rho = \rho_0$, which corresponds to the reduced applied torque per unit length, such that:

$$\left.\frac{\partial^2 u}{\partial \rho^2}\right|_{\rho=\rho_{0+}} - \left.\frac{\partial^2 u}{\partial \rho^2}\right|_{\rho=\rho_{0-}} = \frac{(M_\phi \lambda)}{B_m \lambda}. \tag{C.23}$$

The out-of-plane displacement $u(\rho)$ reads after a few lines of calculation:

$$u(\rho,\phi) = \frac{-\rho_0 (M_\phi \lambda) \mathcal{K}_1(\rho_0/\lambda)}{B_m} \left(\mathcal{I}_0\left(\frac{\rho}{\lambda}\right) - \mathcal{I}_0\left(\frac{\rho_0}{\lambda}\right)\right) \quad \text{for} \quad \rho < \rho_0 \tag{C.24}$$

$$u(\rho,\phi) = \frac{\rho_0 (M_\phi \lambda) \mathcal{I}_1(\rho_0/\lambda)}{B_m} \left(\mathcal{K}_0\left(\frac{\rho}{\lambda}\right) - \mathcal{K}_0\left(\frac{\rho_0}{\lambda}\right)\right) \quad \text{for} \quad \rho > \rho_0, \tag{C.25}$$

which corresponds to Eq. 3.17 in the main text.

C.4 General expressions

In this Appendix we derive the general expressions for the cases discussed in Sec. 3.3. In a first step, we consider N point torques on a tubular membrane. Secondly, we will generalize these expressions to N closed torque-applying filaments. Finally, the energy and displacement field will be specialized for two interacting closed rings.

The torques densities of a point torque are given by $M_\phi^{(j)} = \sum_p M_{\phi,p}^{(j)} \delta(z-z_j)\delta(\phi-\phi_j)$ and $M_z^{(j)} = \sum_p M_{z,p}^{(j)} \delta(z-z_j)\delta(\phi-\phi_j)$, respectively. Inserting these expressions in Eq. (C.8) and following the same method as in the main text, one gets the energy and the displacement field:

$$\begin{aligned} E_{tot} = &- \sum_{n,m=-\infty}^{\infty} \sum_{j=1}^{N} \frac{(k_m R M_\phi^{(j)} - n M_z^{(j)})^2}{4\pi B_m M_{n,m} L/R} \\ &- \sum_{n,m=-\infty}^{\infty} \sum_{j<j'} \frac{(k_m R M_\phi^{(j)} - n M_z^{(j)})(k_m R M_\phi^{(j')} - n M_z^{(j')}) \cos(k_m(z_j - z_{j'}) + n(\phi_j - \phi_{j'}))}{2\pi B_m M_{n,m} L/R}. \end{aligned} \tag{C.26}$$

and

$$u(\phi, z) = \sum_{j=1}^{N} \sum_{n,m=-\infty}^{\infty} \frac{\left(k_m R M_{\phi}^{(j)} - n M_z^{(j)}\right) R}{2\pi B_m M_{n,m} L/R} \sin\left(k_m(z-z_j) + n(\phi - \phi_j)\right). \tag{C.27}$$

For closed filaments, the torques densities can be written as $M_{\phi}^{(j)}(\phi, z) = \sum_p M_{\phi,p}^{(j)} \exp(ip\phi)\delta(z-z_j)$ and $M_z^{(j)}(\phi, z) = \sum_p M_{z,p}^{(j)} \exp(ip\phi)\delta(z-z_j)$. Note that $M_{\phi,p}^{(j)}$, and $M_{z,p}^{(j)}$ are complex constants now. The total energy and the displacement field read:

$$E_{tot} = -\pi \sum_{j,j'} \sum_{n,m} \frac{\exp\left(-ik_m(z_j - z_{j'})\right)\left(k_m R M_{\phi,n}^{(j)} - n M_{z,n}^{(j)}\right)\left(k_m R M_{\phi,-n}^{(j')} - n M_{z,-n}^{(j')}\right)}{B_m L/R M_{n,m}} \tag{C.28}$$

and

$$u(\phi, z) = -i \sum_j \sum_{n,m} \frac{\left(k_m R M_{\phi,n}^{(j)} - n M_{z,n}^{(j)}\right) R}{B_m L/R M_{n,m}} \exp\left(i(n\phi + k_m(z - z_j))\right). \tag{C.29}$$

In particular, we decompose $M_{\phi,p}$ and $M_{z,p}$ into their real and imaginary parts in the following: $M_{\phi/z,p}^{(j)} = \frac{1}{2}\left(R_{\phi/z,p}^{(j)} - iT_{\phi/z,p}^{(j)}\right)$.

The energy and the displacement field of two interacting rings are then given by Eqs. (C.28) and (C.29) with $j = 1, 2$:

$$\begin{aligned} E_{tot} = &-\frac{\pi}{4B_m L/R} \sum_{n}^{\infty} \left(\left(R_{\phi,n}^{(1)2} + T_{\phi,n}^{(1)2} + R_{\phi,n}^{(2)2} + T_{\phi,n}^{(2)2}\right) K_n + 2\left(R_{\phi,n}^{(1)} R_{\phi,n}^{(2)} + T_{\phi,n}^{(1)} T_{\phi,n}^{(2)}\right) N_n\right) \\ &-\frac{\pi}{4B_m L/R} \sum_{n}^{\infty} n^2 \left(\left(R_{z,n}^{(1)2} + T_{z,n}^{(1)2} + R_{z,n}^{(2)2} + T_{z,n}^{(2)2}\right) I_n + 2\left(R_{z,n}^{(1)} R_{z,n}^{(2)} + T_{z,n}^{(1)} T_{z,n}^{(2)}\right) J_n\right), \end{aligned} \tag{C.30}$$

and

$$\begin{aligned} u(\phi, z) = &\frac{R}{2B_m L/R} \sum_{j=1}^{2} \sum_{n,m} \left[\frac{k_m R}{M_{n,m}} \left(R_{\phi,n}^{(j)} \cos(n\phi) + T_{\phi,n}^{(j)} \sin(n\phi)\right) \sin\left(k_m(z - z_1)\right)\right. \\ &\left. - \frac{n}{M_{n,m}} \left(R_{z,n}^{(j)} \sin(n\phi) - T_{z,n}^{(j)} \cos(n\phi)\right) \cos(k_m(z - z_1))\right], \end{aligned} \tag{C.31}$$

where $I_n = \sum_m \frac{1}{M_{n,m}}$, $J_n = \sum_m \frac{\cos(k_m d)}{M_{n,m}}$, $K_n = \sum_m \frac{k_m^2 R^2}{M_{n,m}}$ and $N_n = \sum_m \frac{k_m^2 R^2 \cos(k_m d)}{M_{n,m}}$ (see Appendix B.3 for these expressions in the large L limit).

Let us compare the total energies of two superimposed and two infinitely separated rings, when the rings apply the same or opposite torques, *i.e.*, $R_{z/\phi,n}^{(1)} = \pm R_{z/\phi,n}^{(2)} = \pm R_{z/\phi,n}$ and $T_{z/\phi,n}^{(1)} = \pm T_{z/\phi,n}^{(2)} = \pm T_{z/\phi,n}$. For $d = 0$, one sees that $J_n = I_n$ and $K_n = N_n$, such that $E_{tot}^{+}(d/R = 0) = -\frac{\pi}{B_m L/R} \sum_n \left(\left(R_{\phi,n}^2 + T_{\phi,n}^2\right) K_n + n^2 \left(R_{z,n}^2 + T_{z,n}^2\right) I_n\right)$ for torques of same amplitude and $E^-_{tot}(d/R=0)=0$ for opposite amplitudes. In the latter case all torques compensate and the membrane stays cylindrical. This corresponds to the global maximum of the total energy since it is always ≤ 0 in our system (see Sec. 3.2). For $d/R\to\infty$, $J_n=N_n=0$, such that the total energy is equal to $E^+_{tot}(d\to\infty)=E^-_{tot}(d/R\to\infty)= -\frac{\pi}{2B_mL/R}\sum_n\left(\left(R^2_{\phi,n}+T^2_{\phi,n}\right)K_n+n^2\left(R^2_{z,n}+T^2_{z,n}\right)I_n\right)=\frac{1}{2}E^+_{tot}(d/R=0)$. When the two rings are far enough apart, the interaction between them can be neglected. The total energy corresponds to that of two isolated rings and does not depend on the respective orientation of the torques. It is equal to half of the total energy of two superimposed rings applying the same torque due to the proportionality of E_{tot} to the square of the local torque. Furthermore, as the functions J_n and N_n, are oscillatory decaying for increasing d/R, they are maximal when the distance between the two rings is minimal, *i.e.*, when $d/R=0$. This is why the energy is minimal when two filaments superimpose and apply the same torque distribution, no matter the exact form of the torque distribution.

C.5 Ellipsoidal distribution of torques

For an ellipsoidal filament, the so-called “crunching ring” [148], Eqs.C.30 and C.31 can be specialised and read

$$u(\phi,z)=\frac{\pi R}{B_mL/R}\sum\nolimits_m\frac{k_mR}{M_{2,m}}\left(R_{\phi,2}\cos(2\phi)+T_{\phi,2}\sin(2\phi)\right)\sin\left(k_m\left(z-z_1\right)\right) \tag{C.32}$$

$$+\frac{\pi R}{B_mL/R}\sum\nolimits_m\frac{1}{M_{2,m}}\left(R_{z,2}\sin(2\phi)-T_{z,2}\cos(2\phi)\right)\cos(k_m\left(z-z_1\right)), \tag{C.33}$$

and

$$E_{tot}=-\frac{\pi^2}{4B_mL/R}\left(R^2_{\phi,2}+T^2_{\phi,2}\right)K_2-\frac{\pi^2}{B_mL/R}\left(R^2_{z,2}+T^2_{z,2}\right)I_2, \tag{C.34}$$

where $I_2=\sum_m\frac{1}{M_{2,m}}$ and $K_2=\sum_m\frac{k_m^2R^2}{M_{2,m}}$ (see Appendix B.3).

It is important to note that if we impose $M_{z,2}=0$, then the ellipsoidal torque distribution leads to a circular filament. In order to have an ellipsoidal filament, $M_{z,2}$ must be different from zero. Moreover, the torque in the z-direction corresponds to the force imposed by the filament such that for all $n\neq 0$, $R_{z,n}=\frac{n}{2}g_n$ and $T_{z,n}=-\frac{n}{2}f_n$. Moreover, if we set $M_{\phi,n}=0$, we retrieve the energy and the displacement field for n-rings only applying forces on a tubular membrane.

Let us now focus on two ellipsoidal filaments. Firstly, for ellipsoidal filaments only applying torques in the z-direction as shown in Fig. C.2 (c), one sees that for this special distribution of torques, no local extrema is present. Secondly, if the filaments also apply torques in the ϕ-direction, two different profiles of the energy are possible, depending on the following parameter $\alpha=\frac{R^{(1)}_{z,2}R^{(2)}_{z,2}+T^{(1)}_{z,2}T^{(2)}_{z,2}}{R^{(1)}_{\phi,2}R^{(2)}_{\phi,2}+T^{(1)}_{\phi,2}T^{(2)}_{\phi,2}}$. Indeed, for $\alpha<\frac{3-\sqrt{6}}{4}$, the energy profile is given by Fig. C.2(d), while for $\alpha\geq\frac{3-\sqrt{6}}{4}$, the energy profile is given by Fig. C.2(e). The

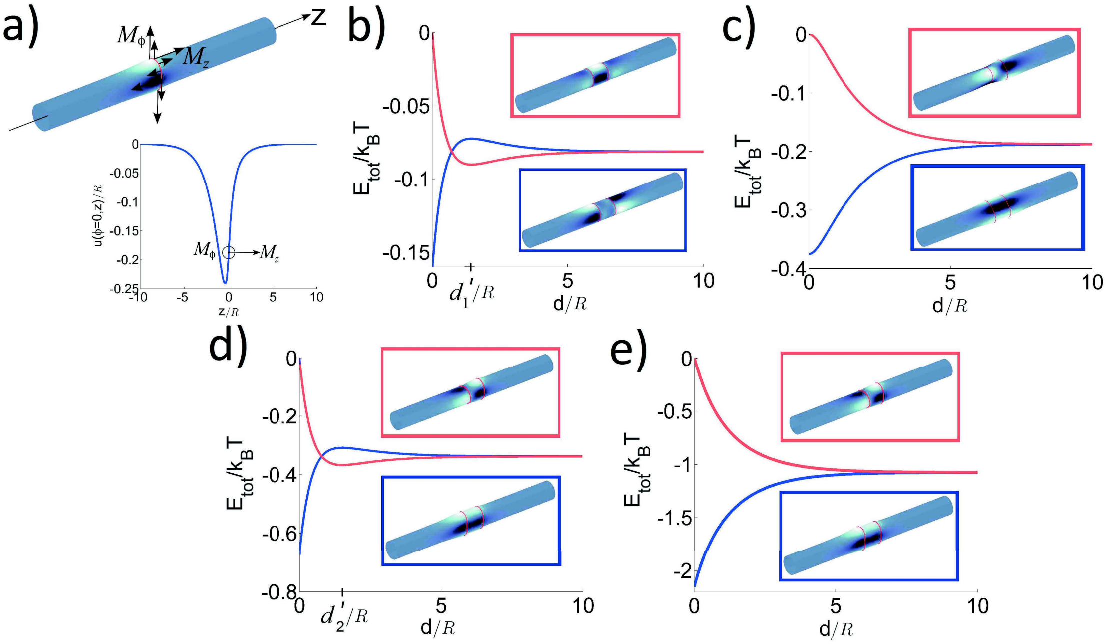

Figure C.2: Closed polymorphic filament(s) applying a uniform torque. (a) Ellipsoidal torque distribution on a tubular membrane.(b)-(e) Two interacting ellipsoidal torque distributions.

value of α depends on the ratio of the torques applied in the z and in the ϕ direction. In order to explain the difference between these two regimes, we will focus on the case of two torques applying the same torques. On the one hand, or filaments only applying torques in the z-direction (Fig. C.2 (c)), the force between the two rings is attractive for distance smaller than d_3 and repulsive for distance larger than d_3. On the other hand, for filaments applying torques in the ϕ-direction (Fig. C.2 (b)), the force between the two rings only is attractive. Finally, if the torques are applied in both directions, the force is equal to the sum of these two forces. If the torques in the z-direction are small compared to the one in the ϕ-direction, the attractive part wins, and the force between the two filaments is only attractive. Whereas for torques in the z-direction larger than the one applied in the ϕ-direction, the repulsive part wins, leading to this bump in the energy profile. Note that the extrema in Fig. C.2 (d) is for a distance $d_4 \approx \frac{ln\left(\frac{4\alpha-3-\sqrt{6}}{4\alpha-3+\sqrt{6}}\right)}{\sqrt{3+\sqrt{6}}-\sqrt{3-\sqrt{6}}}R$.

Appendix D

D.1 Formulation of the boundary value problem

From the expression of the elastic energy $E_{el} = E_b + E_s$, where the energy densities are given in the main text by Eqs. 4.7 and 4.8, one can derive the Euler-Lagrange equilibrium equations. Firstly, one can define the reduced 2D stress and moment tensors by:

$$s^{\alpha\beta} = \frac{\partial \omega_{2D}}{\partial \epsilon^{2D}_{\alpha\beta}} = t A^{\alpha\beta\gamma\delta} \epsilon^{2D}_{\gamma\delta} \tag{D.1}$$

and

$$m^{\alpha\beta} = \frac{\partial \omega_{2D}}{\partial b_{\alpha\beta}} = \frac{t^3}{12} A^{\alpha\beta\gamma\delta} b_{\gamma\delta}, \tag{D.2}$$

where

$$A^{\alpha\beta\gamma\delta} = \frac{Y}{1+\nu} \left(\frac{\nu}{1-\nu} \bar{g}^{\alpha\beta} \bar{g}^{\gamma\delta} + \bar{g}^{\alpha\gamma} \bar{g}^{\beta\delta} \right), \tag{D.3}$$

and $\epsilon^{2D}_{\alpha\beta} = \frac{1}{2}\left(a_{\alpha\beta} - \bar{g}_{\alpha\beta}\right)$ and ω_{2D} are the components of the strain tensor and the out-of-plane displacement field of the mid-surface, respectively.

Minimising the energy leads to the following equations:

$$\begin{aligned}
&\bar{\nabla}_\alpha \left(\bar{\nabla}_\beta m^{\alpha\beta} + \left(\Gamma^\alpha_{\delta\beta} - \bar{\Gamma}^\alpha_{\delta\beta} \right) m^{\delta\beta} \right) - s^{\alpha\beta} b_{\alpha\beta} - m^{\alpha\beta} c_{\alpha\beta} = 0 \\
&\bar{\nabla}_\beta \left(s^{\alpha\beta} + m^{\mu\beta} \left(a^{-1} \right)^{\gamma\alpha} b_{\mu\gamma} \right) + \left(\Gamma^\alpha_{\delta\beta} - \bar{\Gamma}^\alpha_{\delta\beta} \right) \left(s^{\delta\beta} + m^{\mu\beta} \left(a^{-1} \right)^{\gamma\delta} b_{\mu\gamma} \right) \\
&+ \left(\bar{\nabla}_\beta m^{\mu\beta} + \left(\Gamma^\mu_{\delta\beta} - \bar{\Gamma}^\mu_{\delta\beta} \right) m^{\delta\beta} \right) \left(a^{-1} \right)^{\gamma\alpha} b_{\gamma\mu} = 0
\end{aligned} \tag{D.4}$$

and the four following boundary conditions:

$$\begin{aligned}
&n_\alpha n_\beta m^{\alpha\beta} = 0 \\
&n_\beta \left(s^{\alpha\beta} + \left(a^{-1} \right)^{\mu\alpha} b_{\mu\gamma} m^{\gamma\beta} \right) = 0 \\
&n_\beta \left(\bar{\nabla}_\alpha m^{\alpha\beta} + \left(\Gamma^\beta_{\alpha\delta} - \bar{\Gamma}^\beta_{\alpha\delta} \right) m^{\alpha\delta} \right) = 0,
\end{aligned} \tag{D.5}$$

where

$$\begin{aligned}\bar{\nabla}_\beta V^\beta &= \frac{1}{\sqrt{|\bar{g}|}}\partial_\beta\left(\sqrt{|\bar{g}|}V^\beta\right)\\ \bar{\nabla}_\beta M^{\alpha\beta} &= \frac{1}{\sqrt{|\bar{g}|}}\partial_\beta\left(\sqrt{|\bar{g}|}M^{\alpha\beta}\right)+\bar{\Gamma}^\alpha_{\beta\delta}M^{\beta\delta}.\end{aligned} \tag{D.6}$$

Here, the $c_{\alpha\beta}$ form the third fundamental form of the surface, which is directly linked to the first an second fundamental forms by: $c_{\alpha\beta} = 2Hb_{\alpha\beta} - K_G a_{\alpha\beta}$, where H and K_G correspond to the mean and Gaussian curvatures, respectively. Moreover:

$$\bar{\Gamma}^\alpha_{\beta\gamma} = \frac{1}{2}\bar{g}^{\alpha\delta}\left(\partial_\beta\bar{g}_{\gamma\delta}+\partial_\gamma\bar{g}_{\beta\delta}-\partial_\delta\bar{g}_{\beta\gamma}\right) \tag{D.7}$$

are the Christoffel symbols associated with the reference metric, and n_α is the unit normal to the surface.

Finally, in order to satisfy the Gauss-Codazzi equations, which correspond to compatibility equations between the fundamental forms and the mean and Gaussian curvatures, one has to satisfy the following equations:

$$\begin{aligned}&K_G = \frac{1}{2}\left(a^{-1}\right)^{\alpha\beta}\left(\partial_\gamma\Gamma^\gamma_{\alpha\beta}-\partial_\beta\Gamma^\gamma_{\alpha\gamma}+\Gamma^\gamma_{\gamma\delta}\Gamma^\delta_{\alpha\beta}-\Gamma^\gamma_{\beta\delta}\Gamma^\delta_{\alpha\gamma}\right)\\ &\partial_2 b_{\alpha1}+\Gamma^\beta_{\alpha1}b_{\beta2} = \partial_1 b_{\alpha2}+\Gamma^\beta_{\alpha2}b_{\beta1}.\end{aligned} \tag{D.8}$$

Solving the three Eqs. D.4 and the Gauss-Codazzi equations (Eqs. D.8), gives the three components of the first and second fundamentals of the final surface.

D.2 Cytoskeleton under constraints

The cytoskeleton of the Spiroplasma corresponds to a helical sheet. To define the sheet, we first need to introduce the centerline of the helix formed by the cytoskeleton. For a helix, the position of the centerline is given by

$$\vec{r} = \begin{pmatrix} r\cos(t)\\ r\sin(t)\\ ht\end{pmatrix},$$

where r is the radius of the helix and $l = 2\pi h$ is the pitch of the helix.

The unit tangent vector to the curve is given by the derivative of the position vector with respect to the arclength s of the curve. Moreover, the relation between the arclength s and the angular variable t is given by

$$s = \int_0^t \sqrt{\left(\frac{dx}{dt'}\right)^2+\left(\frac{dy}{dt'}\right)^2+\left(\frac{dz}{dt'}\right)^2}dt',$$

leading in our case to : $t=\frac{s}{\sqrt{h^2+r^2}}$, such that finally, the (unit) tangent vector reads

$$\vec{t}=\frac{1}{\sqrt{h^2+r^2}}\begin{pmatrix}-r\sin\left(\frac{s}{\sqrt{h^2+r^2}}\right)\\ r\cos\left(\frac{s}{\sqrt{h^2+r^2}}\right)\\ h\end{pmatrix}.$$

Moreover, according to the Frenet-Serret formulas

$$\begin{aligned}\frac{d\vec{t}}{ds}&=\kappa\vec{n},\\ \frac{d\vec{n}}{ds}&=-\kappa\vec{t}+\tau\vec{b},\\ \frac{d\vec{b}}{ds}&=-\tau\vec{n},\end{aligned}\tag{D.9}$$

where $\kappa=\frac{r}{h^2+r^2}$ and $\tau=\frac{h}{h^2+r^2}$ respectively represent the curvature and the torsion of the curve. For the Spiroplasma, the radius $r\approx 190$ nm, while the pitch $l\approx 900$ nm (giving $h\approx 145$ nm). It follows that the curvature and the torsion approximatively are $\kappa=3.3\times10^{-3}$ nm^{-1} and $\tau=2.5\times10^{-3}$ nm^{-1}.

After a few lines of calculations, the normal vector $\vec{n}$ and the binormal one $\vec{b}$ are given by

$$\vec{n}=-1\begin{pmatrix}\cos\left(\frac{s}{\sqrt{h^2+r^2}}\right)\\ \sin\left(\frac{s}{\sqrt{h^2+r^2}}\right)\\ 0\end{pmatrix}\quad\text{and}\quad\vec{b}=\frac{1}{\sqrt{h^2+r^2}}\begin{pmatrix}h\sin\left(\frac{s}{\sqrt{h^2+r^2}}\right)\\ -h\cos\left(\frac{s}{\sqrt{h^2+r^2}}\right)\\ r\end{pmatrix}.$$

To represent the spiroplasma itself, it is necessary to have the diameter of the Spiroplasma which is approximatively of $d=2R=190$ nm (interestingly it is the same value as the radius of the centerline). The surface is parametrized by the following

$$\vec{X}=\vec{r}+R\left(\cos(\phi)\vec{n}+\sin(\phi)\vec{b}\right),$$

where the angle ϕ is comprised between $\approx-\pi/6$ and $\approx\pi/6$. Moreover, it can be defined differently, in order to be the same variable as the one of the flat sheet as: $\phi=\frac{y}{R}+\frac{\phi_{max}+\phi_{min}}{2}=\frac{y}{R}+\phi_0$, where ϕ_{max} and ϕ_{min} are the maximal and minimal values ϕ can take to define the sheet[1]. Moreover, the width of the sheet is equal to $2w$, such that $R\left(\phi_{max}-\phi_{min}\right)=2w$. Moreover, one can determine the normal vector (which is always a unit vector) to the sheet described by the cytoskeleton as: $\vec{N}=\left(\cos(\phi)\vec{n}+\sin(\phi)\vec{b}\right)$.

From the location of the sheet in space, one can find the first and second fundamental forms of the surface as follows:

$$\begin{aligned}a_{11}&=\left(1-R\kappa\cos\left(\phi\right)\right)^2+R^2\tau^2\\ a_{12}&=R\tau\\ a_{22}&=1\end{aligned}\tag{D.10}$$

---

[1] To make the formulas easier to read, we will only write ϕ instead of $\frac{y}{R}+\frac{\phi_{max}+\phi_{min}}{2}=\frac{y}{R}+\phi_0$ in the equations.

and

$$\begin{aligned} b_{11} &= \kappa\cos(\phi)\left(1 - R\kappa\cos(\phi)\right) - R\tau^2 \\ b_{12} &= -\tau \\ b_{22} &= -\frac{1}{R}. \end{aligned} \tag{D.11}$$

Moreover, the metric determinant and inverse metric of this sheet are equal to:

$$a = a_{11}a_{22} - a_{12}^2 = \left(1 - R\kappa\cos(\phi)\right)^2, \tag{D.12}$$

and

$$\begin{aligned} a^{11} &= \frac{1}{\left(1 - R\kappa\cos(\phi)\right)^2} \\ a^{12} &= \frac{-R\tau}{\left(1 - R\kappa\cos(\phi)\right)^2} \\ a^{22} &= \frac{\left(1 - R\kappa\cos(\phi)\right)^2 + R^2\tau^2}{\left(1 - R\kappa\cos(\phi)\right)^2}. \end{aligned} \tag{D.13}$$

From the metric, we can also determine the mean and Gaussian curvatures of the sheet[2]:

$$H = \frac{-1}{2R} + \frac{\kappa\cos(\phi)}{2\left(1 - R\kappa\cos(\phi)\right)} \tag{D.14}$$

$$K_G = \frac{-\kappa\cos(\phi))}{R\left(1 - R\kappa\cos(\phi)\right)}. \tag{D.15}$$

Finally, the Christoffel symbols read:

$$\begin{aligned} \Gamma^1_{11} &= -\Gamma^2_{12} = \frac{R\tau\kappa\sin(\phi)}{1 - R\kappa\cos(\phi)} \\ \Gamma^2_{11} &= -\frac{\kappa\sin(\phi)\left(\left(1 - R\kappa\cos(\phi)\right)^2 + R^2\tau^2\right)}{1 - R\kappa\cos(\phi)} \\ \Gamma^1_{12} &= \frac{\kappa\sin(\phi)}{1 - R\kappa\cos(\phi)} \\ \Gamma^1_{22} &= \Gamma^2_{22} = 0. \end{aligned} \tag{D.16}$$

Note that the formulas are given for a right-handed helix. To obtain a left-handed helix, one need to replace h by $-h$, such that the torsion τ becomes $-\tau$.

---

[2] The mean and Gaussian curvatures are entirely define by the first and second fundamental forms *via* the following relations: $H = \frac{b_{11}a_{22} - 2b_{12}a_{12} + b_{22}a_{11}}{2a}$ and $K_G = \frac{b_{11}b_{22} - b_{12}^2}{a}$.

Bibliography

[1] D.P. Bartel, and P.J. Unrau, *Trends Cell Biol.* **9**, M9 (1999).

[2] G. Joyce, *Nature* **418**, 214 (2002).

[3] http://niaid.nih.gov/topics/biodefenserelated/biodefense/publicmedia/Pages/image_library.aspx.

[4] http://science.nasa.gov/science-news/science-at-nasa/2004/10sep_radmicrobe/.

[5] http://clinicalcenter.nih.gov/about/news/newsletter/1999/nov99/index.html.

[6] G. B. Bouck, *J. Cell. Biol.* **26**, 523 (1965).

[7] http://rsb.info.nih.gov/ij/images/.

[8] http://micro.magnet.fsu.edu/cells/animalcell.html.

[9] D. S. Goodsell, *Trends Biochem. Sci.* **16**, 203 (1991).

[10] G. Szabo, *Nature* **252**, 47 (1974).

[11] V. Puri et al., *Nature Cell Biol.* **1**, 386 (1999).

[12] M. S.Almén et al., *BMC Biol.* **7**, 50 (2009).

[13] I. Mellman, *Annu. Rev. Cell Dev. Biol.* **12**, 575 (1996).

[14] J. S. Bonifacino, and B. S. Glick, *Cell* **116**, 153 (2004).

[15] P. B. Canham, *J. Theoret. Biol.* **26**, 61 (1970).

[16] W. Helfrich, *Z. Naturforsch.* **28 c**, 693 (1973).

[17] E. A. Evans, *Biophys. J.* **14**, 923 (1974).

[18] *Statistical thermodynamics of surfaces, interfaces, and membranes*, S. A. Safran, (Addison-Wesley, Reading, 1994).

[19] *Differential geometry.*, E. Kreyszig, (Dover, Mineola, NY, 1991).

[20] C. R. Safinya et al., *Phys. Rev. Lett.* **57**, 2718 (1986).

[21] J. F. Nagle, and S. Tristram-Nagle, *BBA Biomem.* **1469**, 159 (2000).

[22] D. Constantin et al., *Eur. Phys. J. E* **12**, 283 (2003).

[23] E. Evans, and W. Rawicz, *Phys. Rev. Lett.* **64**, 2094 (1990).

[24] R. M. Hochmuth, *J. Biomech.* **33**, 15 (2000).

[25] O.-Y. Zhong-can, and W. Helfrich, *Phys. Rev. Lett.* **59**, 2486 (1987).

[26] K. C. Neuman, and A. Nagy, *Nat. Methods* **5**, 491 (2008).

[27] V. Heinrich, and R. Waugh, *Ann. Biomed. Enge* 24, 595 (1996).

[28] S. Svetina et al., *Eur. Biophys. J.* **27**, 197 (1998).

[29] V. G. Meklesh, Master thesis (2014).

[30] D. A. Antelmi, and P. Kekicheff, *J. Phys. Chem. B* **101**, 8169 (1997).

[31] S. J. Marrink et al., *J. Phys. Chem. B* **111**, 7812 (2007).

[32] J. Wolff, C. M. Marques, and F. Thalmann, *Phys. Rev. Lett.* **106**, 128104 (2011).

[33] P. J. Stansfeld, and M. S.P. Sansom, *J. Chem. Theory. Comput.* **7**, 1157 (2011).

[34] J.M. Carlson, and J.P. Sethna, *Phys. Rev. A* **36**, 3359 (1987).

[35] Z. Derzko, and K. Jacobson, *Biochem.* **19**, 6050 (1980).

[36] C. Scomparin et al., *Eur. Phys. J. E* **28**, 211 (2009).

[37] J.T.Woodward, and J.A. Zasadzinski, *Phys. Rev. E* **53**, 3044 (1996).

[38] T. Heimburg, *Biophys. J.* **78**, 1154 (2000).

[39] W.L.C. Vaz, R.M. Clegg, and D. Hallmann, *Biochem.* **24**, 781 (1985).

[40] P.F.F. Almeida, L.C. Vaz, and T.E. Thompson, *Biochem.* **31**, 6739 (1992).

[41] T. Charitat, S. Lecuyer, and G. Fragneto, *Biointerphases* **3**, FB3 (2008).

[42] E. Lindahl, and O. Edholm, *Biophys. J.* **79**, 426 (2000).

[43] J. Liu, and J. C. Conboy, *Biophys. J.* **89**, 2522 (2005).

[44] *Handbook of Biological Physics*, E. Sackmann, (Elsevier Science, New York, 1995).

[45] E. Evans et al., *Biophys. J.* **85**, 2342 (2003).

[46] *Physical Biology of the Cell*, R. Phillips, J. Kondev, and J. Theriot, (Garland Science, New York, 2008).

[47] M. P. Sheetz, *Nat. Rev. Mol. Cell Biol.* **2**, 392 (2001).

[48] J. D. Watson, and F. H. C. Crick, *Nature* **4356**, 737 (1953).

[49] R. K. Montange, and R. T. Batey, *Nature* **441**, 1172 (2006).

[50] http://csls-text3.c.u-tokyo.ac.jp/active/06$_0$5.html.

[51] J.X. Tang et al., *Eur. Biophys. J.* **30**, 477 (2001).

[52] E. H. Egelman, *Nat. Rev. Mol. Cell Biol.* **4**, 621 (2003).

[53] J. Kozuka et al., *Nature Chem. Biol.* **2**, 83 (2006).

[54] T. Sanchez, I. M. Kulić, and Z. Dogic, *Phys. Rev. Lett.* **104**, 098103 (2010).

[55] P. Venier et al., *J. Biol. Chem.* **269**, 13353 (1994).

[56] H. Mohrbach, A. Johner, and I. M. Kulić, *Phys. Rev. Lett.* **105**, 268102 (2010).

[57] H. Mohrbach, A. Johner, and I. M. Kulić, *Eur. Biophys. J.* **41**, 217 (2012).

[58] O. Kahraman et al., *Soft Matter* **10**, 2836 (2014).

[59] L. Chang, and R.D. Goldman, *Nat. Rev., Mol. Cell Biol.* **5**, 601 (2004).

[60] H. Herrmann, et al, *Nature Rev. Mol. Cell Biol.* **8**, 562 (2007).

[61] H. Herrmann et al., *J. Clin. Invest.* **119**, 1772 (2009).

[62] A. Roux et al., *Nature* **441**, 528 (2006).

[63] M. Lenz, J. Prost, and J.-F. Joanny, *Phys. Rev. E* **78**, 011911 (2008).

[64] M. G. J. Ford, S. Jenni, and J. Nunnari, *Nature* **477**, 561 (2011).

[65] S. Morlot, and A. Roux, *Annu. Rev. Biophys.* **42**, 629 (2013).

[66] C. Lu, M. Reedy, and H.P. Erickson, *J. Bacteriol.* **182**, 164 (2000).

[67] M. Osawa, D. E. Anderson, and H. P. Erickson, *Science* **320**, 792 (2008).

[68] R. Shlomovitz and N. S. Gov, *Phys. Biol.* **6**(4), 046017 (2009).

[69] H. P. Erickson, D. E. Anderson, and M. Osawa, *Microbiol. Mol. Biol. Rev.* **74**, 504 (2010).

[70] D. J. Turner et al, *Biophys. J* **102**, 731 (2012).

[71] F. van den Ent, L.A. Amos, and Jan Löwe, *Nature* **413**, 39 (2001).

[72] D. Popp et al, *J. Biol. Chem.* **285**, 15858 (2010).

[73] E. C. Garner et al, *Science* **333**, 222 (2011).

[74] S .M. Ferguson et al, *Science* **316**, 570 (2007).

[75] D. E. Warnock, T. Baba, and S. L. Schmid, *Mol. Biol. Cell.* **8**, 2553 (1997).

[76] A. Raimondi et al, *Neuron.* **70**, 1100 (2011).

[77] T. G. Iversen et al, *Proc. Natl. Acad. Sci. USA* **100**, 5175 (2003).

[78] M.H. Stowell et al., *Nat. Cell Biol.* **1**, 27 (1999).

[79] J. E. Hinshaw, and S. L. Schmid, *Nature* **374**, 190 (1995).

[80] J. F. Carr, and J. E. Hinshaw, *J. Biol. Chem.* **272**, 28030 (1997).

[81] T.Itoh et al, *Dev. Cell.* **9**, 791 (2005).

[82] S. M. Sweitzer, and J.E. Hinshaw, *Cell* **93**, 1021 (1998).

[83] Y. Chen, and H. P. Erickson, *J. Biol. Chem* **280**, 22549 (2005).

[84] S. Pichoff, and J. Lutkenhaus, *EMBO J.* **55**, 1722 (2005).

[85] S. Thanedar, and W. Margolin, *Curr. Biol.* **14**, 1167 (2004).

[86] P. C. Peters et al, *Mol. Microbiol.* **64@**, 487 (2007).

[87] J. Käs et al., *Biophys. J.* **70**, 609 (1996).

[88] F. Gittes et al., *J. Cell Biol.* **120**, 923 (1993).

[89] D. S. Fudge et al., *Biophys. J.* **85**, 2015 (2003).

[90] F. Pampaloni et al., *Proc. Natl. Acad. Sci. USA* **103** 10248 (2006).

[91] C. P. Brangwynne et al., *Biophys. J.* **93**, 346 (2007).

[92] O. Kratky, and G. Porod, *Rec. Trav. Chim.* **68**, 1106 (1949).

[93] *Polymer Physics*, M. Rubinstein, and R. H. Colby, (Oxford University Press, Oxford, 2003).

[94] S. B. Smith, Y. Cui, and C. Bustamante, *Science* **271**, 795 (1994).

[95] F. Ziebert, H. Mohrbach, and I. M. Kulić, *Phys. Rev. Lett.* **114**, 148101, (2015).

[96] R. Kamiya, and S. Asakura, *J. Mol. Biol.* **106**, 167 (1976).

[97] E. Hasegawa, R. Kamiya, and S. Asakura, *J. Mol. Biol.* **160**, 609 (1982).

[98] J. Kürner, A. S. Frangakis, and W. Baumeister, *Science* **307**, 436 (2005).

[99] J. W. Shaevitz, J. Y. Lee, and D. A. Fletcher, *Cell* **122**, 941 (2005).

[100] S. Cohen-Krausz, P. C. Cabahug, and S. Trachtenberg, *J. Mol. Biol.* **410**, 194 (2011).

[101] S. Trachtenberg et al., *PLoS ONE* **9**, 87921 (2014).

[102] J. Hu et al., *Science* **319**, 1247 (2008).

[103] S. Monnier et al., *Phys. Rev. Lett.* **105**, 028102 (2010).

[104] R. Shlomovitz, N. S. Gov, and A. Roux, *New J. Phys.* **13**, 065008 (2011).

[105] S. Asakura, *Adv. Biophys.* **1**, 99 (1970).

[106] C.R. Calladine, *Nature* **255**, 121 (1975).

[107] S. V. Srigiriraju, and T. R. Powers, *Phys. Rev. Lett.* **94**, 248101 (2005).

[108] H. Wada, and R. R. Netz, *EPL* **82**, 28001 (2008).

[109] J. Guven and P. Vàzquez-Montejo, *Phys. Rev. E* **85**, 026603 (2012).

[110] D. A. Quint, A. Gopinathan, and G. M. Grason, *Soft Matter* **8**, 9460 (2012).

[111] J. Guven, D. M. Valencia, and P. Vàzquez-Montejo, *J. Phys. A* **47**, 355201 (2014).

[112] P. Vàzquez-Montejo et al., *Phys. Rev. E* **91**, 063203 (2015).

[113] N. D. Rochman and S. X. Sun, *Soft Matter* **12**, 779 (2016).

[114] T. J. Pucadyil and S. L. Schmid, *Cell* **135**, 1263 (2008).

[115] M. Goulian, R. Bruinsma, and P. Pincus, *Europhys. Lett.* **22**, 145 (1993).

[116] *A Comprehensive introduction to differential geometry*, Vol 3, 3rd ed., ed. by M. Spivak (Publish or Perish, 1999).

[117] A. R. Evans, M. S. Turner, and P. Sens, *PRE* **67**, 041907 (2003).

[118] *Handbook of Mathematical Functions*, 9th ed., ed. by M. Abramowitz and I. A. Stegun (Dover, New York, 1970).

[119] P. G. Dommersnes and J.-B. Fournier, *Eur. Phys. J. B* **12**, 9 (1999).

[120] *Special functions and their applications*, N. N. Lebedev, (Dover, New York, 1972).

[121] G.-M. Nam, N.-K. Lee, H. Mohrbach, A. Johner, and I. M. Kulić, *EPL* **100**, 28001 (2012).

[122] J.-B. Fournier and P. Galatola, *Phys. Rev. Lett.* **98**, 018103 (2007).

[123] M. M. Müller, M. Deserno, and J. Guven, *Europhys. Lett.* **69**, 482 (2005).

[124] 41 M. M. Müller, M. Deserno, and J. Guven, *Phys. Rev. E* **71**, 011921 (2007).

[125] J.-B. Fournier, *Soft Matter* **3**, 883 (2007).

[126] S. M. Ferguson, and P. De Camilli, *Nat. Rev. Mol. Cell Biol.* **13**, 75 (2012).

[127] C. W. Wolgemuth et al., *Phys. Biol.* **2**, 189 (2005).

[128] D. R. Daniels, and M. S. Turner, *PLoS ONE* **8(3)**, e59010 (2013).

[129] H. Aharoni et al., *Phys. Rev. Lett.* **108**, 238106 (2012).

[130] M. J. Pallen, and N. J. Matzke, *Nature Rev. Microbiol.* **4**, 784 (2006).

[131] https://www.studyblue.com/notes/note/n/middy-ii/deck/5472074.

[132] By Flagellum-beating.png: Kohidai, L. derivative work: Urutseg (Flagellum-beating.png) [CC BY 3.0 (http://creativecommons.org/licenses/by/3.0)], via Wikimedia Commons.

[133] F. Ziebert, and I. S. Aranson, *PLoS One* **8**, e64511 (2013).

[134] S. Trachtenberg, and R. Gilad, *Mol. Microbiol.* **41**, 827 (2001).

[135] S. Trachtenberg, *J. Mol. Microbiol. & Biotech.* **11**, 265 (2006).

[136] S. Trachtenberg, *J. Struct. Biol.* **124**, 244 (1998).

[137] J.M. Bové, *Clin. Infect. Dis.* **17**, S10 (1993).

[138] P. Bork et al., *Mol. Microbiol.* **16**, 955 (1995).

[139] J. M. Bové et al., *Annu. Rev. Phytopathol.* **41**, 483 (2003).

[140] M. D. Koch, PhD thesis (2015).

[141] H. Wada, and R. R. Netz, *Phys. Rev. Lett.* **99**, 108102 (2007).

[142] S. Trachtenberg, R. Gilad, and N. Geffen, *Mol. Microbiol.* **47**, 671 (2003).

[143] H. Liang, and L. Mahadevan, *Proc. Natl. Acad. Sci.* **106**, 22049 (2009).

[144] E. Efrati, E. Sharon, and R. Kupferman, *J. Mech. Phys. Solids* **57**9, 762 (2009).

[145] *The Physics of Liquid Crystals*, P. G. De Gennes and J. Prost, (Oxford University Press, Oxford, 1993).

[146] A. Caillé, *Comptes Rendus de l'Académie des Sciences Paris*, 891 (1972).

[147] W. Helfrich, *Z. Naturforsch.* **33**, 305 (1978).

[148] J. Fierling et al., *EPL* **107**, 68002 (2014).

List of Figures

Julien FIERLING

Polymorphic Bio-filaments and their Interaction with Biological Membranes

Résumé

Cette thèse développe, dans le cadre de la biophysique, des modèles théoriques centrés sur les interactions entre les bio-filaments, de longs polymères présents dans les cellules biologiques et les membranes biologiques, qui protègent les cellules de leur environnement. La thèse est divisée en trois parties, traitant différentes systèmes. Dans un premier temps, un modèle admettant plusieurs états de courbure préférée des bio-filaments est développé. Ce type de filaments est forcé à former un anneau et leur interaction avec des membranes tubulaires qu'ils enlacent est discutée. Deuxièmement, les déformations de membranes biologiques modèles sous l'action de filaments appliquant des couples sont calculées, dans le régime linéaire. Finalement, la motilité de la bactérie Spiroplasma est abordée. Les résultats préliminaires d'un modèle élastique sont donnés.

Mots-clés : Membranes biologiques, Bio-filaments, Elasticité, Polymorphisme.

Résumé en anglais

This work focuses on the development of theoretical models in the framework of biophysics. In particular, it deals with the interactions between bio-filaments (long polymer chains found in biological cells) and biological membranes which protect cells from their environment. It is divided in three main parts, where different systems are studied. Firstly, a model going beyond the Worm-Like Chain model is developed to take into account different preferred states of curvature of the constituents of the bio-polymer chains. This kind of filaments are forced to close into a ring and their interactions with tubular membranes they entwine are discussed. Secondly, the deformations induced to biological membranes by torque-applying bio-filaments are discussed in the linear regime. Finally, the motility of the bacteria Spiroplasma. Preliminary results on an elastic model describing the cell motility are given.

Keywords : Biological membranes, Bio-filaments, Elasticity, Polymorphism.